

THE DISSIPATIVE TRAPPED ELECTRON INSTABILITY
IN THE LINEAR MULTI-MIRROR DEVICE

BY

DAVID P. GRUBB

A thesis submitted in partial fulfillment of the
requirements for the degree of

DOCTOR OF PHILOSOPHY
(Nuclear Engineering)

at the

UNIVERSITY OF WISCONSIN - MADISON

1978

ABSTRACT

THE DISSIPATIVE TRAPPED ELECTRON INSTABILITY
IN THE LINEAR MULTI-MIRROR DEVICE

David P. Grubb

Under the supervision of Associate Professor G. A. Emmert

The dissipative trapped electron mode (DTEM) has been predicted to be a major cause of the cross-field transport of particles and heat in tokamaks when they enter the banana regime. The basic physical phenomena necessary for the generation of the DTEM are also present in linear multi-mirror devices.

We have derived a dispersion relation for the DTEM which includes the physics relevant to the description of the plasma in the Linear Multi-Mirror (LMM). This dispersion relation has been found to accurately predict the behavior of the two instabilities which we observe in the collisionality regime $\nu_e/\epsilon \approx \omega_{*e}$, where ν_e/ϵ is the effective electron collision frequency for detrapping out of the magnetic mirrors and ω_{*e} is the electron diamagnetic frequency. The first of these instabilities dominates in the plasma at high magnetic field strength and is localized radially in a region of coinciding density and electron temperature gradients. The second instability dominates in the plasma at low magnetic field strength and is localized radially in a region of relatively weak electron temperature gradient. Based upon the basic drift wave nature of these instabilities, the fact that they increase in amplitude as the mirror ratio is increased, and the agree-

ment which we have obtained between the theoretical predictions derived from the dispersion relation and the experimental measurements, we have identified both of these modes as trapped electron instabilities: the first driven by the electron temperature gradient, the second driven by finite ion Larmor radius effects.

For certain values of the plasma parameters the plasma is unstable to more than one of the trapped electron modes at the same time. When this occurs the plasma has been observed to break into ultra low frequency (ULF) oscillations. These ULF oscillations can be very large ($\delta I_{oi}/I_{oi} \approx 50\%$) and extend radially from the center of the plasma to the walls of the vacuum vessel. They appear to be excited by the non-linear coupling of the trapped electron instabilities. Many of the characteristics of these ULF oscillations are explainable in terms of convective cells, though other explanations may be possible.

G. A. Emmert

ACKNOWLEDGEMENTS

During the course of my graduate study I have recieved a great deal of assistance. Sometimes it was financial; other times it was technical or educational; and often it was in the form of moral support. I would like to be able to acknowledge everyone who has contributed to my work, unfortunately, it would be somewhere between difficult and impossible for me to do so. I hope that all those not directly mentioned here will understand that their contributions did not go unnoticed and were greatly appreciated.

For financial assistance, I gratefully acknowledge the Energy Research and Development Administration, the University of Wisconsin Graduate School, and the National Science Foundation.

For technical assistance, I would like to thank Paul Nonn and, especially Tom Lovell with whom I have had the pleasure of collaborating on the design of many of the alterations and additions to the Linear Multi-Mirror.

For the many varied and indepth discussions of plasma physics (and the problems of the world in general) I would like to thank Roger Richards, Ray Fonck, Charlie Armentrout, and Cliff Strawitch.

I owe my advisor, Dr. G. A. Emmert, a great deal. He has demonstrated to me the enviable ability to guide a student without dominating him. Dr. Emmert has been both my instructor and

my friend, and I have enjoyed working with him and learning from him in all of the phases of research. His analyses of both my successes and my failures have given me a greater insight into plasma physics.

Finally, I owe a very special acknowledgement to my wife, Sue. She has provided half of our income during the course of my graduate study and more than half of the moral support. In addition, she has done a tremendous amount of work in the preparation of the figures for this thesis. I love her dearly and am very proud of her.

TABLE OF CONTENTS

Abstract	ii
Acknowledgements	iv
Table of Contents	vi
Chapter 1. Introduction	1
Chapter 2. Experimental Apparatus	21
Chapter 3. Diagnostics	67
Chapter 4. Equilibrium Plasma	118
Chapter 5. The Dissipative Trapped Electron Instability in the Linear Multi-Mirror Device	135
Chapter 6. Near Zero Frequency Oscillations	207
Chapter 7. Summary	244

CHAPTER 1

INTRODUCTION

Recent advances in the study and understanding of magnetically confined plasmas have led to optimism about our ability to build a fusion reactor. Many of these advances have been made in tokamak research; and it is this device which a majority of researchers believe offers the surest basis for the demonstration of scientific feasibility. The plasma in tokamaks, however, is now entering a regime in which the existence of magnetically trapped particles may play an important role in the stability of the plasma.

Since the magnetic field in present tokamaks is essentially the vacuum magnetic field $\oint \vec{B}_T \cdot d\vec{x}$ is constant, where B_T is the toroidal magnetic field. The field is, therefore, stronger on the inside of the torus than on the outside. In a manner which is analogous to that in mirror machines, a particle may be trapped in the low field region on the outside of the torus. These trapped particles cannot freely circulate around the torus, but are restricted to a bouncing motion in the local magnetic mirrors. The plasma in previous tokamaks was so collisional that the particles executed a random walk motion through the regions of high and low field strength and were essentially unaffected by the presence of the mirrors. In some of the present devices, however, the plasma is less collisional; and the electrons in particular

are sufficiently collisionless that a substantial fraction of the

of the existence of such instabilities. Theoretical predictions and experimental observations serve as the subject of this dissertation.

Review of the Theory*

In their original paper on the DTEM, Kadomtsev and Pogutse¹ per-

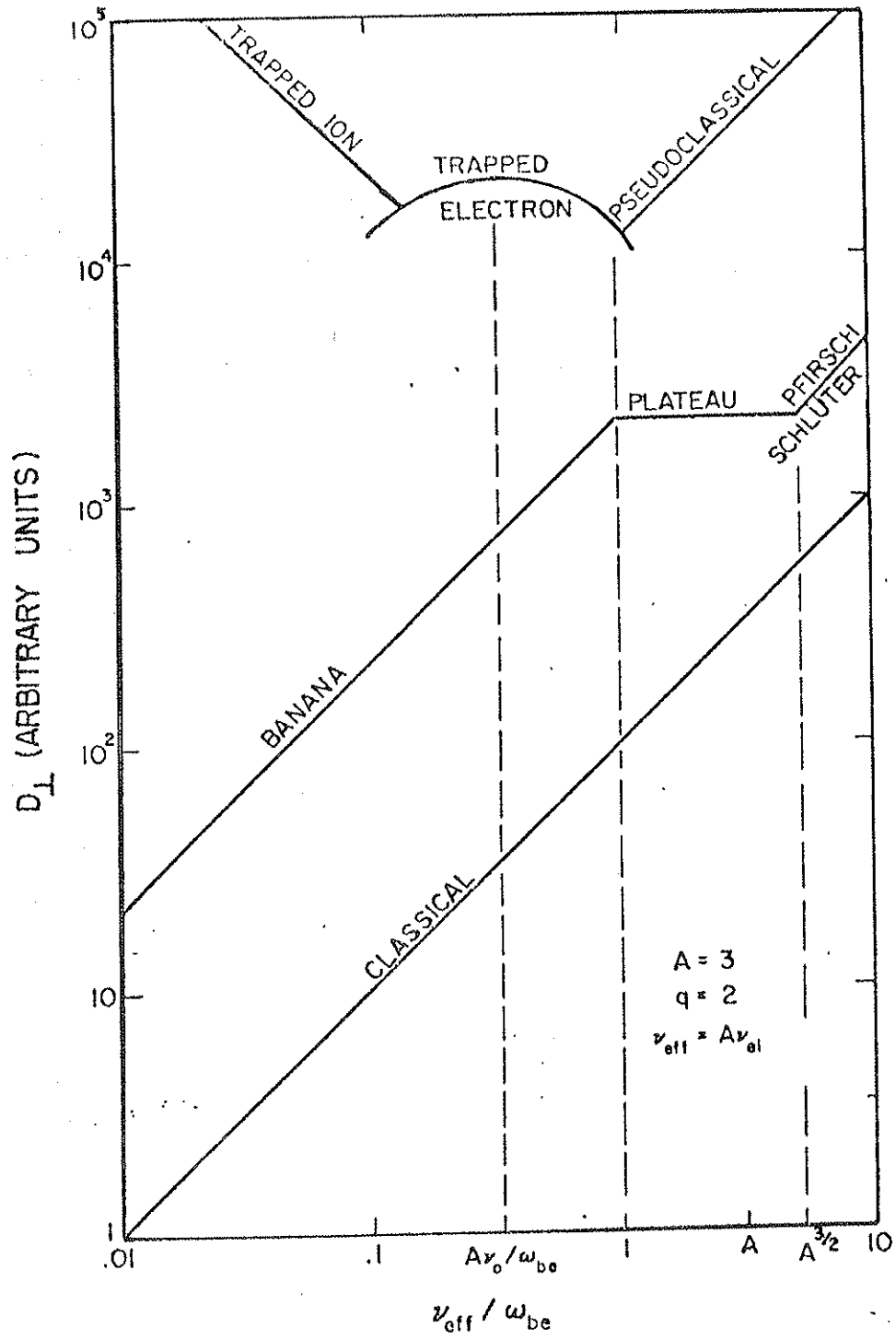
*The theoretical analysis of the dissipative trapped electron instability is generally complicated and often confusing, especially to the reader who has not been introduced to the complexities of toroidal geometries. W. M. Manheimer has written an excellent monograph on this subject entitled "An Introduction to Trapped-Particle Instability in

formed their analysis for a simple cylindrical geometry and retained only the basic physics necessary to generate an instability with a positive growth rate. Their analysis included finite density and electron temperature gradients, a class of trapped and a class of circulating electrons, and an effective collision frequency for the detrapping of the electrons which was a function of the electron's energy. They found that, for effective electron collision frequencies greater than the electron diamagnetic frequency but less than the electron bounce frequency, the DTEM was unstable. This mode has a finite parallel wave number, k_{\parallel} , propagates in the direction of the electron diamagnetic drift at the diamagnetic drift frequency, $\omega = \omega_{*e}$, has a parallel phase velocity greater than the ion thermal velocity and less than the electron thermal velocity, and that the maximum growth rate is of order one tenth of the electron diamagnetic frequency. They also estimated the instability induced cross field transport (Fig. 1-1) due to the DTEM by invoking the strong turbulence relation, $D_{\perp} \sim \gamma/k_{\perp}^2$. The values which they obtained were large enough to predict that diffusion due to the DTEM might be the dominant cause of plasma transport in proposed devices such as TFR and PLT. Before their theory could be directly applied to tokamaks, though, the effects of several important physical phenomena had to be included in the linear theory of the DTEM. These included shear in the magnetic field, ∇B and curvature drifts, Landau

Tokamaks." It is available as TID-27157 from the National Technical Information Service.

Figure 1-1 Theoretically predicted cross-field diffusion coefficient as a function of the electron collisionality in a tokamak. This figure has been copied from H. Houlberg, Ph.D. dissertation, University of Wisconsin, Madison, Wisconsin (1976). It represents a properly normalized version of the figure which appeared in WASH 1295. It does not include the destabilizing effect of the VB resonance which is important at low collisionality.

FIG. 1-1



damping due to circulating electrons, finite ion Larmor radius effects, and finite plasma β .

In 1973 Adam et al.² published a paper dealing with the DTEM in toroidal geometry. They solved the dispersion relation numerically using a Fokker-Planck (FP) collision term instead of the simple Krook model collision operator used by Kadomtsev and Pogutse.¹ They found that the growth rate calculated in Ref. 1 was qualitatively correct. They also found that the DTEM was unstable even if $\eta_e = 0$ ($\eta_e = \frac{d \ln T_e}{d \ln n}$) and with only a slightly lower growth rate. (Their work was subsequently confirmed by Horton et al.³ who compared a Krook type, pitch-angle scattering model collision operator to a FP collision term.) Lastly, Adam found that a Landau type resonance between the wave and the trapped electrons due to the toroidally directed magnetic curvature and gradient drifts of the trapped electrons could cause the DTEM to have a positive growth rate in the low collisionality regime, where it had initially been predicted to be stable. Adam et al.⁴ expounded on this point in a subsequent paper where they showed that the DTEM could dominate plasma transport in small aspect ratio tokamaks even in the collisionality regime where the dissipative trapped ion instability had originally been assumed to be the most damaging plasma instability.⁵ Their work, however, showed that the destabilizing effects of the resonance would not be present if an inverted density profile was created such that $\eta_e < 0$.

Horton⁶ calculated the stability of a tokamak with an inverted

density profile. By taking into account the fact that, for a given electron temperature, some electrons are in each of the three collisionality regimes (collisionless, trapped electron, and collisional), he found that an inverted profile was more stable at low collisionality, but that the plasma was not absolutely stable because $\eta_e < 0$ destabilizes collisionless drift waves.

Finite ion Larmor radius (FLR) effects are also important in the lower collisionality regimes. Liu, Rosenbluth, and Tang⁷ found that it was the FLR effects which caused the DTEM to be unstable at high collisionality ($v_{\text{eff}} > \omega$) even in the absence of an electron temperature gradient. At low collisionality ($v_{\text{eff}} < \omega$), both the FLR effects and the magnetic curvature resonance must be considered since $\eta_e < 0$ is stabilizing with respect to the resonance terms⁴ but destabilizing with respect to the FLR effects⁷.

It may be possible to improve the overall stability at low collisionality by having an inverted density profile with a finite plasma β . Tang et al.⁸ found that β of a few percent was strongly stabilizing to the FLR mode. Finite β , however, was found to have little effect on the DTEM driven by the electron temperature gradient. Landau resonance with the circulating electrons did have a strong stabilizing influence on the ∇T_e modes, but tended to destabilize the FLR modes.

The effects of ion viscosity^{9,10} and the presence of impurities¹¹ in the plasma have also been considered. Ion viscosity exerts an important stabilizing influence only at high collisionality. Impuri-

ties cause an enhanced electron collision frequency with a resulting change in the growth rate as a function of the collision frequency. The presence of impurities can also lead to a new trapped electron instability with a parallel phase velocity greater than the impurity thermal velocity but less than the ion thermal velocity. Neither ion viscosity nor impurities are expected to be important to the stability of the DTEM in tokamak fusion reactors^{10,11}.

The results of a linear stability analysis are the stability criteria and the linear growth rate. If the plasma is stable, then the calculation is complete and other modes of instability can be considered. However, if the plasma is unstable the problem becomes one of determining the dominant non-linear saturation mechanism(s) which causes the instability to saturate at a finite amplitude. In the case of the DTEM, one of the first saturation mechanisms considered was the electrostatic detrapping of the magnetically trapped electrons by the parallel electric field associated with the instability. Kadomstev and Pogutse¹² found that this mechanism caused wave saturation when $e\tilde{\phi}/T_e \approx \epsilon$ where $\tilde{\phi}$ is the wave potential and ϵ is the inverse aspect ratio. However, it was later shown by Ott and Manheimer¹³ that Kadomstev and Pogutse had neglected a term of order 100 so that the wave-induced detrapping would not cause the DTEM to saturate until $e\tilde{\phi}/T_e \approx 100 \epsilon$.

The coupling of unstable waves at low wave numbers to waves with high wave numbers which are strongly damped by shear has been considered as a saturation mechanism.¹⁴ This mode-mode coupling is effective

only when $k_{\perp} \rho_i \ll 1$ (k_{\perp} is the perpendicular wave number and ρ_i is the ion gyro-radius) so that the waves are not dispersive. However, present linear theories predict that modes with $k_{\perp} \rho_i \approx 1$ have the largest growth rates, so this mechanism is probably not important in the saturation of the DTEM in tokamaks. It has recently been proposed that trapped electron induced scattering¹⁵ (analogous to the enhanced collision frequency associated with ion acoustic turbulence) transfers wave energy from the unstable modes at $k_{\perp} \rho_i \approx 1$ to shorter wavelength modes which are damped by ion viscosity.¹⁶ However, there appears to be a limited range of plasma parameters for which trapped electron induced scattering dominates over non-linear ion Landau damping¹⁵ which transfers energy from short wavelengths to long wavelengths where ion viscosity is less effective at damping the wave.

Tsang, Callen, and Vahala¹⁷ have applied Dupree's renormalized quasi-linear (RQL) theory¹⁸ to the problem of the non-linear saturation of the DTEM. They, however, choose to ignore the effects of the turbulent diffusion of the ion orbits and calculate the stabilizing influence of the effective electron collisions caused by wave-induced electrostatic turbulence. Their work is especially interesting because they find that the k_{\perp} in the strong turbulence relation ($D_{\perp} \sim \gamma/k_{\perp}^2$) is k_r for their analysis. This is the first time, to this author's knowledge, that a clear choice between k_{θ} and k_r has been illustrated. Their theory, however, is subject to a number of criticisms¹⁹, not the least of which is the fact that the logical result of the stabilization

of successively more linearly unstable modes by wave-induced turbulence is a state in which only the most unstable mode remains. It is in exactly this state that the assumptions required for RQL theory fail. Until this point and others can be successfully resolved, the validity of RQL theory and its application to the DTEM will remain in doubt.

A final saturation mechanism which has been frequently employed in non-linear calculations is the quasi-linear flattening of the electron temperature and density gradients. Two versions of this theory are used. The first version predicts that the instability saturates when the fluctuating variation in the density gradient is equal to the zero order density gradient, i.e. $\frac{\nabla_r \delta n}{n_0} \approx \frac{1}{L_n}$ where L_n is the unperturbed density scale length. This version of the theory is illogical since it neglects the fact that a local flattening of the density gradient by the wave will be accompanied by a reinforcing of the density gradient at a point where the wave is of the opposite polarity.¹⁹ The second version of this theory predicts mode stabilization when the diffusion caused by the instability reduces the important zero order gradient to the point that the growth rate due to the gradient is exactly balanced by the linear stabilizing mechanism.²⁰ The chief criticism of this theory is an ad hoc argument that the energy input from the neutral beams and the ohmic heating current will maintain the zero order gradients irrespective of plasma instabilities.¹⁷ It is worth noting that the quasi-linear flattening of the electron temperature gradient is the stabilization mechanism observed in computer simulations of plasmas in

linear geometry which are unstable to the DTEM.²¹

Based upon a particular author's preference with respect to a non-linear saturation mechanism, most of the previously referenced papers included some estimate of the cross field transport of particles and heat caused by the DTEM. Since no one theory regarding the saturation of the DTEM has been shown to be clearly superior to the others, it is difficult to place too much faith in the estimates of the diffusion caused by the DTEM which these theories predict. The situation is particularly bad if "typical values" are used in the calculations. Since the values of the plasma parameters vary significantly across the radius of the plasma, it is easy to make large errors in the theoretical evaluation of the instability induced diffusion. This point was clearly illustrated by Chu and Manheimer²² who showed that it is possible to be more than two orders of magnitude off in the determination of the amount of shear required to stabilize the DTEM in a tokamak. This gross error is possible because even a simple stability criteria requires the evaluation of no less than nine variable parameters. Their point is well taken, therefore, when they suggest that the most complete theory possible be used in the stability calculations and that experimentally determined parameters be used in these calculations.

The value of magnetic shear for the stabilization of drift waves in tokamaks, including the DTEM, has been invoked as a part of the linear stability analysis of almost everyone in the previously referenced papers. The validity of the assumption that shear stabilizes

drift waves has recently been called into question.²³ In a simple slab model, the shear in the magnetic field exerts a stabilizing influence on drift waves because it leads to the radiation of energy away from the region of localization of the instability to regions where the energy is absorbed by ion Landau damping. This analysis of the effect of shear relies on two assumptions: (1) the shear is uniform and homogeneous across the radius of the plasma and (2) the instabilities are localized radially. Both of these assumptions are of questionable validity. It has been pointed out by Taylor²³ that the shear in a tokamak is, indeed, not uniform. His analysis shows that a sufficiently large degree of inhomogeneity in the shear will lead to the effective nullification of the stabilizing influence of the shear.

Until recently, the calculations of the mode structure of the DTEM have suppressed either the radial or poloidal variation of the mode structure. This technique made the resulting eigenvalue equation solvable, but led to an artificial localization of the instabilities. Rewoldt et al.^{24,25} have recently performed a fully two-dimensional study of the structure of the DTEM. They found that there was spatial localization of the trapped electron modes and that magnetic shear exerts a stabilizing influence on the modes. However, Ross and Miner²⁶ have also published a fully 2-D modal analysis. Their results, however, indicate that shear does not localize the trapped electron modes. They find global radial structure similar to that found by Taylor²³ for ordinary drift waves. Therefore it would appear at this time that the

role that magnetic shear plays in the stability of the DTEM remains unclear. Until this point is resolved it will be difficult to assess the validity of the stability calculations of the DTEM in tokamaks, much less the estimates of the non-linearly saturated amplitude of the instability or the diffusion that it causes.

Review of Experimental Observations

Stability analysis of the experimentally measured parameters of Ormak, TFR, ST and ATC indicate that the DTEM should be active in all four devices.²² Indeed, measurements of the turbulence spectrum in ATC²⁷ and TFR²⁸ by means of microwave scattering techniques indicate a broadband spectrum of oscillations which have been attributed to drift waves. A more definitive identification of these oscillations as trapped electron modes, however, is nearly impossible due to the turbulent nature of the waves in both devices.

Similar experiments in the FM-1 device using microwave scattering have revealed drift-like waves in this device when it is operated in the trapped electron regime.²⁹ Furthermore, these oscillations appear to be related to the cross field transport of heat.³⁰ The identification of these modes as trapped electron instabilities has been questioned because their response to magnetic shear is not in agreement with theoretical predictions.³¹ In light of the present reevaluation of the role which shear plays in the stabilization of drift-like instabilities, the identity of the instabilities observed in FM-1 remains an open question.

By far the most definitive study of the DTEM in toroidal geometry has been performed by Prater et al.³² in the General Atomic Octopole. Under conditions of very low field strengths ($\bar{B} \sim 100$ Gauss) they observe a large scale ($\delta n/n \lesssim 60\%$), highly coherent oscillation of the plasma. This mode propagates in the direction of the electron diamagnetic drift at a frequency which is approximately the theoretically predicted frequency within the uncertainty associated with the Doppler shift due to a radial electric field. In addition, the wave amplitude as a function of collisionality occurs at values just slightly less than those predicted by linear theory. (The interpretation of this particular data is difficult due to the large error bars associated with the instability amplitude.) Based upon their data they have identified this mode as a DTEM driven by finite ion Larmor radius effects. Perhaps the most interesting aspect of the instability that they observe is that it does not appear to cause significant plasma transport.³³ Experimental confirmation of this observation in another device is desirable to show that it is not a machine-dependent phenomenon.

As shown in the original derivation of the DTEM¹, toroidal effects are not necessary for the generation of this instability. A linear multimirror experiment retains all of the necessary physics for the excitation of the DTEM while avoiding many of the toroidal effects which complicate the study of the trapped electron modes.

In 1973 Deschamps et al.³⁴ reported experimental observation of the DTEM in the ODE device. The ODE experiment is a 5 m long multi-

mirror with a mirror ratio of 1.25. Plasma is created symmetrically at both ends of the device and allowed to flow through cusped fields which isolated the sources from the experimental region. The instability which Deschamps and co-workers observed exhibited many of the predicted characteristics of a DTEM. However, it occurred at collision frequencies which were roughly two orders of magnitude less than the predicted values. Since no theory has been reported which predicts this phenomenon, and since no other experiment has observed the DTEM at such low collision frequencies, their data is certainly open to other interpretations.

Prager et al.³⁵ at Columbia have also reported observation of the DTEM driven by a finite electron temperature gradient. Their experiment is a simple, single cell device. The plasma is created at one end of the experiment outside of the mirror cell. The loss cone portion of the plasma then streams through the mirror cell where a small fraction of the streaming plasma is scattered by collisions into the trapped region of phase space. For mirror ratios greater than approximately 1.4, they observe an instability which propagates in the direction of the electron diamagnetic drift with approximately the diamagnetic frequency. This instability exhibits a broad radial extent with a maximum amplitude in a region where the electron temperature gradient is significantly less than it is nearer the center of the plasma. The data in Ref. 35 appear to be in agreement with their theoretical predictions. However, the fact that their device consists of only a single mirror

cell means that the transit electrons in that device do not repetitively sample the oscillating potential due to the instability, whereas, in a tokamak the circulating electrons continuously sample the wave potential and, thereby, develop a Boltzmann distribution. The extrapolation, therefore, of their observations to a toroidal device is not straightforward.

Using the same device Dixon et al.³⁶ have reported experimental observation of the DTEM driven by finite ion Larmor radius effects. However, their method of measuring the ion temperature by "time of flight" is questionable. The same experiment performed in the DC machine and the Linear Multi-Mirror measures the ion sound speed. Interpretation of this data as a measurement of the ion temperature would indicate ion temperatures which are an order of magnitude higher than those measured spectroscopically.³⁷ Since Dixon's analysis of the importance of the ion gyro-radius effects and the degree of ion Landau damping both hinge critically on the value of the ion temperature, it is difficult to assess the validity of his identification of the instability without a more definitive measurement of the ion temperature.

Dixon and Sen³⁸ have also attempted to use feedback stabilization to determine whether the temperature gradient driven instability reported by Prager³⁵ is dissipative or reactive and to measure its growth rate. It is true that they do not observe the characteristic frequency jump as a function of the phase shift in the feedback circuit that distinguishes a reactive instability.³⁹ However, the maximum reduction in the instability amplitude which they have reported is insufficient to cause a frequency jump even if the mode is reactive.

By the same token, it is difficult to measure the growth rate of an instability which is not completely stabilized. The growth rate can, at best, be only approximated under conditions of incomplete stabilization.⁴⁰

Finally, the work by Primmerman et al.⁴¹ is often referenced with respect to the DTEM but, in fact, is not concerned with this instability. The instability studied by Primmerman is not excited by the collisional detrapping of electrons, but rather, by a resonance between the bounce motion of the trapped electrons and the wave. This bounce resonance mode was theoretically predicted by Coppi.⁴²

Based upon the lack of widely accepted experimental evidence of the DTEM and the obvious need for such evidence to test theoretical predictions, we felt that valuable research in this area could be accomplished in the Linear Multi-Mirror (LMM). At the time that these experiments were proposed (1975), the LMM required several modifications so that the plasma would be unstable to the DTEM. In the following chapters we describe the present configuration of the LMM, our experimental observations, and their correspondence with the theoretical predictions.

References for Chapter 1

1. B. B. Kadomstev and O. P. Pogutse, Soviet Physics-Doklady, 14, 470 (1969)
2. J. C. Adam, G. Laval, and R. Pellat, Nuc. Fusion, 13, 47 (1973)
3. W. Horton, Jr., et al. in Plasma Physics and Controlled Nuclear Fusion Research, Proceedings of the Fifth International Conference, Tokyo (IAEA, Vienna, 1974), p. 541
4. J. C. Adam, W. M. Tang, and P. H. Rutherford, Princeton Plasma Physics Lab Report, Matt 1156 (1975)
5. "Status and Objectives of Tokamak Systems for Fusion Research," AEC, WASH 1295 (1973)
6. W. Horton, Jr., Phys. of Fluids, 19, 711 (1976)
7. C. S. Liu, M. N. Rosenbluth, and W. M. Tang, Phys. of Fluids, 19, 1040 (1976)
8. W. M. Tang, C. S. Liu, M. N. Rosenbluth, P. J. Catto, and J. D. Callen, Nuc. Fusion, 16, 191 (1976)
9. K. R. Chu and W. M. Manheimer, NRL Memorandum Report #3336 (1976)
10. K. T. Tsang, J. D. Callen, and P. J. Catto, ORNL/TM-5236 (1977)
11. K. T. Tsang, ORNL/TM-5287 (1976)
12. B. B. Kadomstev and O. P. Pogutse, Soviet Physics-Doklady, 14, 881 (1970)
13. E. Ott and W. M. Manheimer, Phys. of Fluids, 19, 1035 (1976)
14. W. M. Manheimer, E. Ott, K. R. Chu, J. P. Boris, and J. D. Callen, Nuc. Fusion, 16, 203 (1976)
15. R. Z. Sagdeev and A. A. Galeev, Nonlinear Plasma Theory, Benjamin, New York (1969)
16. Liu Chen, R. L. Berger, J. G. Lominadze, M. N. Rosenbluth, and P. H. Rutherford, Phys. Rev. Lett., 39, 754 (1977)
17. K. T. Tsang, J. D. Callen, and G. Vahala, ORNL/TM-5942 (1977)

18. T. H. Dupree, Phys. of Fluids, 11, 2680 (1968)
19. W. M. Manheimer, NRL Memorandum Report #3369 (1976)
20. W. M. Manheimer, K. R. Chu, E. Ott, and J. P. Boris, NRL Memorandum Report #3248 (1976)
21. Y. Matsuda and H. Okuda, Phys. Rev. Lett., 36, 474 (1976)
22. K. R. Chu and W. M. Manheimer, NRL Memorandum Report #3336 (1976)
23. J. B. Taylor in Plasma Physics and Controlled Nuclear Fusion Research 1976, Proceedings of the Sixth International Conference, Berchtesgaden (IAEA, Vienna, 1977) Vol. II, p. 323
24. G. Rewoldt, W. M. Tang, and E. A. Frieman, Phys. of Fluids, 20, 402 (1977)
25. G. Rewoldt, W. M. Tang, and E. A. Frieman, Princeton Plasma Physics Lab Report PPPL-1387 (1977)
26. D. W. Ross and W. M. Miner, Phys. of Fluids, 20, 1957 (1977)
27. E. Mazzucato, Phys. Rev. Lett., 36, 792 (1976)
28. TFR Group, Plasma Physics and Controlled Nuclear Fusion Research 1976, (IAEA, Vienna) Vol. I, p. 35 (1977)
29. M. Okabayashi and V. Arunasalam, Nuc. Fusion, 17, 497 (1977)
30. S. Ejima and M. Okabayashi, Phys. of Fluids, 18, 904 (1975)
31. N. R. Sautoff, M. Okabayashi, and J. A. Schmidt, Bull. Am. Phys. Soc., 20, 1289 (1975)
32. R. Prater, S. Ejima, T. Ohkawa, and S. K. Wong, GA-A 14220 (1977)
33. R. Prater, S. Ejima, C. Moeller, and T. Ohkawa, Bull. Am. Phys. Soc., 20, 1287 (1975)
34. P. Deschamps, R. Gravier, C. Renaud, and A. Samain, Phys. Rev. Lett., 31, 1457 (1973)
35. S. C. Prager, T. C. Marshall, and A. K. Sen, Plasma Physics, 17, 785 (1975)
36. D. P. Dixon, T. C. Marshall, and A. K. Sen, Bull. Am. Phys. Soc., 22, 1167 (1977)

37. W. C. Guss and R. J. Fonck, Wisconsin Plasma Physics Report PLP 584 (1974)
38. D. Dixon, T. C. Marshall, and A. K. Sen, Bull. Am. Phys. Soc., 20, 1289 (1975)
39. For an analysis of the effect of feedback stabilization on a reactive instability see R. K. Richards, G. A. Emmert, and D. P. Grubb, Plasma Physics, 17, 271 (1975)
40. G. A. Emmert, R. K. Richards, and D. P. Grubb, Wisconsin Plasma Physics Report PLP 618 (1975)
41. C. A. Primmerman, L. M. Lidsky, and P. A. Politzer, Phys. Rev. Lett., 33, 957 (1974)
42. B. Coppi, Phys. Rev. Lett., 16, 1076 (1972)

CHAPTER 2

EXPERIMENTAL APPARATUS

The Linear Multi-Mirror (LMM) was built by Ray Fonck¹ and began operation in 1972 (Fig. 2-1). As originally constructed the device consisted of eleven short mirror cells in a 4.2 m length. A plasma of density 10^{10} cm^{-3} with $kT_e \sim 5 \text{ eV}$ was continuously created by an interdigital Lisitano coil at one end of the device. The plasma then diffused down the length of the experiment until it terminated on a metal endplate. This plate was moveable and was used to determine the length of the plasma column. The plasma was monitored by Langmuir probes at two fixed axial locations and by probes mounted on a moveable cart system.¹ The investigations of the interchange instability and the dissipative drift wave^{2,3} were performed using the LMM in this configuration.

In order to operate the LMM in the parameter regime where the plasma would be unstable to the dissipative trapped electron mode (DTEM)⁴ a differential pumping column and magnets to contain the plasma in the column were added in November of 1975 (Fig. 2-2). The transfer function analyses⁵ were also performed while the machine was in this configuration.

Finally, in November of 1976 the machine was shortened from eleven mirror cells to seven and an aluminum diagnostic port assembly was added to the experiment. As shown in Fig. 2-3 the device has been used for the continuing studies of the temperature gradient driven

Figure 2-1 The Linear Multi-Mirror experiment as constructed
by R. Fonck.

FIG. 2-1

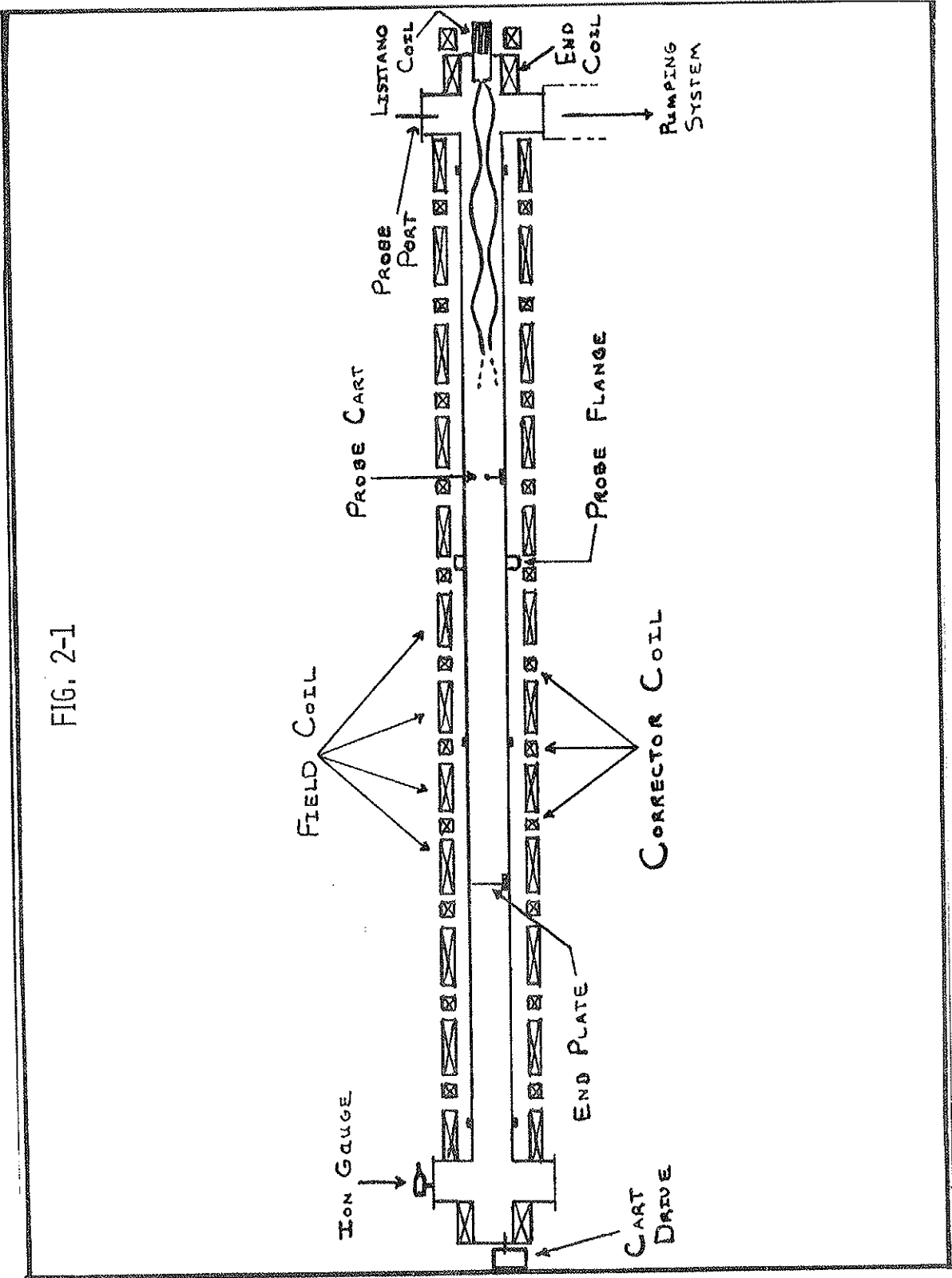


Figure2-2 The Linear Multi-Mirror experiment after the addition of a differential pumping system and the conical helix plasma source.

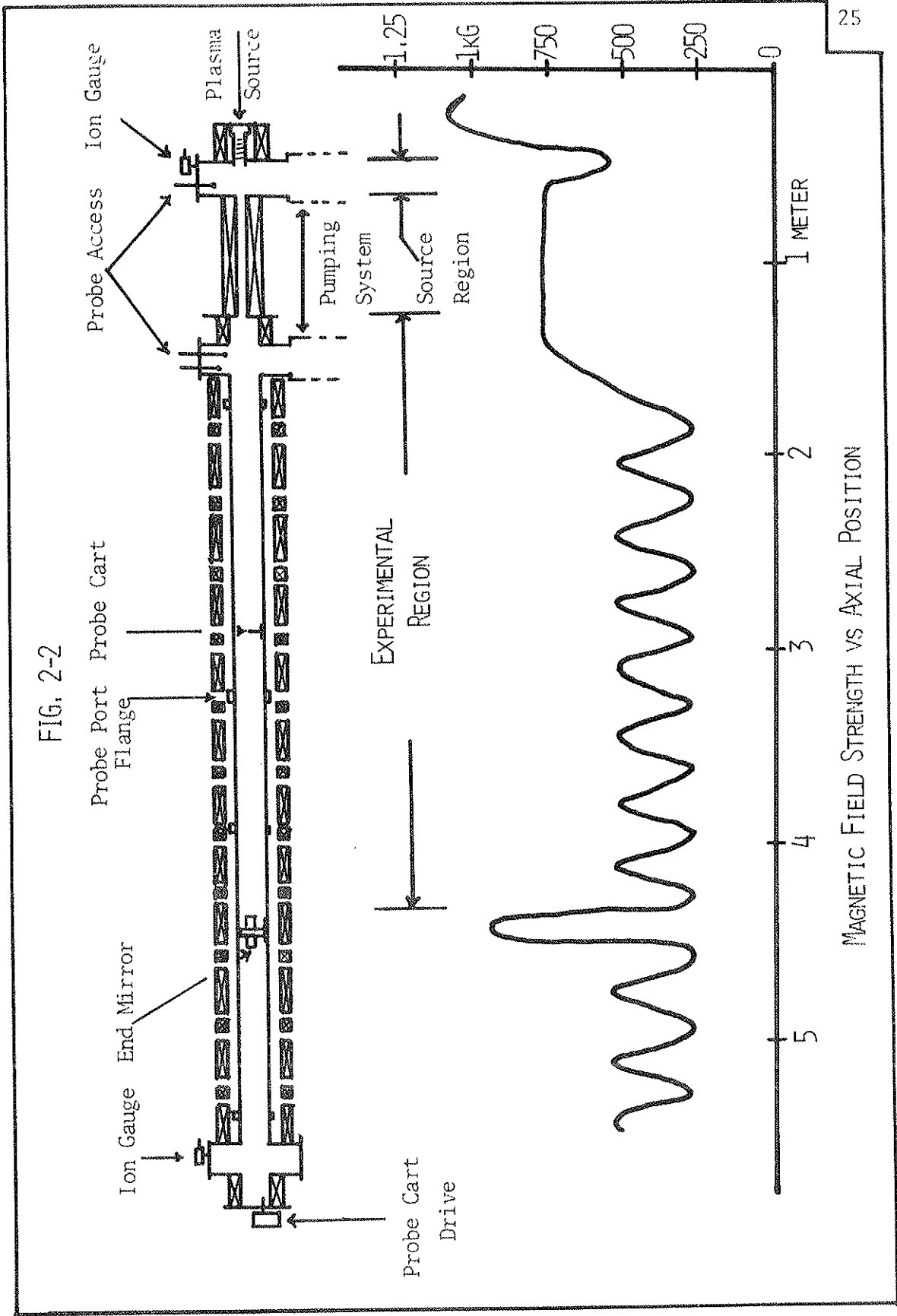


FIG. 2-2

Figure 2-3 The Linear Multi-Mirror: present configuration.

FIG. 2-3

PROBE ACCESS

SOURCE

+1.25

GAUSS

+1KG

+750

+500

+250

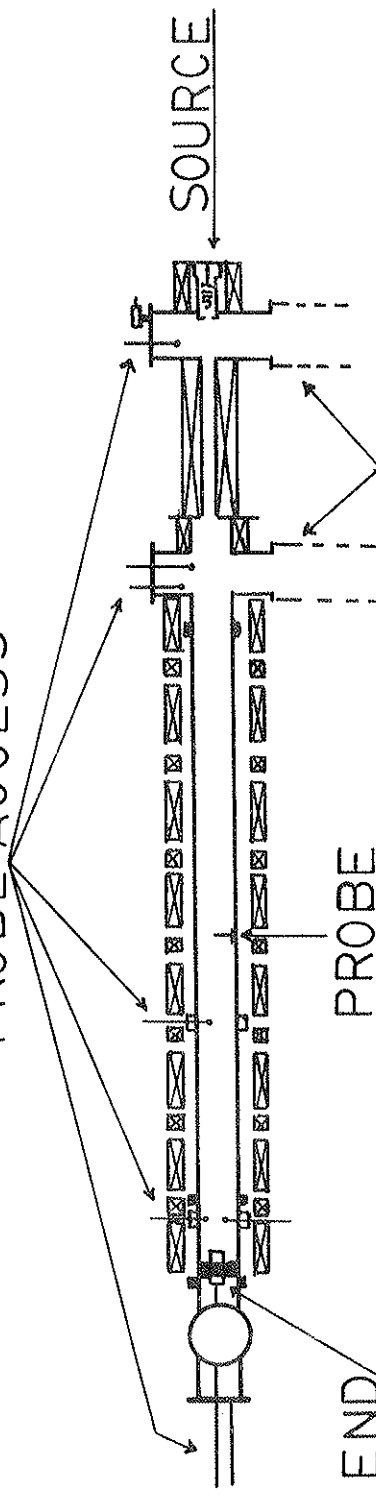
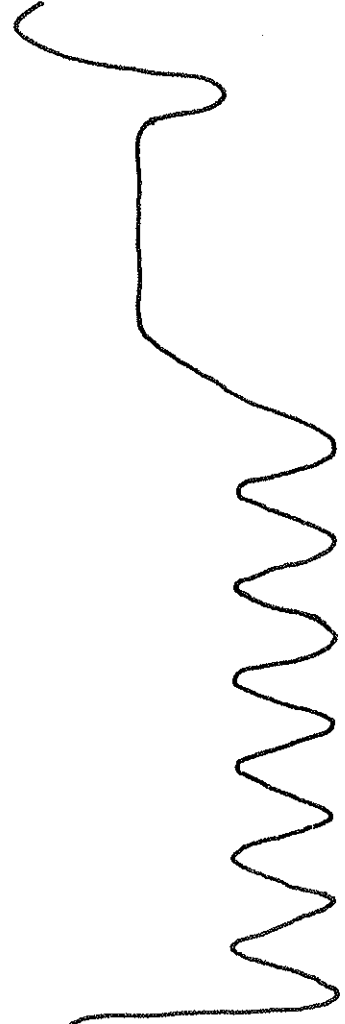
PUMPING

PROBE
CART

END/
MIRROR

Z, METER

5 4 2 1



trapped electron instability and, most recently, the trapped electron instability driven by finite Larmor radius effects and ultra low frequency oscillations (Chapters 5 and 6).

The changes which were made to the LMM have allowed us to significantly expand the range of plasma parameters which we can explore without losing the capability to study the interchange instability and the dissipative drift wave. They have also greatly improved our access to the experiment for diagnostic purposes.

A detailed description of the device in its present configuration (Fig. 2-3) will now be presented.

Vacuum system

The vacuum chamber of the LMM consists of several interconnected sections of Pyrex Conical* pipe. The vacuum vessel has a 6" (15.2 cm) inner diameter except in the pumping column which has an ID of 1.5" (3.8 cm). The entire vacuum chamber is 4.1 m long with a total volume of $8.4 \times 10^4 \text{ cm}^3$.

The experiment is roughed down from atmospheric pressure by a mechanical pump (Leybold-Hereaus model DK-45) with a pumping speed of 650 l/min. The pressure is then reduced to its base value of 1×10^{-7} Torr by two oil diffusion pumps charged with Dow Corning DC 704 silicon pump oil. A 6" (15.2 cm) diffusion pump (Consolidated Vacuum Company model PMC-1440) with an unbaffled pumping speed of

*Trade name of the Corning Glass Works, Corning, N. Y. 14830

1440 l/s is mounted at the bottom of the source region. A water cooled chevron baffle is used to reduce backstreaming of the pump oil but also lowers the pumping speed to one half of its unbaffled speed. This diffusion pump is backed by a 500 l/min mechanical pump (Welch model 1397). A molecular sieve foreline trap is used to prevent backstreaming of the forepump oil.

When the differential pumping column was added, a 10" (25.4 cm) diffusion pump (CVC model 4100) with an unbaffled pumping speed of 4100 l/s was installed at the entrance to the multimirror region (Fig. 2-2). This pump is also topped with a water cooled chevron baffle with a corresponding reduction in pumping speed. It too is backed by a 500 l/min mechanical pump (Welch model 1397) with foreline trap. Both diffusion pumps are protected from loss of cooling water by overheat cutoff switches and from overpressure by an interlock controlled by an ion gauge metering circuit.

The vacuum is monitored by thermocouple gauges (Veeco model DV-1M) for pressures in the range 1 atm - 1 micron. Similar gauges are used to measure the foreline pressure on the diffusion pump systems. For pressures between one micron and the base pressure, two Baynard-Alpert ionization gauges (one Westinghouse W5966 and one Varian 563 gauge tube) are used. One tube is located at the top of the source region and the other is located at the end of the experimental region so that the pressure differential between these two regions can be measured. By selectively adjusting the throttling type

gate valves over the two diffusion pumps, while gas is bled into the source region, this pressure differential can be varied over the range $1 \leq \Delta P \leq 200$ where ΔP is the pressure in the source region divided by the pressure in the experimental region.

Magnets

Five independently powered sets of electromagnets are used to create the DC magnetic fields which contain the plasma and to provide the resonance magnetic field for the plasma source. All the magnets are water cooled during operation and are protected against loss of cooling water by water pressure cutoff switches. The power supplies for three of the magnet sets are shared with the DC machine so a series of switches and interlocks are used to insure that power is not diverted to the wrong experiment.

Two magnets are used to create the magnetic field for the plasma source. By using two coils, both the amplitude of the magnetic field and the gradient of the field strength can be varied without moving the source assembly. The first coil was made by winding 3500 turns of #14 gauge magnet wire on a spool made from two 10" (25.4 cm) diameter copper plates connected by a 3" (7.6 cm) long piece of 2" (5.1 cm) ID \times 1/8" (.32 cm) W copper pipe. Heat conducting compound was applied between the layers of turns to help transport the heat from the center of the magnet to the two water cooled endplates. This coil is powered by a filtered DC power supply which produces a continuously variable current from 0 to 5 A at a maximum voltage of 5 V. The

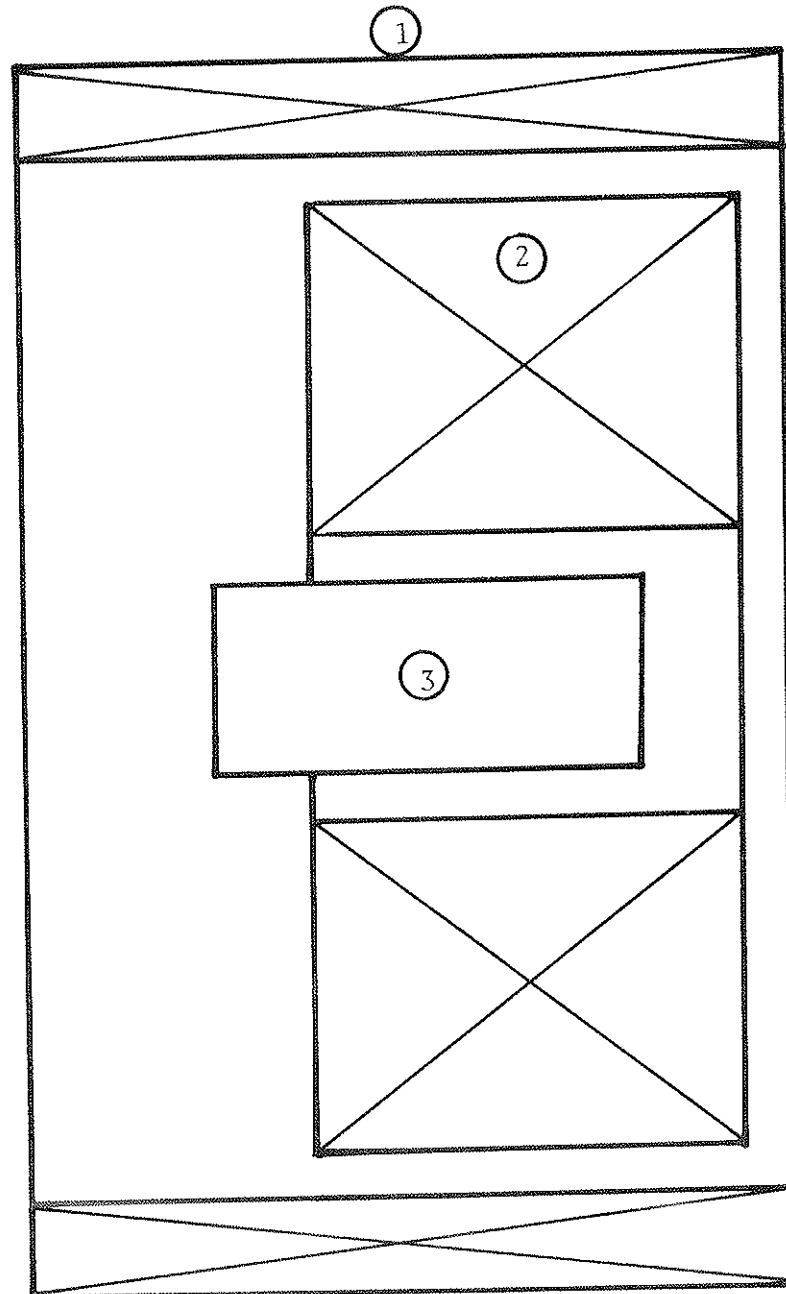
coil is typically operated at 3.8 A which produces an on-axis field of 650 Gauss.

The second source magnet is made of three layers of 1/4" (.64 cm) copper tubing with 22 turns per layer for a total of 67 turns. The coil is 6" (15.2 cm) long with an ID of 11" (27.9 cm). It is fitted around the wire coil and is biased so that the fields from the two coils add. It is powered by the "Cube" power supply which provides a highly filtered, continuously variable current from 0 to 350 A at a maximum of 50 volts. This magnet is typically operated at 260 A which produces an on-axis field of 680 Gauss (Fig. 2-4). An identical coil is located at the end of the differential pumping column. It is wired in series with the source coil so that it also produces an on-axis field of 680 Gauss at 260 A.

There are two coils around the differential pumping columns which constrict the plasma so that it passes through the column. These coils were made in the manner described by Fonck.¹ A total of 70 turns of 1/4" (.64 cm) copper tubing were wound in two layers along the 9.5" (24.1 cm) length of each coil. The inner diameter of the coils is 5" (12.7 cm) which allows them to fit around the connecting collars of the Pyrex tube in the pumping column. These magnets are powered with an Arc Welder supply which is capable of providing up to 400 A at 30 V. A balanced, 3 phase variac is used to change the current to the coils from 0 to 400 A. At 220 A the on-axis field created by these magnets is 790 Gauss.

Figure 2-4 Schematic representation of the coils which produce the resonance magnetic field for ECRH. The multi-mirror region lies to the left in this figure.

FIG. 2-4
ARRANGEMENT OF SOURCE COILS



- ① 67 TURN "CUBE" COIL
- ② 3500 TURN WIRE COIL
- ③ CONICAL HELIX

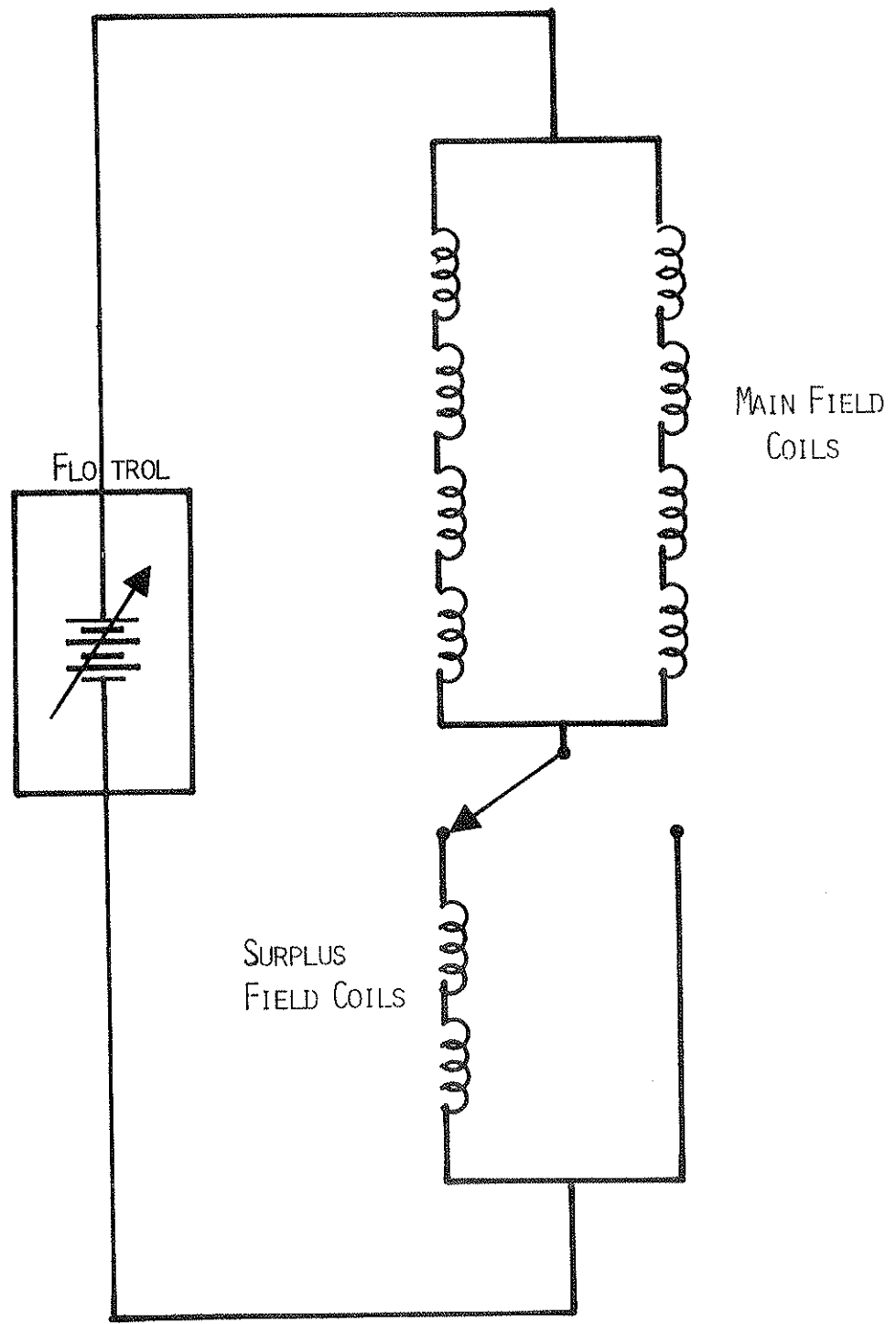
NO SCALE

The multimirror field in the experimental region is created by two independent magnet sets. The basic solenoidal field is supplied by the eight "Main Field" coils. These coils consist of 60 turns of 1/4" (.64 cm) copper tubing in two layers. They are 8" (20.3 cm) long and have an 11" (27.9 cm) ID. They are powered by the Flotrol power supply, which is capable of providing up to 400 A at 50 V. A high or low range of currents from the Flotrol is selected by a front panel switch on the power supply. The low current range is 20-100 A (continuously variable) and the high range is 200-400 A (continuously variable) with the eight Main Field coils connected to the Flotrol in a balanced arrangement of four coils in series in parallel with the other four coils in series. In order to obtain currents in the 100-200 A range, a switch was installed in the circuit which allows two surplus Main Field coils to be connected in series with the eight coils on the experiment (Fig. 2-5). Since the Flotrol works more like a voltage source than a current source, the increased load reduces the supply current of the high range to the desired values. At a Flotrol current of 200 A the Main Field coils produce an on-axis field of 280 Gauss.

The second set of field coils determines the degree of bumpiness of the magnetic field in the experimental region. These "corrector coils" were made by winding three layers of 1/2" (1.27 cm) diameter copper tubing. Each layer consists of four electrically parallel sections of tubing. The seven corrector coils are powered, all in

Figure 2-5 Schematic representation of the wiring of the eight Main Field coils. The two surplus Field coils are switched into the circuit to load down the Flotrol power supply into a previously unattainable range of currents.

FIG. 2-5



SCHEMATIC OF MAIN FIELD COIL WIRING

series, by the Magnflux power supply. The Magnflux is capable of supplying up to 4 kA at 12 V, but only in a step-wise variable fashion. To increase the usefulness of this power supply, C. Strawitch and D. Grubb added a network of filament transformers and variacs to the internal wiring of the Magnflux so that the current can be varied almost continuously between the stepped values (Fig. 2-6). The direction of current flow to the corrector coils is controlled by reversing the power leads to the LMM at the switch which directs the Magnflux current to either the DC machine or the LMM. For a Magnflux current of 1200 A* the corrector coils produce an on-axis field of 160 Gauss.

The on-axis field strength and mirror ratio were determined by R. Fonck¹ by sweeping a Hall probe down the axis of the LMM using the probe cart system (Fig. 2-7 and 2-8). He then empirically determined the mirror ratio and the average field strength as functions of Flo-trol current (I_F) and the Magnflux current (I_M). For a mirror ratio defined by $M = B_{MAX}/B_{MIN}$ and an average field strength defined by $\bar{B} = (B_{MAX} + B_{MIN})/2$ the relationships are

$$\bar{B} = 1.19 I_F \pm 0.103 I_M$$

*We have recently learned that the front panel meter on the Magnflux reads 1-1/2 times the actual current so that 1200 A on the meter is actually 800 A to the coils. Since all of the following formulas were derived according to the readings on the front panel meter, it is this value which should be used when calculating the magnetic field configuration.

Figure 2-6 Schematic representation of the circuitry which was wired into the Magnflux power supply to make the available current values analog instead of digital.

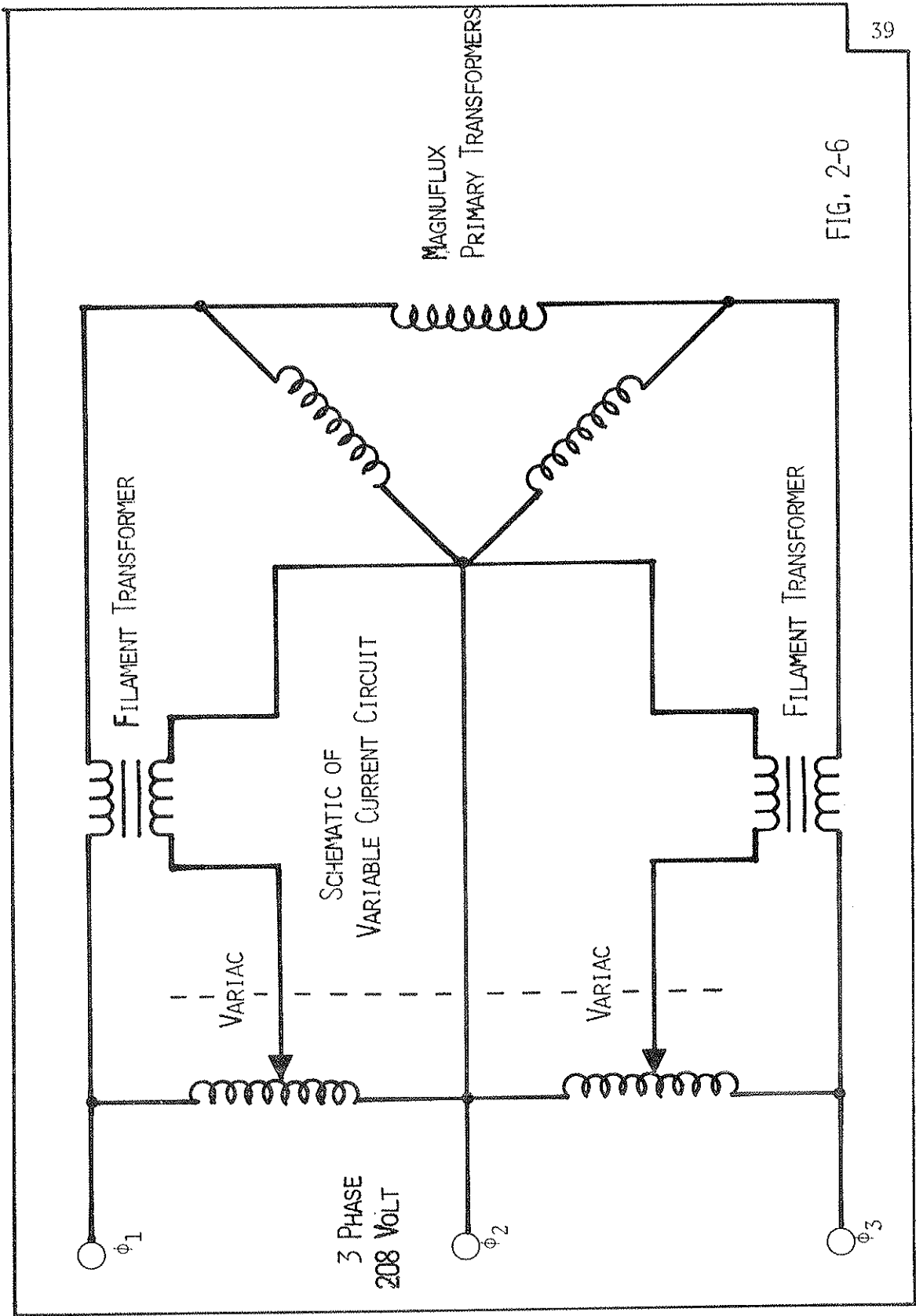


FIG. 2-6

MAGNIFLUX
PRIMARY TRANSFORMERS

FILAMENT TRANSFORMER

FILAMENT TRANSFORMER

SCHMATIC OF
VARIABLE CURRENT CIRCUIT

VARIAC

VARIAC

3 PHASE
208 VOLT

Figure 2-7 Magnetic field strength (as detected by a Hall probe) versus axial position in the Linear Multi-Mirror for a uniform magnetic field.

FIG. 2-7
UNIFORM FIELD, $M = 1.02$

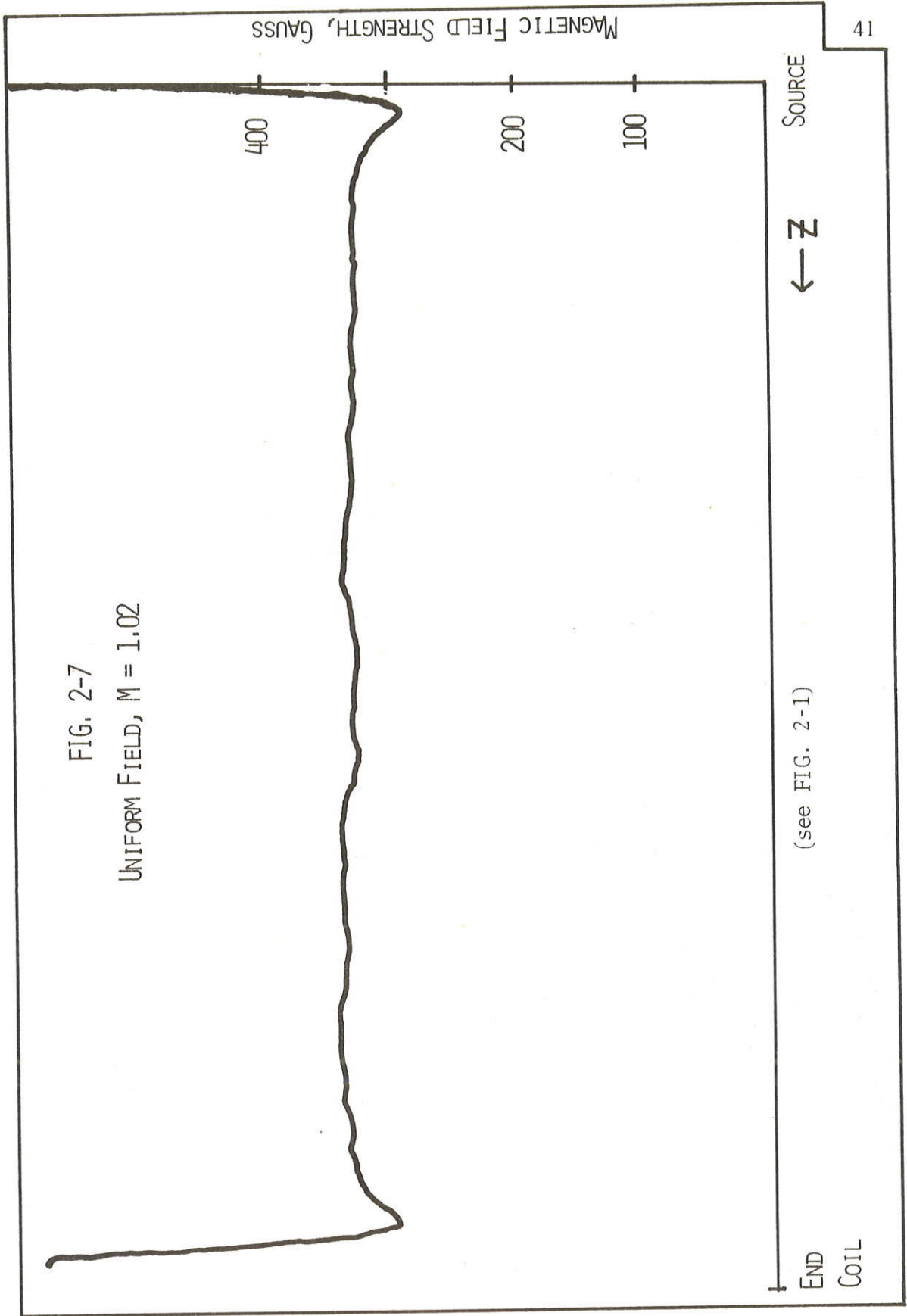
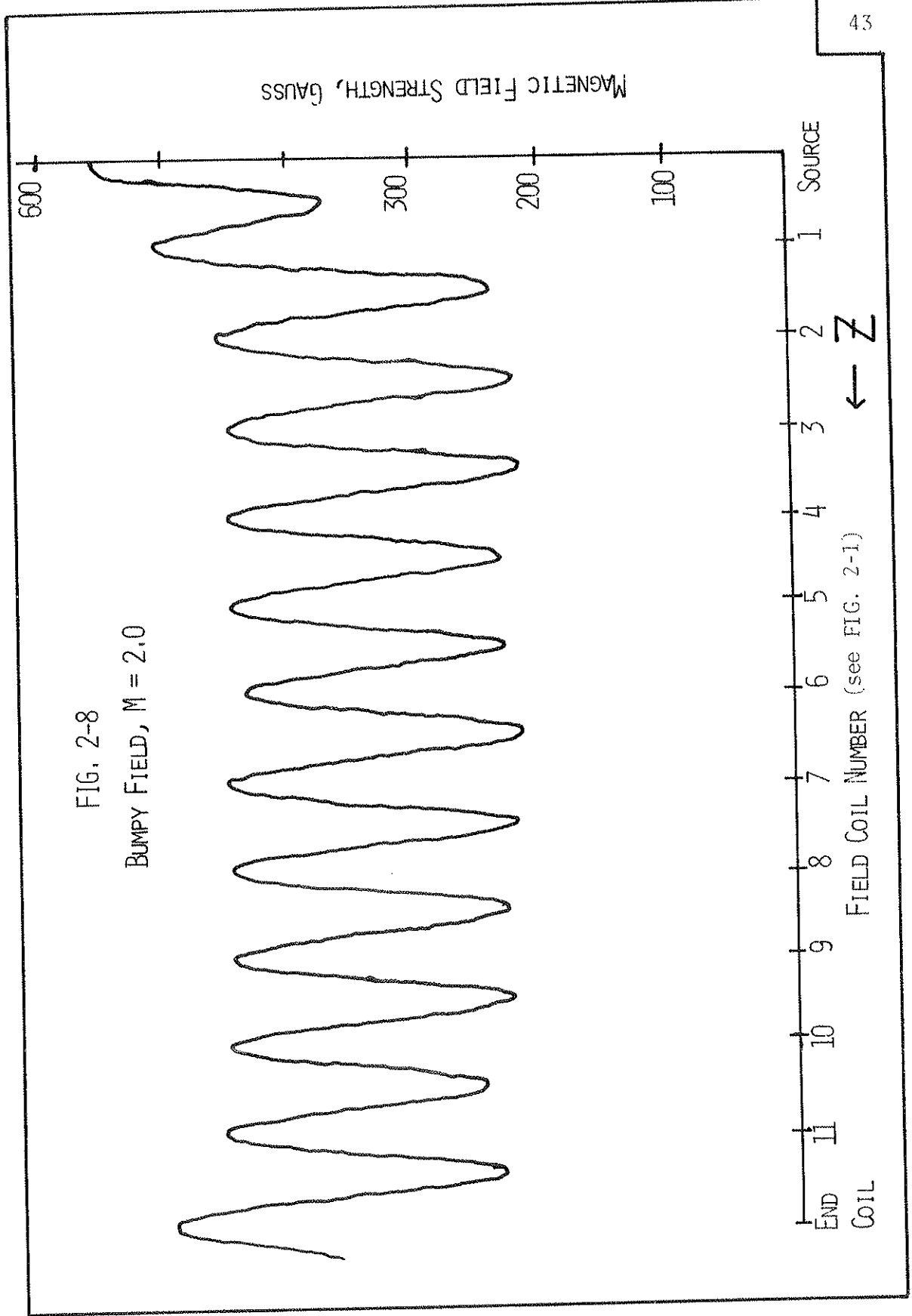


Figure 2-8 Magnetic field strength (as detected by a Hall probe) versus axial position in the Linear Multi-Mirror for a bumpy magnetic field.

FIG. 2-8
BUMPY FIELD, $M = 2.0$



$$M = \frac{1.38 I_F \pm 0.0785 I_M}{I_F \pm 0.127 I_M}$$

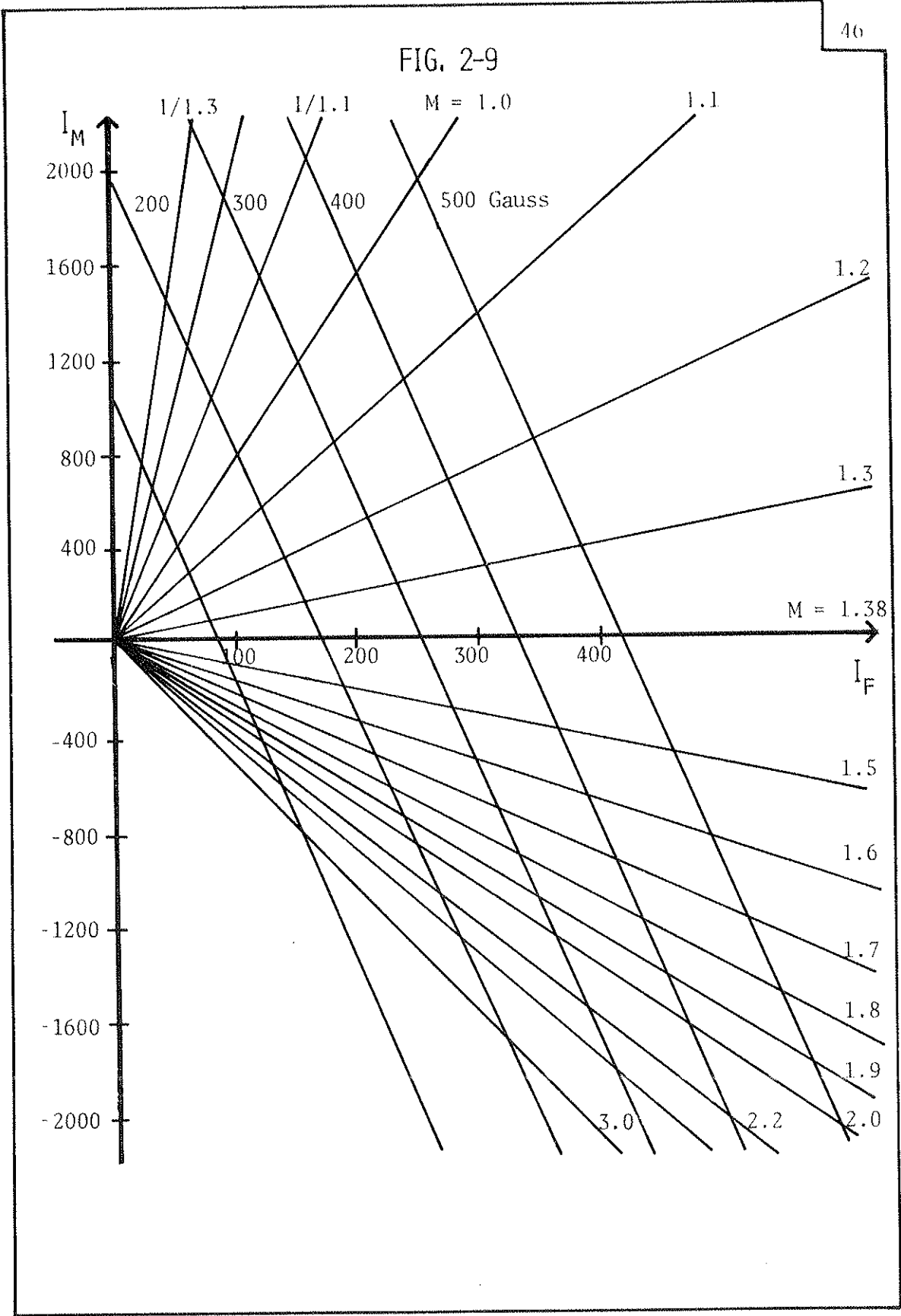
for the mirror cell connection length of 13.6" (34.5 cm). The (+) and (-) sign indicate whether the corrector coil field is adding to or subtracting from the main field, respectively. Lines of constant M and \bar{B} are plotted in Fig. 2-9 as functions of I_F and I_M .

Rough field alignment is accomplished by visibly aligning the plasma column on the centerline of the machine. For this purpose four small wires separated by 90° in azimuth have been mounted along the length of the outside of the vacuum chamber to provide parallax free alignment. This method is usually accurate to ± 5 mm. Precise field alignment is obtained using the electron beam built by C. Strawitch. We have found that using Neon as the fill gas at a pressure of 2×10^{-4} Torr a highly visible beam can be fired along the length of the machine. The same four wires are then used for centering the beam.

During the studies of the drift and interchange instabilities the plasma column was terminated on a moveable, metal endplate. In this mode of operation the plasma diffused down the length of the experiment and terminated on the endplate. This resulted in an axial density gradient. In order to eliminate this density gradient, improve the confinement, and create a class of pseudo-transit particles, we replaced the endplate with a moveable mu-metal cylinder (3.8 cm diameter \times 14 cm). This cylinder is situated inside of the vacuum chamber

Figure 2-9 Lines of constant magnetic field strength at varying mirror ratio and lines of constant mirror ratio at varying field strength as functions of the Magnflux current, I_M , and the Flo-trol current, I_F .

FIG. 2-9



and centered within one of the Main Field coils. The magnetic field at the face of the cylinder is 2-1/2--3 times the field strength inside the other field coils. This provides an end mirror which is approximately equal in height to the mirror at the end of the differential pumping column (Fig. 2-3). The mu-metal cylinder is encased in glass so that the plasma is not "line tied" on the face of the mu-metal.

Probe access ports are located along the length of the experiment (Fig. 2-3). There are two ports above the source region, one of which is a swivel port. There are two ports at the end of the pumping column where the experimental region begins; one of these ports swivels. The side port assembly contains four probe access ports mounted at 90° intervals. The end port assembly also has four ports at 90° intervals. These end ports can accept probe assemblies up to 1-1/2" (3.8 cm) in diameter or a swivel port assembly. The end plate has a 1" (2.5 cm) axial viewing port and two axial probe ports. A final probe access assembly is the probe cart system.¹ By means of a remotely controlled synchronous motor mounted outside the vacuum chamber, the probe cart can be swept along the length of the experiment. The cart is capable of accepting up to three probes at one time. Generally, however, to avoid perturbing the plasma only one probe is used.

Plasma sources used in the LMM

Since the LMM is of modest size with relatively low magnetic field strength, it was logical to look for a plasma source which would

ionize low mass gases (H₂, He, etc.) and produce warm electrons with cold ions. Lisitano coils of the interdigital⁶ and helical⁷ types were logical choices. These sources create the plasma by coupling microwave power into the plasma by electron cyclotron resonance heating (ECRH).

For absorption of microwave power at the upper hybrid frequency the resonance magnetic field is determined by the relationship

$$f_a = f_{UH} = \sqrt{f_{pe}^2 + f_{ce}^2} = \frac{1}{2} \sqrt{\frac{4\pi n e^2}{m_e} + \left(\frac{eB}{m_e}\right)^2}$$

$$= 2.83 \sqrt{n(10^{12} \text{ cm}^{-3}) + B(\text{kG})^2} \text{ GHz}$$

where f_a is the applied frequency, f_{UH} is the upper hybrid frequency, f_{pe} is the electron plasma frequency, and f_{ce} is the electron cyclotron frequency. For plasma densities $\lesssim 10^{11} \text{ cm}^{-3}$, this reduces to $f_a \approx f_{ce}$ ⁸. For an applied frequency of 3.0 GHz the resonance magnetic field is $B = 1060$ Gauss.

The microwave power for the LMM is supplied by a Raytheon 4J63 magnetron. This tube supplies a nominal 50 watts at an adjustable frequency of 2.985 - 3.385 GHz. The tube operates most efficiently at 3 GHz and so is operated at that frequency. In order to isolate the microwave supply from variations in reflected power a P & H Laboratories model B1-526317 circulator is inserted into the microwave line to provide 20 db of isolation. A General Radio model 874-LK10L line stretcher is also inserted into the line to improve the impedance

match between the power supply and the plasma source.

The initial operation of the LMM employed an interdigital Lisitano coil as the plasma source⁶ (Fig. 2-10). This source typically yielded plasma densities in the range $10^9 \text{ cm}^{-3} \leq n \leq 10^{10} \text{ cm}^{-3}$ using a neutral gas pressure in the source region in the range $1 \times 10^{-4} \leq P_N \leq 5 \times 10^{-3} \text{ Torr}$. This source worked admirably for the studies of the drift and interchange modes. However, to operate the LMM in the trapped electron regime, a density on the order 10^{11} cm^{-3} was required. In order to obtain this density we designed a simpler and more efficient slow wave antenna.

Design considerations -- Slow Wave Antenna

In order to heat the electrons efficiently by ECRH it is desirable to have as much of the electric field as possible perpendicular to the resonance magnetic field. To accomplish this, the coil was designed so that $C/\lambda \approx 1$, where C is the circumference of the helix and λ is the wavelength of the microwaves used to power the coil. Coils which satisfy this condition have a charge distribution as illustrated in Fig. 2-11. As shown in this figure there is also an electric field between the helix and the wall of the coaxial cylinder which houses the coil. It is not surprising, therefore, that it is possible to break down a plasma in this region also. Consequently, the diameter of the plasma produced by this source is approximately equal to the ID of the housing cylinder. By varying the ratio of r_H to r_C (Fig. 2-11) the fine structure of the plasma gradients can be

Figure 2-10 a. The Lisitano coil (shown in half scale) is made by milling an 1/8" slot in a copper pipe, in the pattern shown here. There are eight equally spaced slots on a pipe of 2" ID and 1/16" wall. The quarter-wave slot at the microwave feed avoids short circuiting the input current.

b. The source assembly is shown full size. Gas is fed in at (A), and microwaves at (B) through a modified Type-N microwave coax connector. The vacuum seal is teflon (C), and connection to the Lisitano coil is made at (D). The Lisitano coil is hard soldered into its brass end-plug at (E). The pipe (F) is stainless steel, the collimator (G) is copper.

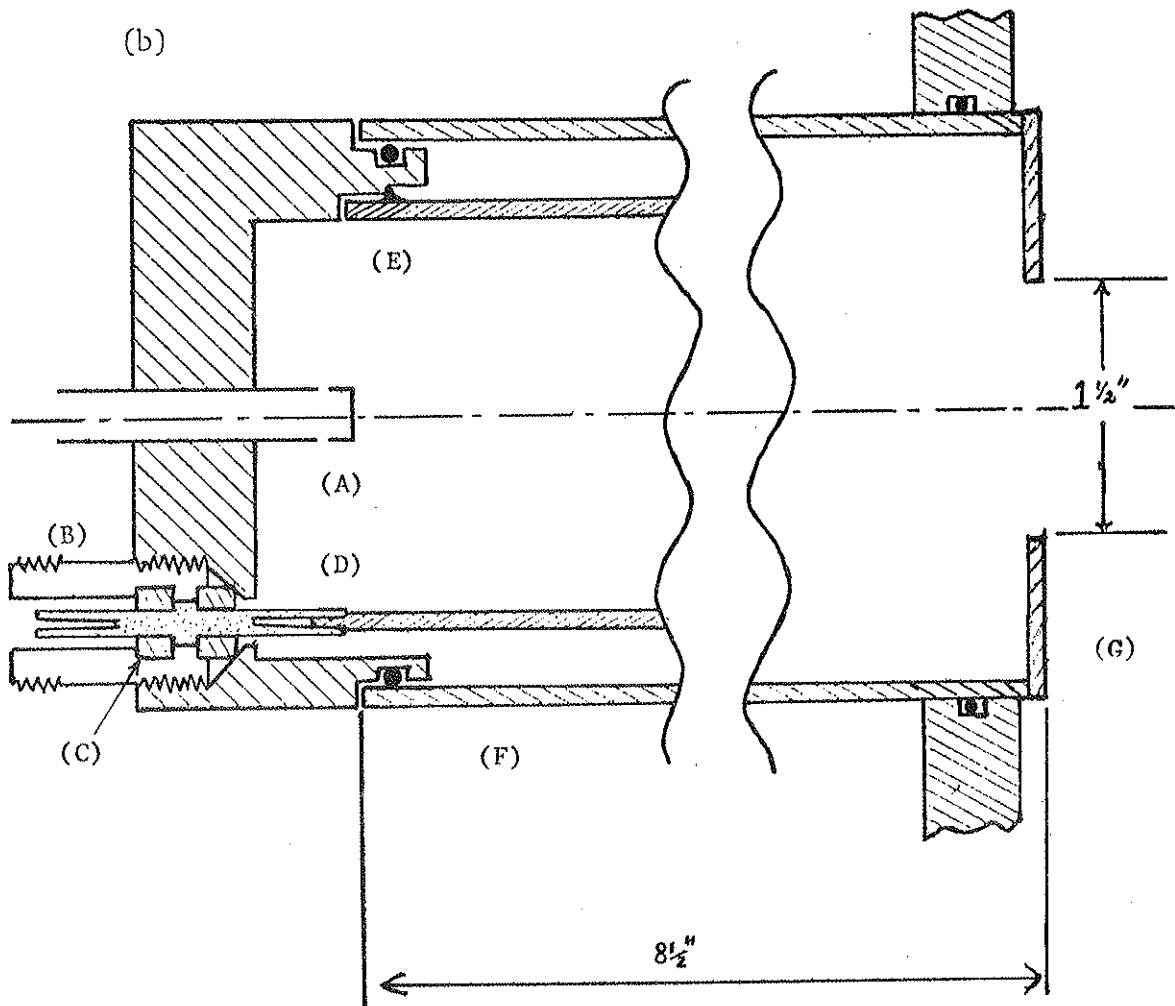
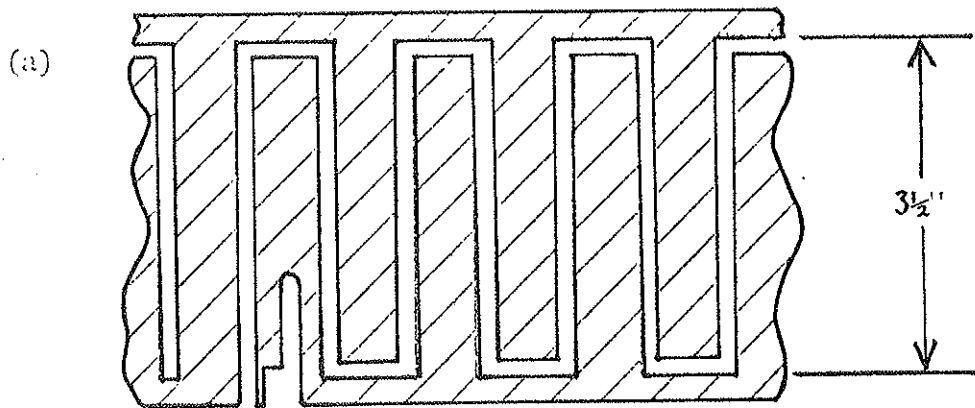
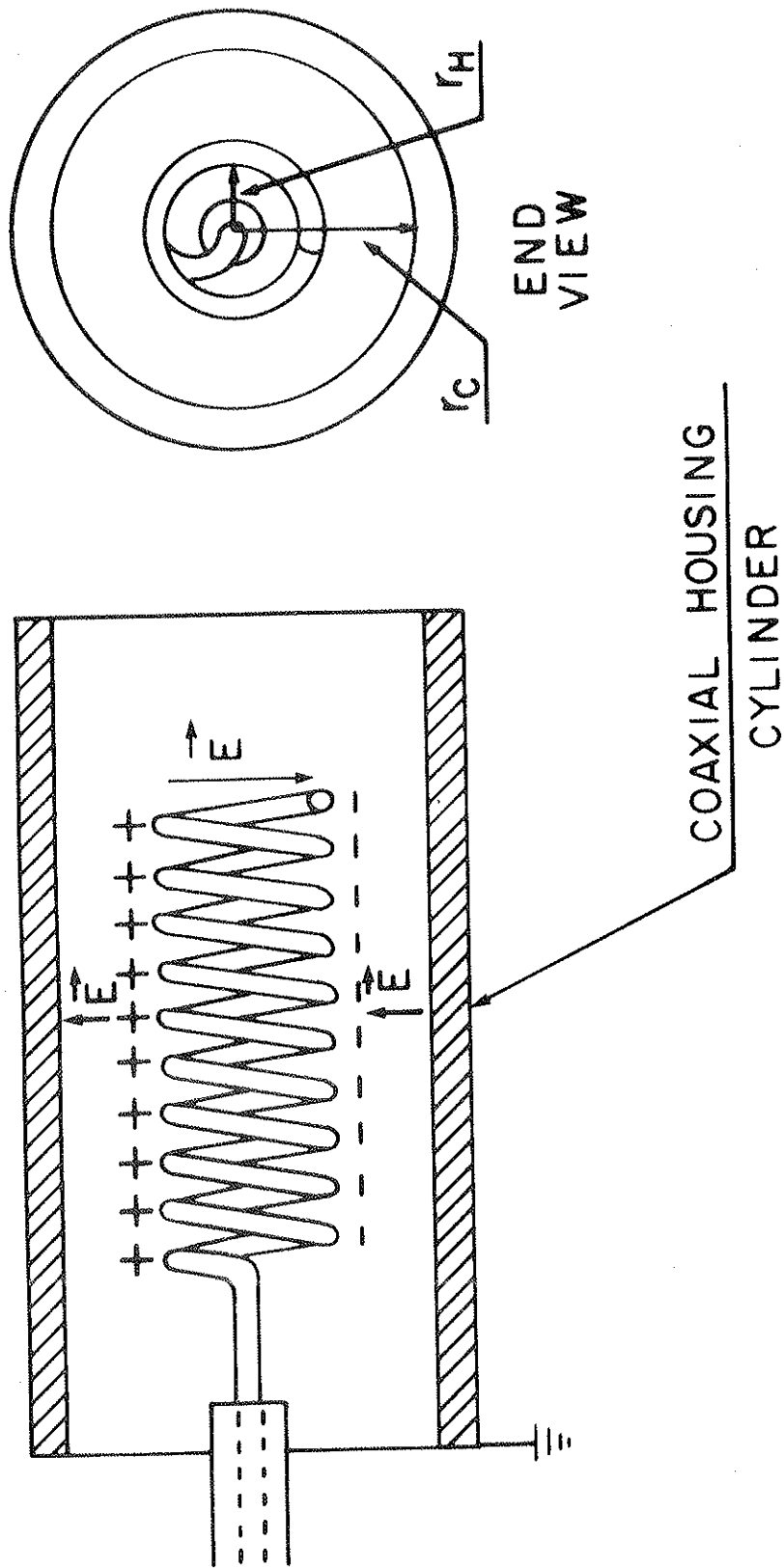


Figure 2-11 Charge distribution and electric field for a conical helix housed in a grounded cylinder.

FIG. 2-II



altered.

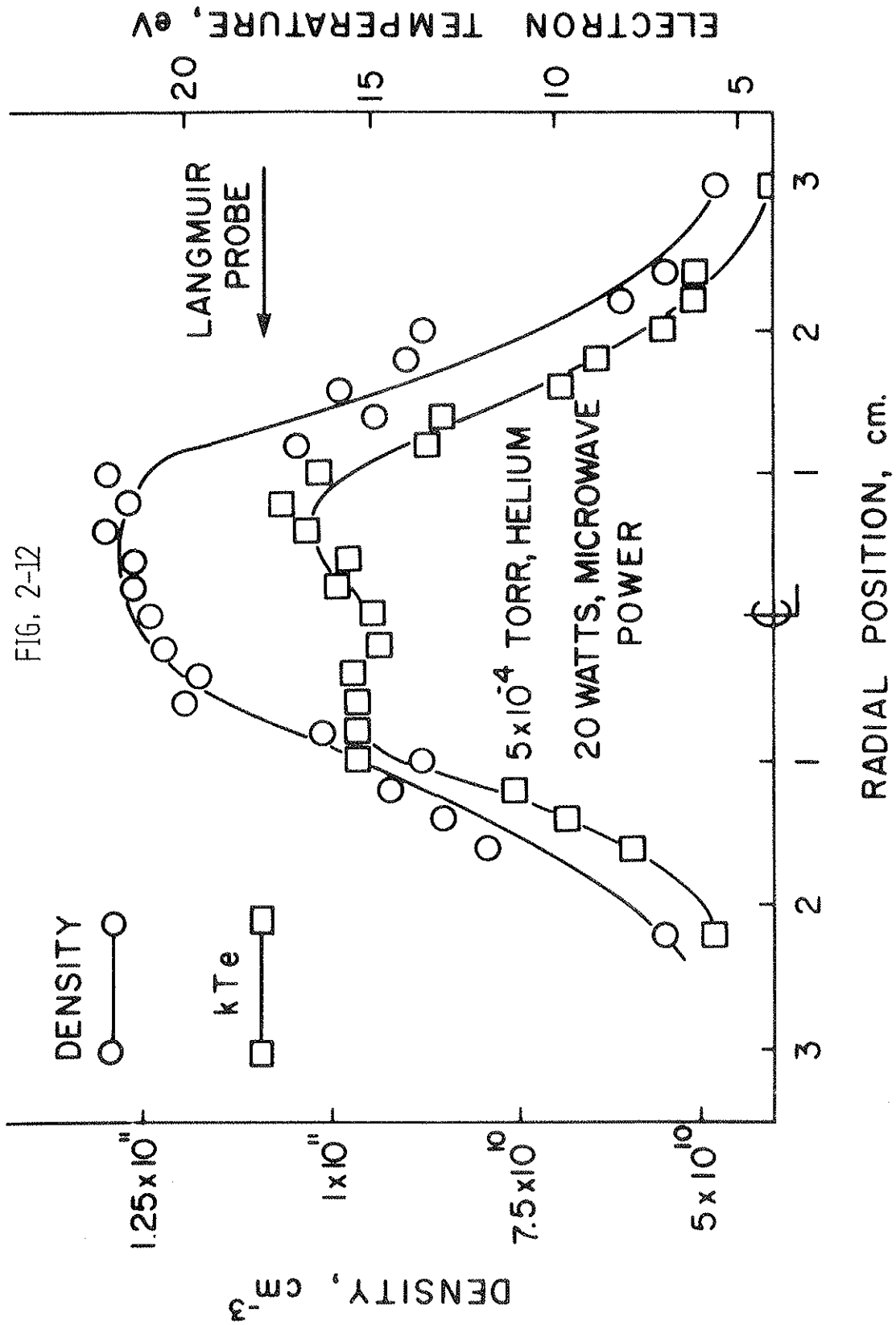
After the initial breakdown of the plasma, cylindrical Lisitano coils have shown a tendency to produce a plasma which is peaked in temperature and density on the field lines which run along the inner diameter of the cylinder.⁹ This effect is probably caused by the strong absorption of the microwave energy at this point and a weakening of the on-axis electric field by the dielectric effect of the plasma. By tapering the helix, we created a series of concentric rings so that the outer peaks in the plasma temperature and density are smoothed out.¹⁰ The temperature and density of the plasma created by this source, therefore, peak on the center-line of the coils and not on the edges of the plasma (Fig. 2-12).

The coil was designed so that the length of the coil following the helical windings, L , was much greater than the wavelength of the microwaves, λ . We have not performed any experiments to determine the importance of this condition, $L \ll \lambda$, but experience with helical antennas operating in the axial mode indicate that it is necessary to satisfy this criteria in order to take advantage of the broadband nature of these coils. Kraus¹¹ also recommends that the coil have a ground plane diameter, $D \approx \lambda/2$, so this feature was incorporated into our design.

Construction

One of these source coils and the form upon which it was wound is shown in Fig. 2-13. It was produced by a bifilar winding of equal

Figure 2-12 Radial profiles of the density and the electron temperature in the source region of the LMM.



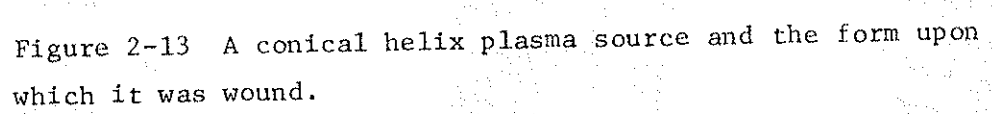
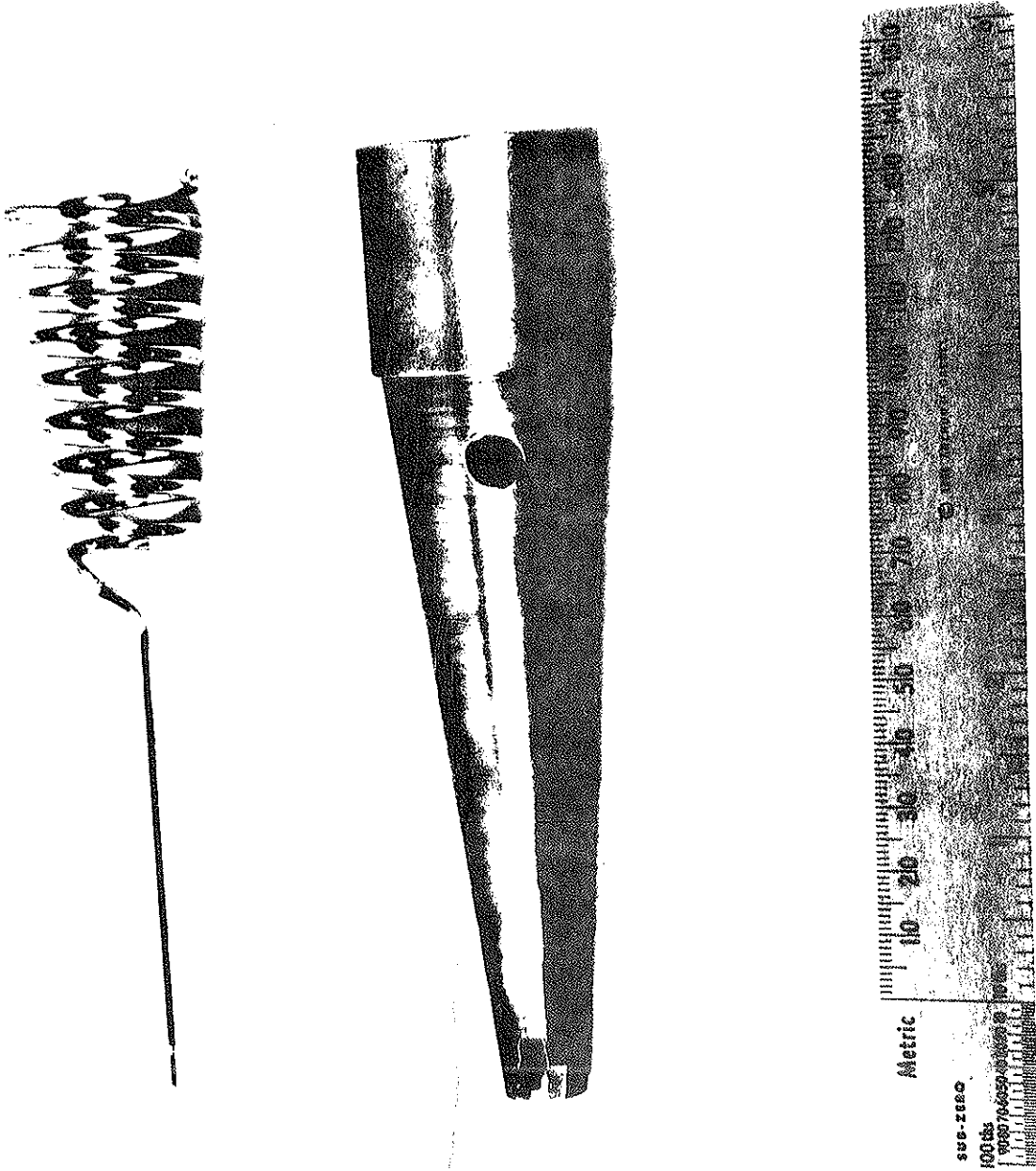


Figure 2-13 A conical helix plasma source and the form upon which it was wound.

FIG. 2-13



lengths of Beryllium-Copper (Berylco 25) rod and iron rod on a tapered iron form. The Be-Cu rod was chosen because it provides superior mechanical durability and still retains 25% of the conductivity of pure copper.

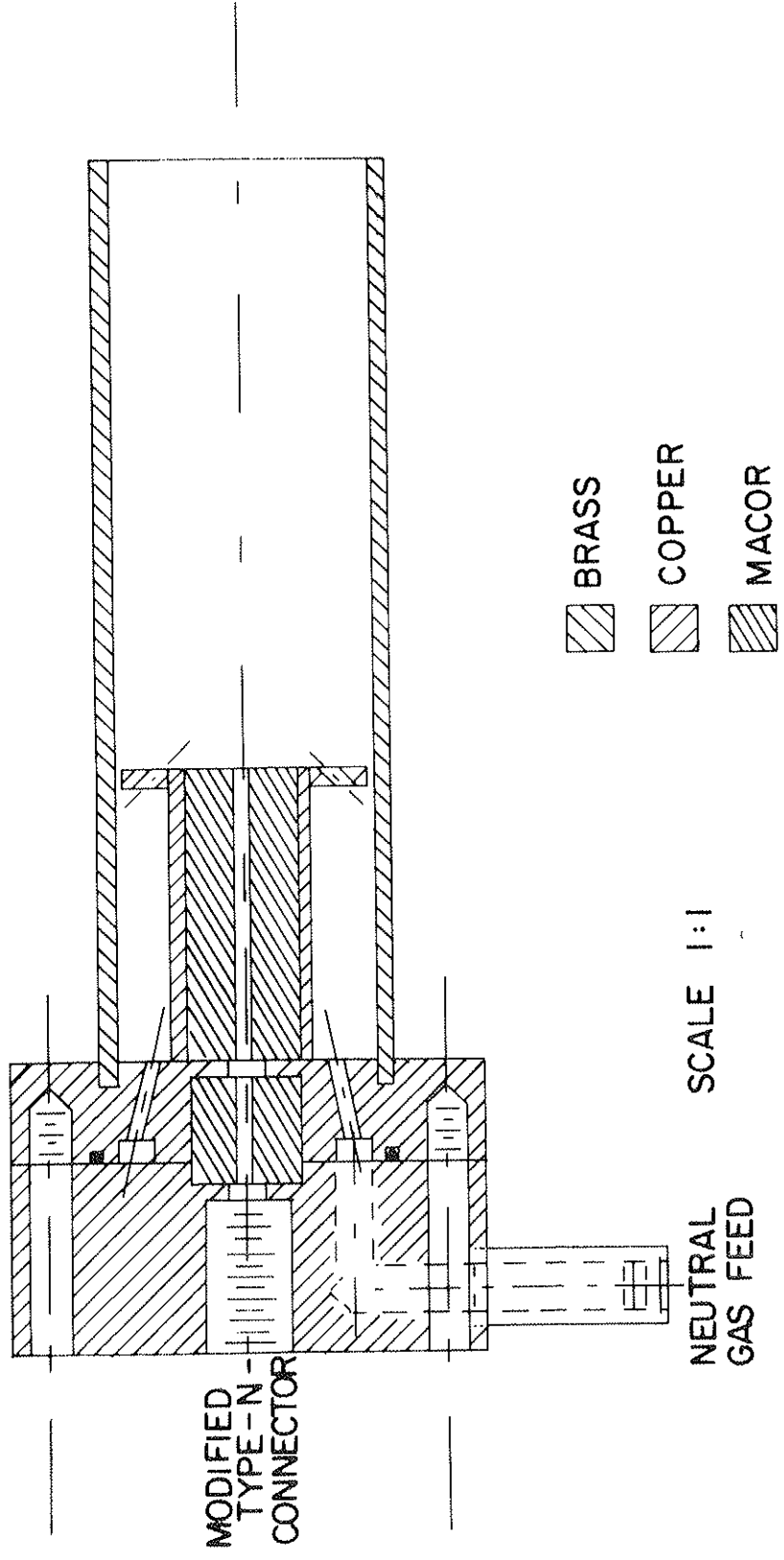
With the ends of the rods clamped to prevent deformation during heat treating, the coil was baked at 315°C for 2-1/2 hr to promote precipitation hardening of the Be-Cu rod. The coil was then left in the oven overnight for a slow cool down to insure that thermal stresses would not deform the finished coil. After complete cooling the coil was unclamped from the form, cleaned, and polished. The finished coil is plugged into a source assembly which serves as a vacuum feed-through (Fig. 2-14).

The source assembly was constructed so that the coil could be inserted into the vacuum vessel and positioned in a region of resonance magnetic field for ECRH. Care was taken to insure that the line impedance was 50 Ω from the microwave power supply to the first turn of the helical coil. The radiation impedance of an axial mode antenna is typically 100-200 Ω ¹¹, but varying plasma conditions change the load impedance. It was, therefore, deemed wise to include a line stretcher in the system to provide impedance matching. Experience has shown that this line stretcher does, indeed, improve the plasma production, but it is not essential to the operation of the source.

Finally, as shown in Fig. 2-14, the source assembly is also used to introduce the neutral gas into the coil region. The path which the

Figure 2-14 Cross sectional view of the assembly used to house the conical helix and introduce the neutral gas into the source region.

FIG. 2-14



gas follows is, by design, a tortuous one. In order to insure a uniform filling of the cylinder surrounding the helix, we constructed the source assembly so that the gas would be turbulent as it entered the source chamber.

Operation

The coil presently in use has been operating faultlessly for over a year. No form of direct cooling is provided to the coil. Two electromagnets are used to create the resonance magnetic field and to control the field gradient in the coil region. A standard operating field structure is shown in Fig. 2-15.

To date, plasmas of hydrogen, helium, argon, and neon have been produced. Neutral gas pressures in the range 2×10^{-5} Torr to 2×10^{-3} Torr yield plasma densities $10^{10} \text{ cm}^{-3} \lesssim n \lesssim 10^{12} \text{ cm}^{-3}$. These values of the density are roughly two orders of magnitude higher than could previously be produced in the same experiment using an interdigital Lisitano coil (Fig. 2-10). Electron temperatures are typically $2 \text{ eV} \lesssim T_e \lesssim 20 \text{ eV}$. The ion temperature in a similar experiment has been measured by Fonck and Guss using a Fabry-Perot interferometer.¹² They found $T_i \lesssim .1 \text{ eV}$ for a helium plasma. The ion temperature has not been measured for a hydrogen plasma; but results similar to those of I. Brown,¹³ who found $T_i \lesssim .2 - 2 \text{ eV}$ for a Lisitano coil plasma, may be expected.

Density and temperature profiles in the source region of the linear machine are shown in Fig. 2-12. The RMS noise level in this

Figure 2-15 Magnetic field configuration in the source region of the LMM.

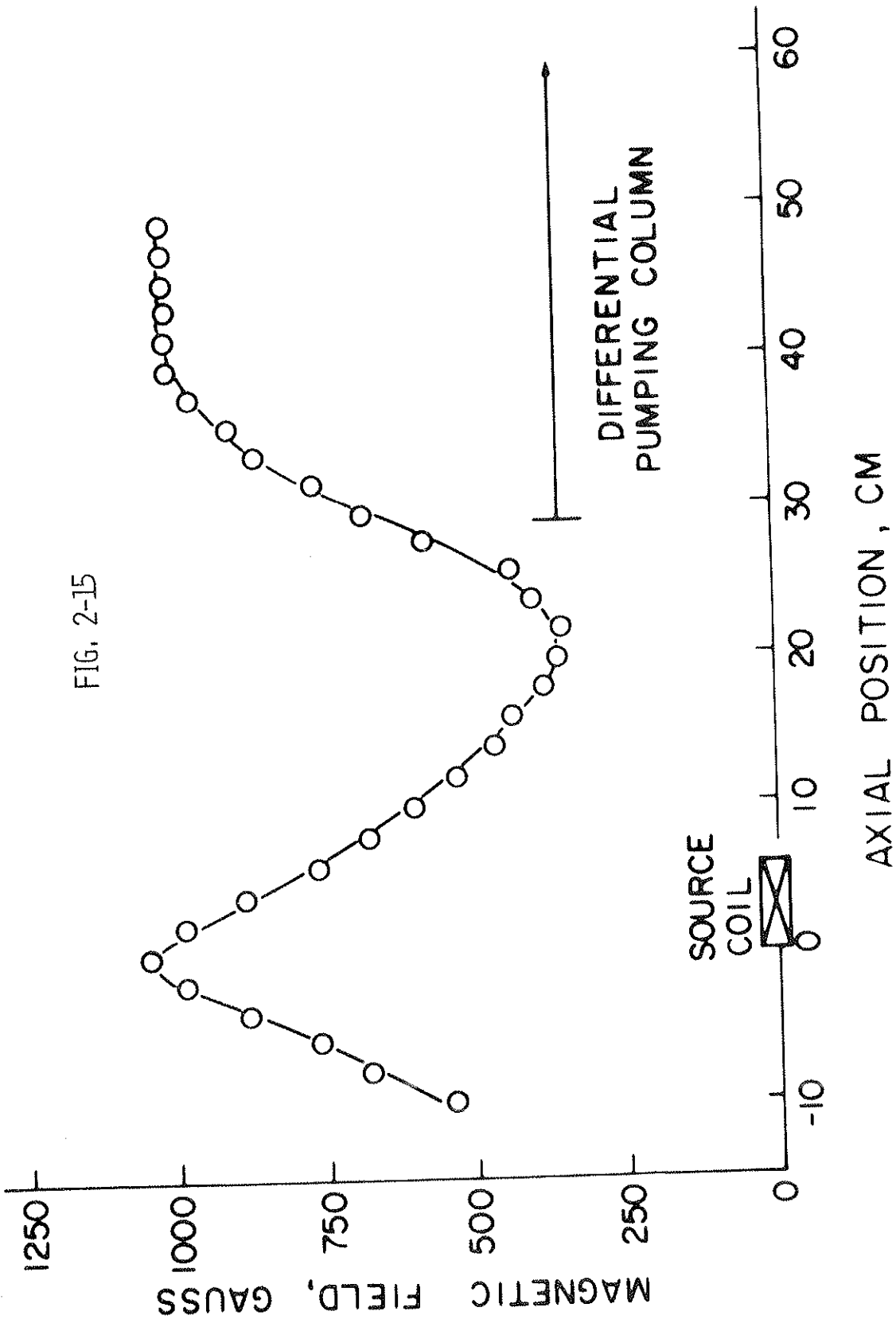


FIG. 2-15

region is typically 1-5%. It should be noted that due to the high degree of isolation provided by the differential pumping column there are significant differences in the density, temperature, and plasma gradients between the plasmas in these two regions.

References for Chapter 2

1. R. J. Fonck, Wisconsin Plasma Physics Report PLP 585 (1974)
2. R. J. Fonck, W. C. Guss, and D. M. Meade, Bull. Am. Phys. Soc., 18 ser. 2, 1320 (1973)
3. D. P. Grubb, G. A. Emmert, R. K. Richards, Wisconsin Plasma Physics Report PLP 616 (1975)
4. D. P. Grubb and G. A. Emmert, Wisconsin Plasma Physics Report PLP 717 (1977)
5. D. P. Grubb and G. A. Emmert, Wisconsin Plasma Physics Report PLP 719 (1977)
6. G. Lisitano, I. G. Brown, and J. G. Gorman, Princeton Plasma Physics Lab Report Matt-629 (1968)
7. G. Lisitano, M. Fontanesi, and E. Sindoni, Appl. Phys. Lett., 16, 122 (1980)
8. R. Prater, Ph.D. Thesis, Wisconsin Plasma Physics Report PLP 452 (1971)
9. M. Fontanesi and E. Sindoni, Il Nuovo Cimento, LXIVB, N1, 88 (1969)
10. A similar effect has been noted by Decker using a conical, drawn glass source. J. F. Decker and C. V. D'Amico, Rev. Sci. Inst., 41, 1431 (1970)
11. J. D. Kraus, Antennas, McGraw-Hill Book Co., Inc., New York (1950)
12. R. J. Fonck and W. C. Guss, Wisconsin Plasma Physics Report PLP 584 (1970)
13. I. G. Brown, Plasma Phys., 18, 205 (1976)

CHAPTER 3
DIAGNOSTICS

This chapter is divided into two sections: equipment and techniques. The equipment section describes the actual apparatus used to measure the plasma parameters. The techniques section describes two specific methods, which are not in common use, used to study the plasma: feedback stabilization and transfer function analysis.

Equipment

The primary diagnostic tools used to study the plasma in the Linear Multi-Mirror (LMM) are Langmuir probes. The probes are designed specifically to measure the plasma floating potential and the ion saturation current over the frequency range DC - 500 kHz. Both spherical and planar probes are used. Spherical probe tips give the highest degree of spatial resolution for a given collection area and can be made small enough to minimize perturbations of the plasma when radial profiles are taken. Spherical probe tips, especially small ones, though, do not exhibit good saturation of the ion current. Planar probes do show good saturation when the plane of the probe is perpendicular to the magnetic field; however, planar probes tend to be larger and, therefore, more perturbing.

The spherical probes are made by applying the flame of an oxy-gas or an oxy-acetylene torch to the end of a piece of #32 platinum wire so that the end of the wire melts and forms a bead due to the surface

tension of the liquid platinum.¹ With care, a highly spherical probe tip of almost any desired diameter can be made in this manner. Typically, probe tip diameters of .5 mm or 1.0 mm diameter are used. Both sizes satisfy the relationship $\lambda_{De} \ll r_p < \rho_i$ where λ_{De} is the electron Debye length, r_p is the radius of the probe tip, and ρ_i is the ion gyro-radius.

The remaining length of platinum wire is then inserted into a 7.5 cm length of Alumina tubing. (7.5 cm of tubing allows the probe tip to be inserted radially into the center of the plasma column without the main body of the probe being exposed to the plasma.) The exposed wire is soldered to the inner conductor of a shielded microdot cable. The entire assembly is sealed into a 1/4" (.64 cm) diameter glass tube with epoxy (Fig. 3-1).

Planar probes are made by punching platinum disks from 0.076 mm thick platinum foil using a variable hole diameter leather punch. The disk is then spot welded to a piece of #32 platinum wire. The rest of the probe is assembled in the same manner as a spherical tip probe.

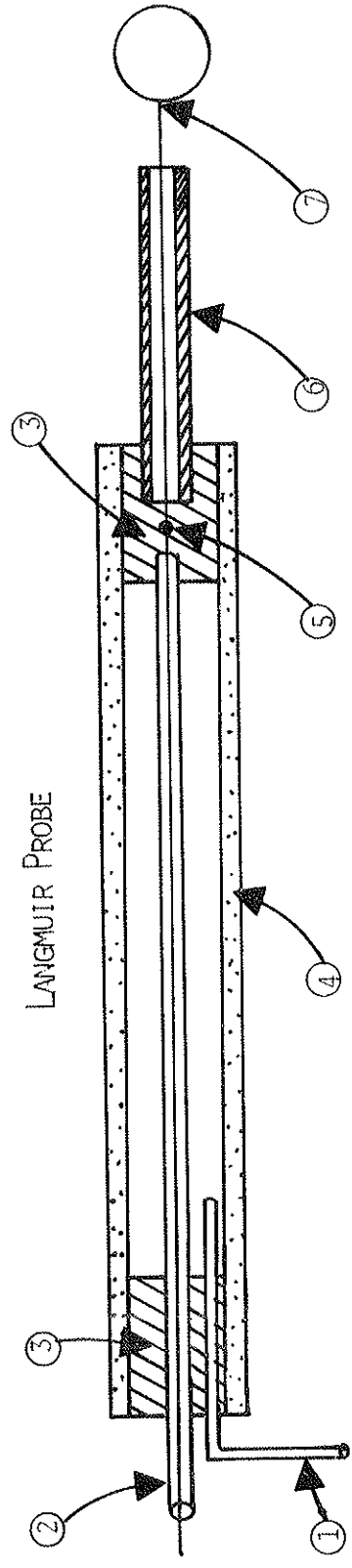
The circuit shown in Fig. 3-1 is used to bias a probe with respect to the machine ground. The current drawn from the plasma is measured as a voltage drop across the biasing resistor.

In the LMM these probes are used to measure the ion saturation current by biasing the probe strongly negative ($V_a = -22$ to -45 v). These probes are also used to determine the local values of the electron temperature and density by varying the bias from -90 V to $+90$ V

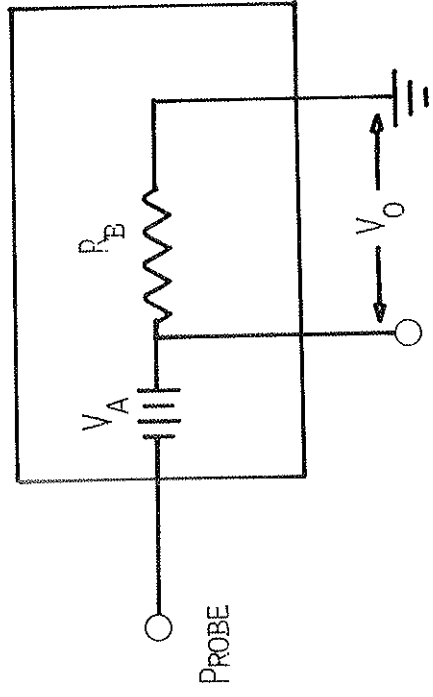
Figure 3-1 Construction of a typical Langmuir probe used in the LMM and the circuit used to bias it with respect to the machine ground.

FIG. 3-1

LANGMUIR PROBE



- ① TEFLON TUBE
- ② MICRODOT COAXIAL CABLE
- ③ EPOXY
- ④ 1/4 IN. DIA. GLASS TUBE
- ⑤ SOLDER JOINT
- ⑥ ALUMINA TUBE
- ⑦ PLATINUM BEAD AND WIRE



NO SCALE

to sweep out the probe I-V characteristic (Fig. 3-2).

A single tip Langmuir probe used to measure the ion saturation current is susceptible to changes in the floating potential. This problem arises basically due to the fact that the ion saturation current branch of the I-V characteristic (for most probes) is not absolutely independent of the biasing voltage but actually exhibits a slight slope. Due to this variation of I_{oi} with V , changes in the floating potential give rise to apparent changes in I_{oi} . In order to avoid these erroneous measurements, a second type of probe, commonly referred to as a double floating probe, is also used to measure the ion saturation current in the LMM. They are constructed in the same manner as the simple single probes (Fig. 3-3). The double probe obviously presents twice the physical obstruction to the plasma that a single probe does, but it has the advantage that the relative bias between the probe tips is a constant independent of change in the floating potential.

When either type of probe is used to draw a current from the plasma, the probe circuit should present a minimal impedance to the current flow. This restriction usually takes the form $R_B \ll V_a / I_{oi}$ where V_a is the voltage of the biasing battery and R_B is the biasing resistor.² The value of R_B should also be kept small so that the time constant of the circuit determined by $R_B C_p$ is small in order to extend the frequency response of the probe circuit. (C_p is generally determined by the parasitic capacitance of the coaxial cable used to

Figure 3-2 Current-voltage characteristics of a Langmuir probe in the LMM.

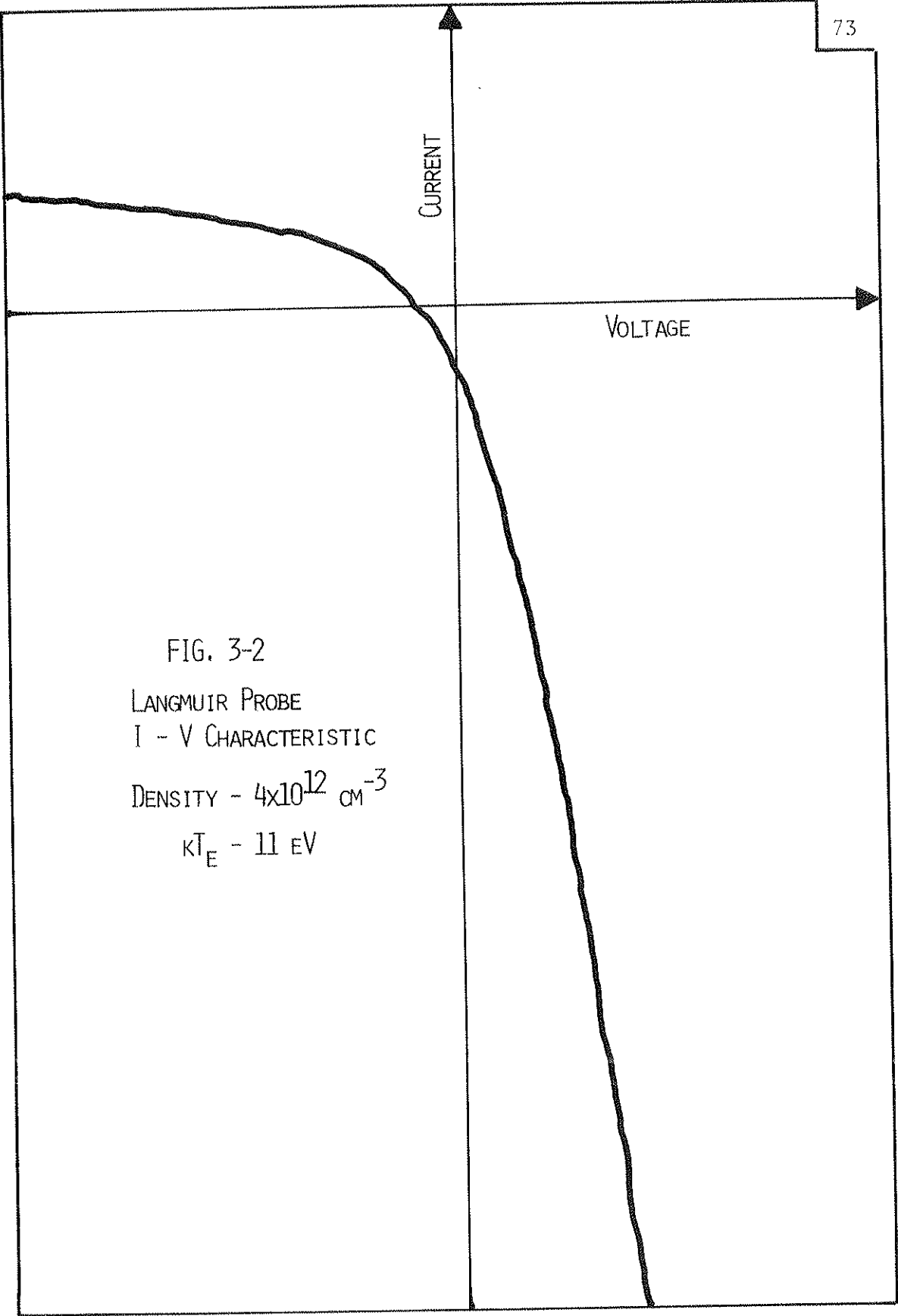
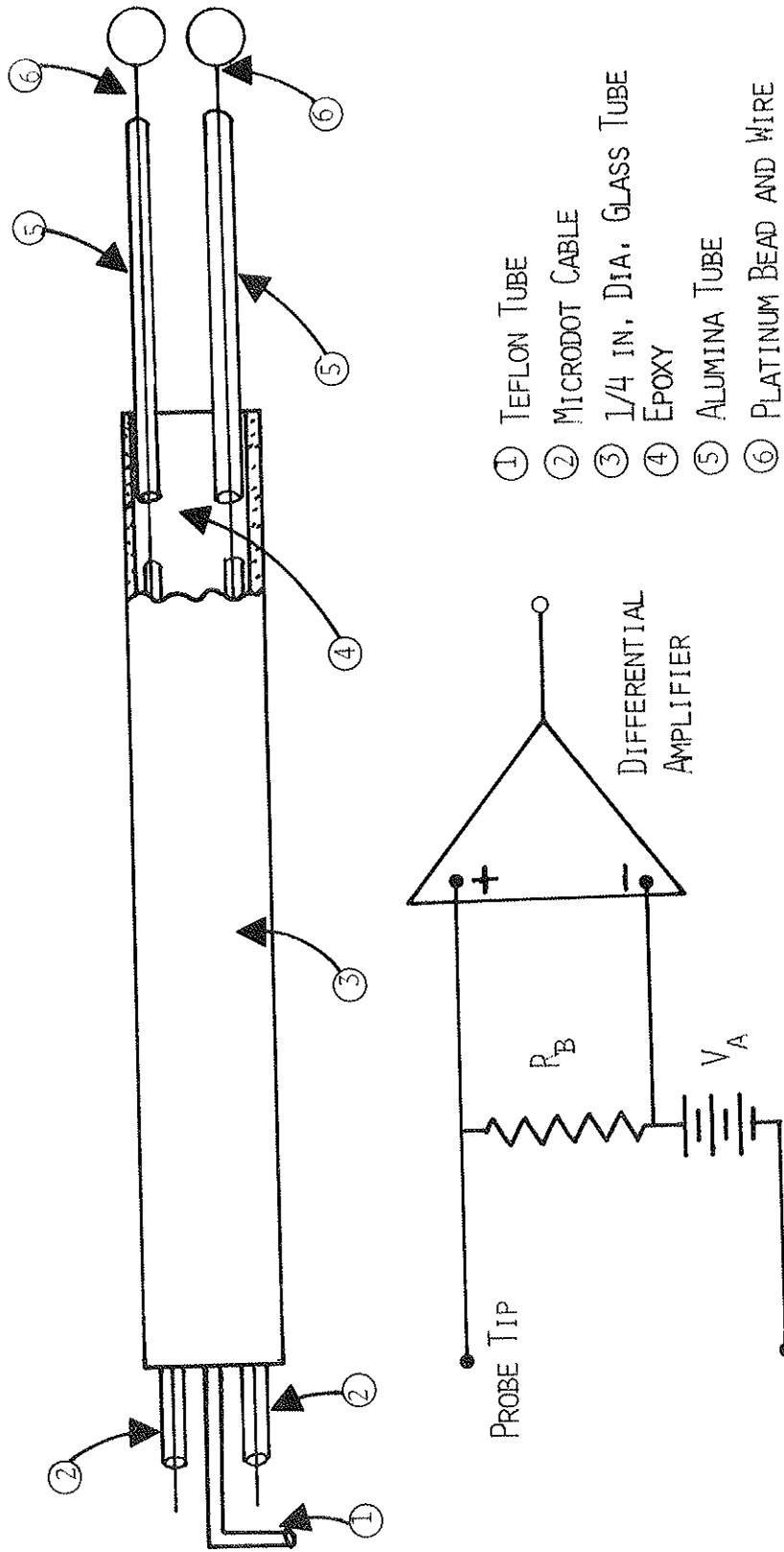


FIG. 3-2
LANGMUIR PROBE
I - V CHARACTERISTIC
DENSITY - $4 \times 10^{12} \text{ cm}^{-3}$
 $kT_E - 11 \text{ eV}$

Figure 3-3 Construction of a floating double probe used in the LMM and the circuit used to measure the ion saturation current.

FIG. 3-3
FLOATING DOUBLE PROBE



No SCALE

connect the probe to the oscilloscope-- C_p is approximately 100 pf/meter for either RG58 A/U cable or microdot cable.)

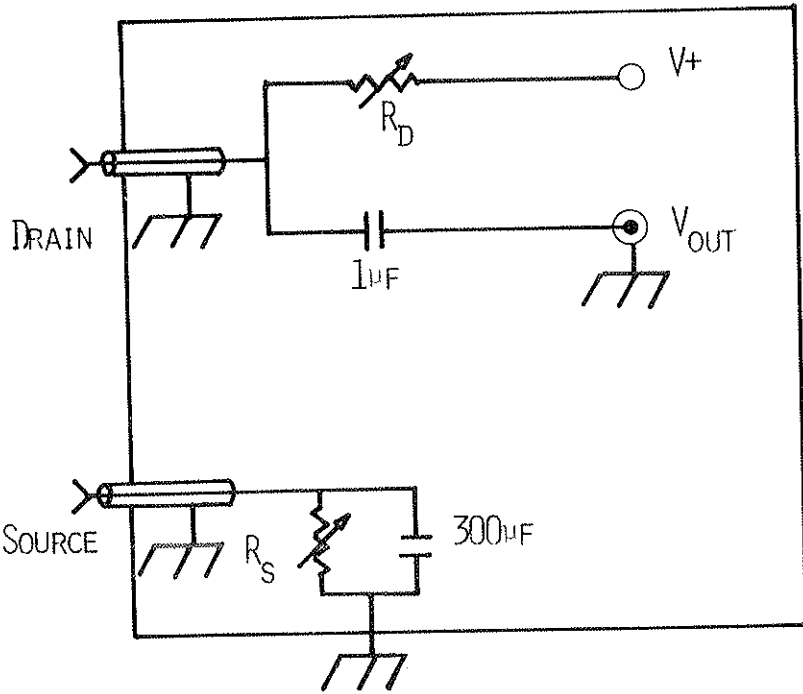
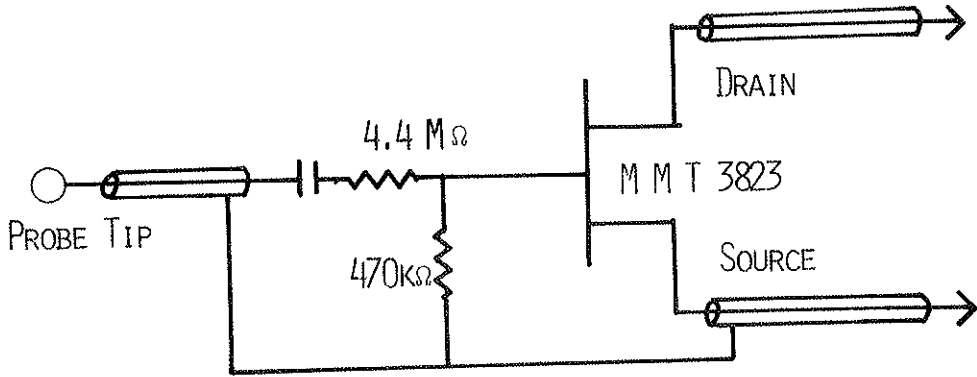
In contrast, measurements of the floating potential of the plasma require that the measuring circuit present as large an impedance as possible to the plasma so that a minimal current is drawn. This is accomplished in the LMM by attaching the probe directly to a voltage sensitive detector with an input impedance greater than the plasma sheath resistance. The magnitude of the sheath resistance is given by the relationship $R_s = (kT_e/e)(1/I_{oi})$.² For the temperature and density of the plasma in the LMM, $R_s \approx 30 \text{ k}\Omega$ so that the floating potential may be measured by using an oscilloscope or a DC Null meter which has an input impedance $\geq 1 \text{ M}\Omega$.

Measurement of the floating potential oscillations is more difficult since parasitic capacitance in the coaxial cables lowers the AC input impedance of the measuring circuit. To overcome this problem a special probe was constructed which has an FET amplifier built into the probe (Fig. 3-4). This probe has a very high input impedance, but is restricted to measuring the AC floating potential.

Finally, striped collectors like those used by Cavallo³ have been used to measure the particle flux to the walls of the LMM. The biasing circuit used is similar to that of a double probe. However, a high degree of isolation is desired so a circuit employing optical isolators was constructed to bias the collectors and measure the collected current (Fig. 3-5). A typical I-V characteristic of this system is

Figure 3-4 Schematic of the circuit used to measure the fluctuations in the floating potential. The top half of the circuit is built into the probe tip. The bottom half is external to the probe.

FIG. 3-4
CIRCUIT FOR FET PROBE

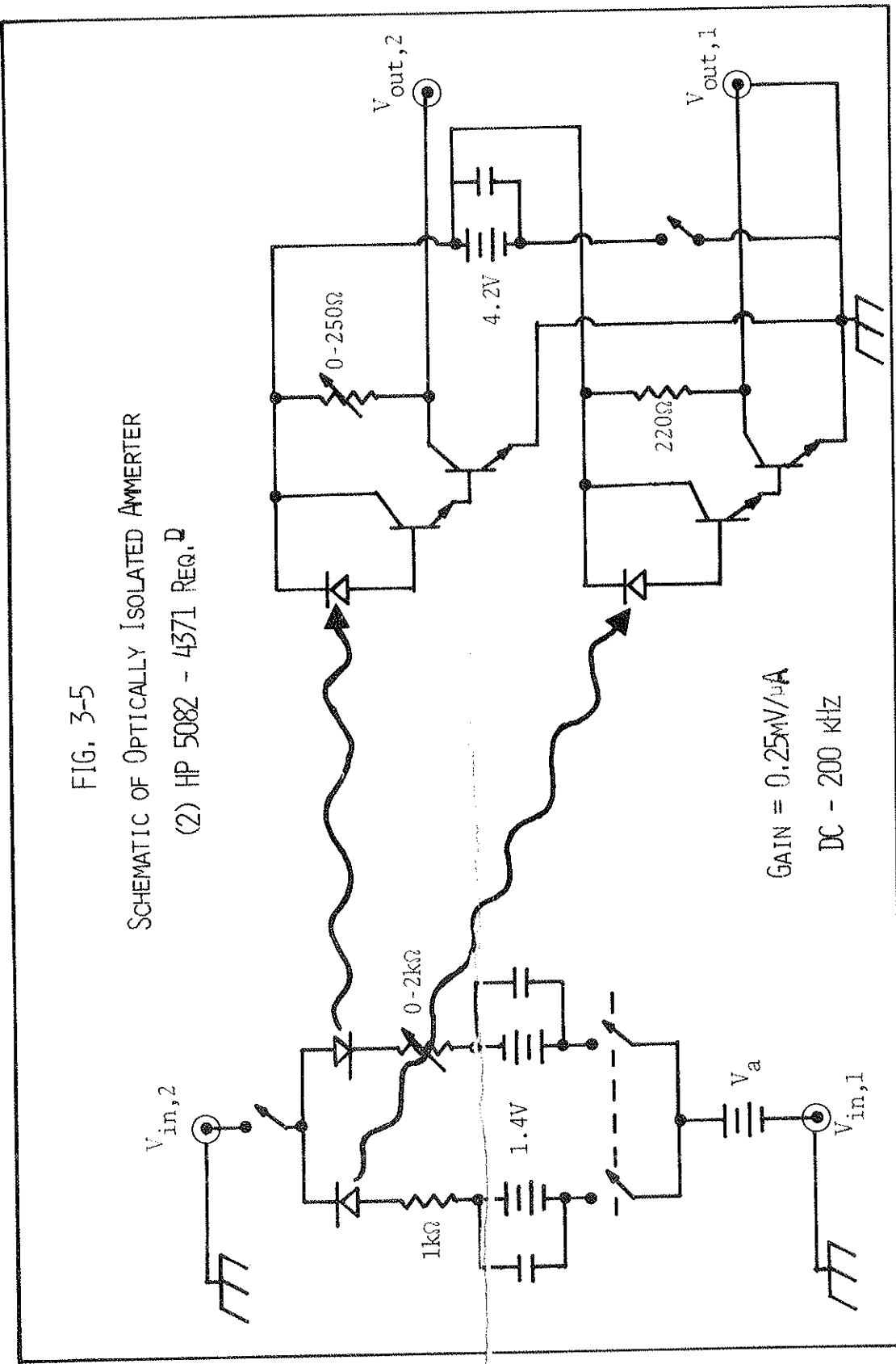


- $R_S = 1.3\text{k}\Omega$
- $R_D = 4.1\text{k}\Omega$
- $V+ = 18.5\text{V}$

Figure 3-5 Schematic of an optically isolated ammeter. This circuit is used for measurements with striped collectors and double probes when a high degree of isolation between the plasma and the external measuring circuit is desired. The output signal is read by taking a difference between the signals $V_{out,1}$ and $V_{out,2}$ on a differential amplifier.

This circuit is an adaption of an optically isolated ammeter designed by C. Armentrout [see C. Armentrout, Ph.D Dissertation, the University of Wisconsin, Madison, Wisconsin (1977)].

FIG. 3-5
SCHEMATIC OF OPTICALLY ISOLATED AMMETER
(2) HP 5082 - 4371 REQ. D



shown in Fig. 3-6.

I have only touched on the complexities involved in the construction and use of Langmuir probes. Extensive consideration of these problems is reported in Ref. 4-6. Practical considerations for the use of probes were presented by Sprott in Ref. 2.

The signals from the probes in the LMM are analysed using a number of electronic measuring devices. Among them are oscilloscopes, differential amplifiers, a frequency spectrum analyser, DC Null meters, RMS voltmeters, an X-Y recorder, and a Lock-In amplifier.

Techniques

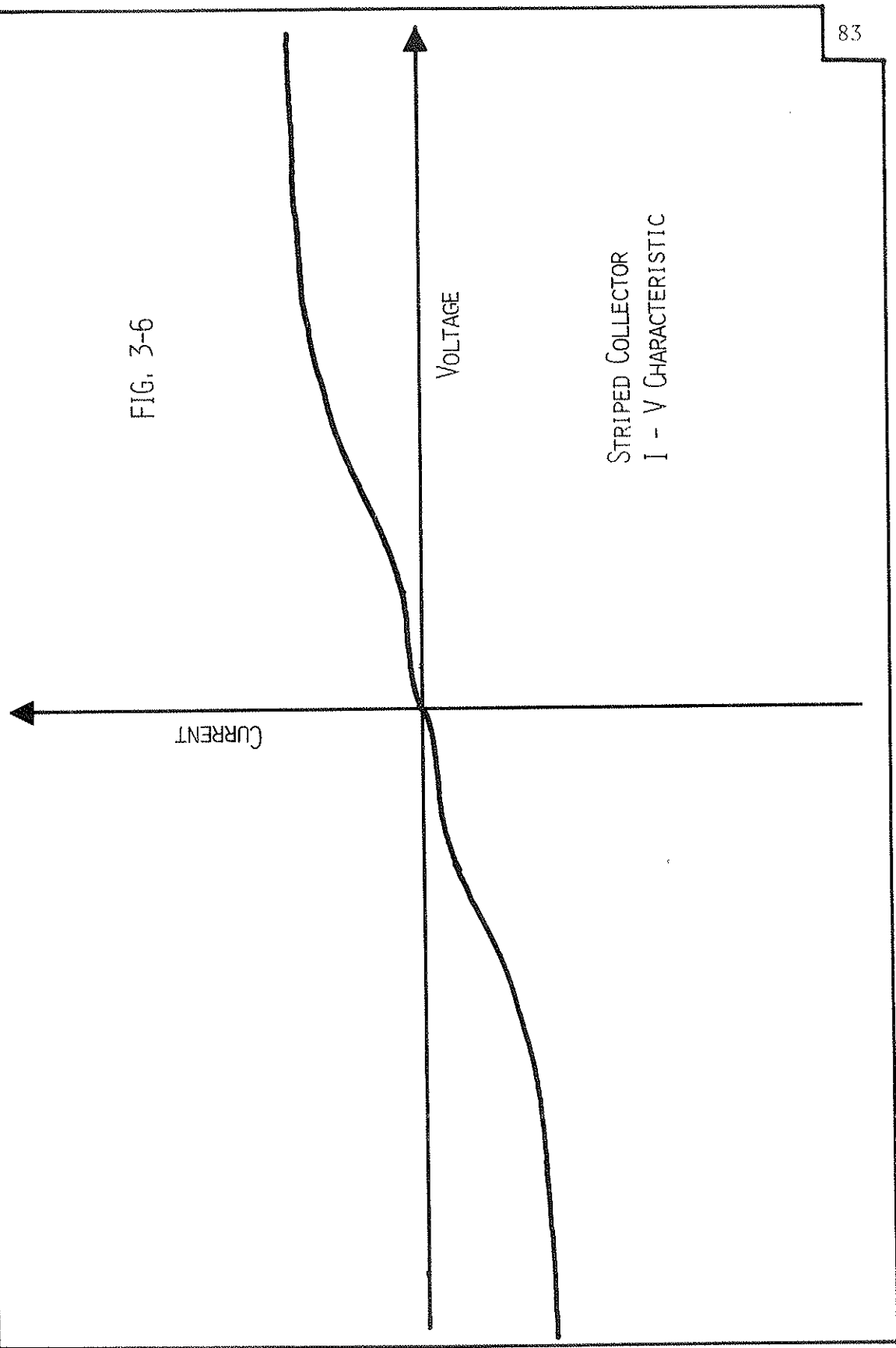
Two diagnostic techniques have been developed for the study of the instabilities in the LMM: transfer function analysis and feedback stabilization. The former is used to determine the presence and degree of damping of marginally stable modes; the latter is used to damp an unstable mode so that the growth rate can be measured and the effect of the instability on the equilibrium plasma can be determined. Both techniques can be used to determine whether an instability is reactive or dissipative.⁷

1) Transfer Function Analysis

In a recent paper, Richards and Emmert⁸ discussed the diagnostic utility of transfer function analysis⁹ for the identification of plasma modes and the measurement of damping rates. They illustrated this technique in an experiment using a reactive instability, the inter-

Figure 3-6 Current-voltage characteristics of a striped collector mounted inside of a corrector coil.

FIG. 3-6



STRIPED COLLECTOR
I - V CHARACTERISTIC

change instability in a magnetic mirror plasma. We have obtained similar results for both a reactive mode and a dissipative mode in the LMM. This complements the previous work since it gives an experimental confirmation of the transfer function analysis formalism for both dissipative and reactive modes.

As a function of the mirror ratio and neutral gas pressure an $m=1$ interchange mode, which is of the reactive class, and an $m=1$ dissipative drift mode can be made separately unstable or damped. The experiments consisted of "tuning" the plasma until the desired mode was weakly damped and the other mode was strongly damped. A sinusoidal voltage from an oscillator was then applied to the plasma. The output voltage and phase relative to the input signal were measured with a lock-in amplifier as the input frequency, ω , was varied.

The input elements consisted of two stainless steel grids in the plasma as shown in Fig. 3-7. They were biased oppositely to produce an odd- m signal in the plasma. The output element was a single Langmuir probe biased to measure the ion saturation current. This probe, also shown in Fig. 3-7, was at the same axial position as the grids. The system was checked to insure that there was no direct capacitive coupling between the input and output elements, and that at a given frequency, ω , the output signal responded linearly as the input voltage was varied. The system is shown schematically in Fig. 3-8.

Before considering the experimental results, we first review some of the theoretical predictions of transfer functions. We assume azi-

Figure 3-7 Arrangement of the launching and receiving probes for transfer function analysis. The probes were mounted in the port flange (see Fig. 2-3).

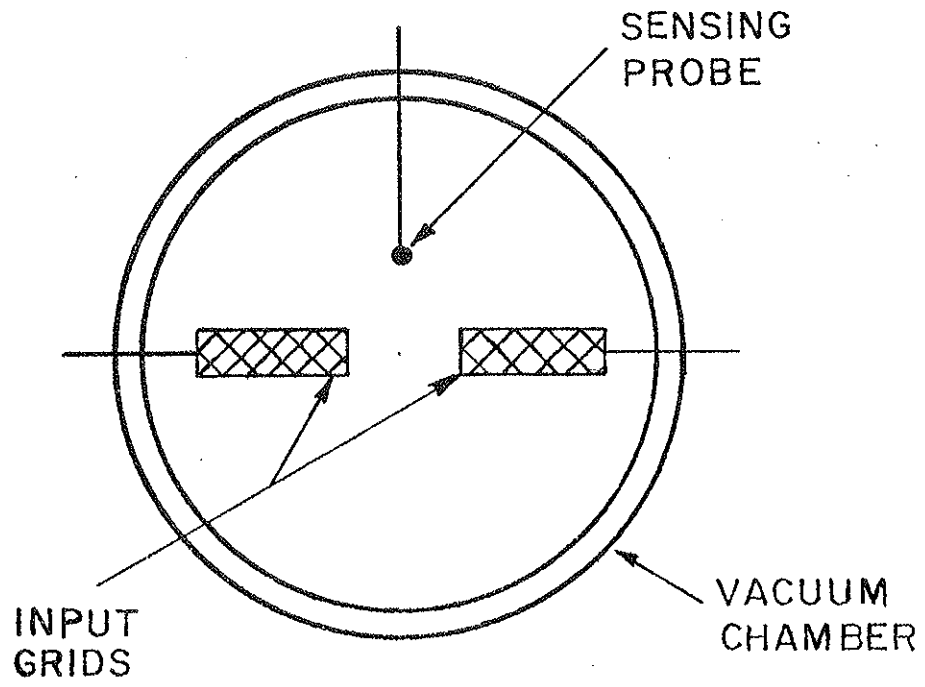


FIG. 3-7

Figure 3-8 Schematic representation of the circuit used for transfer function analysis.

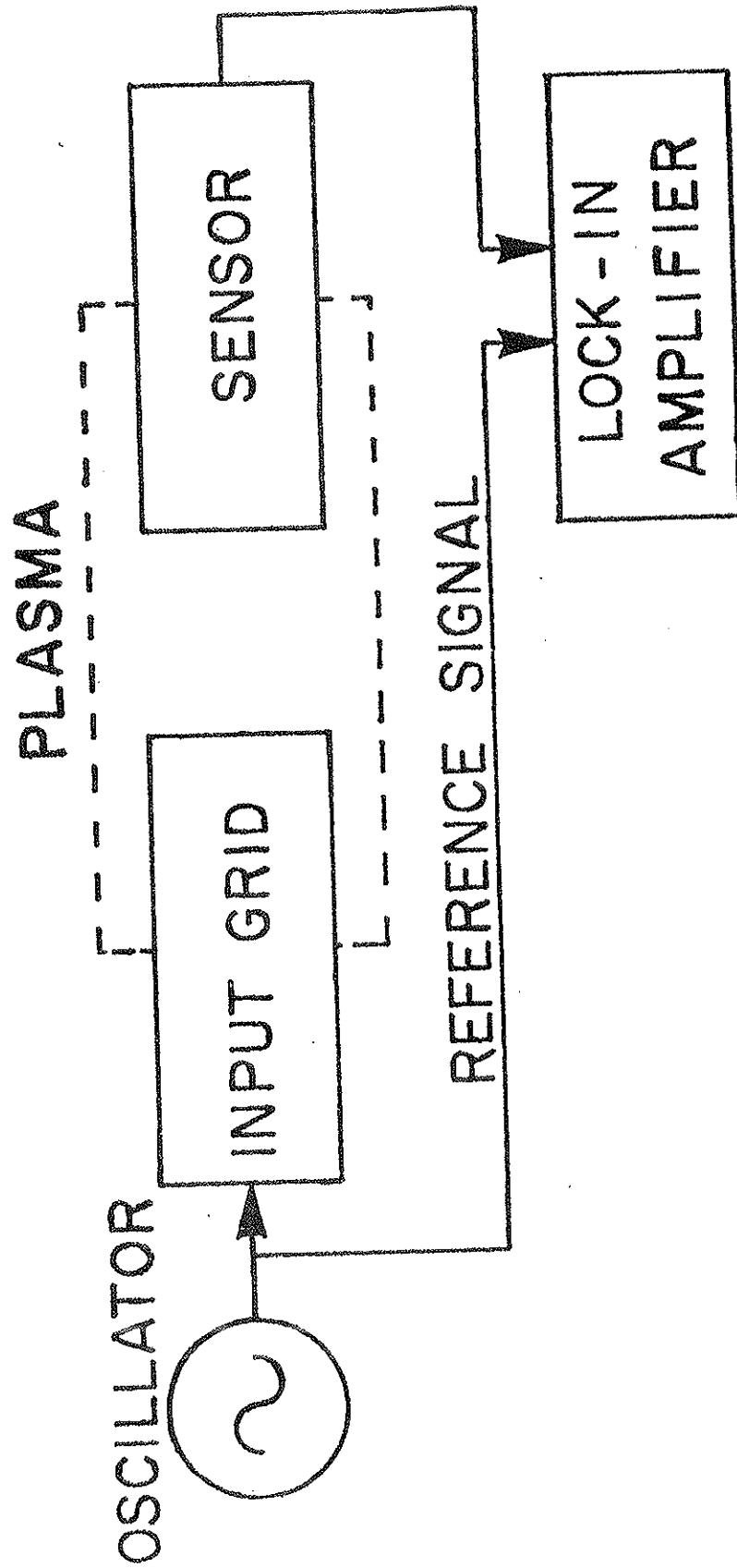


FIG. 3-8

muthal symmetry of the background plasma and Fourier transform the spatially dependent quantities in the azimuthal angle θ (i.e., $\sim \exp(im\theta)$). The transfer function is defined as the ratio of the Fourier transform (in time) of the output signal to that of the input signal. As derived in Ref. 8, it can be written as

$$T(\omega, m) = \frac{A_m}{\omega^2} \left[\frac{1}{\epsilon(\omega, m)} - \frac{1}{\epsilon(\omega, -m)} \right] \quad (3.1)$$

where $m > 0$. The dielectric function of the plasma is $\epsilon(\omega, m)$ and A_m is a collection of various constants of no particular concern. The two terms $\epsilon^{-1}(\omega, m)$ and $\epsilon^{-1}(\omega, -m)$ describe the plasma's response to signals traveling in the (+) or (-) θ direction, respectively. In the case of a weakly damped mode, either the term $\epsilon(\omega, m)$ or $\epsilon(\omega, -m)$ will be small for ω near ω_0 , the mode frequency.

We can define, by choice of coordinate system, the direction of θ such that $\epsilon(\omega, m) \approx 0$. Then $T(\omega, m)$ can be approximated by

$$T(\omega, m) = \frac{A_m}{\omega^2} \frac{1}{\epsilon(\omega, m)}. \quad (3.2)$$

To proceed further we must choose either dissipative or reactive modes. For a dissipative mode we expand both the real and imaginary parts of the dielectric function in a Taylor series expansion

$$\begin{aligned} \epsilon_R(\omega, m) &= \epsilon_R(\omega_0, m) + \frac{\partial}{\partial \omega} \epsilon_R(\omega_0, m) (\omega - \omega_0) + \dots \\ \epsilon_I(\omega, m) &\approx \epsilon_I(\omega_0, m) \end{aligned} \quad (3.3)$$

where ω_0 is defined by $\epsilon_R(\omega_0, m) = 0$. Using these expressions we can

rewrite the transfer function in the form

$$T(\omega, m) = \frac{A_m / \omega^2}{(\omega - \omega_o) + i\gamma_o} \quad (3.4)$$

where γ_o is the damping rate. The amplitude and phase of $T(\omega, m)$ are given by

$$|T(\omega, m)| = \frac{|A_m| / \omega^2}{\sqrt{(\omega - \omega_o)^2 + \gamma_o^2}} \quad (3.5)$$

$$\tan(\phi + \phi_o) = \frac{\gamma_o}{\omega - \omega_o} \quad (3.6)$$

where ϕ_o is the phase of A_m . Analysis of Eqs. (3.5) and (3.6) shows (1) in the vicinity of the instability frequency, ω_o , there is a rapid increase in the amplitude $|T|$ and a rapid change in phase θ , (2) the total change in the phase asymptotically approaches 180° as the frequency is swept by ω_o , (3) the phase change across the -3db points of the amplitude versus frequency plot is 90° , (4) the damping rate can be determined from the amplitude vs. frequency plot according to

$$\gamma_o = \frac{|\Delta\omega|}{\sqrt{3}} \Big|_{1/2 \text{ MAX}} \quad (3.7)$$

where $|\Delta\omega| \Big|_{1/2 \text{ MAX}}$ is the frequency half-width at half maximum, (5) the damping rate can also be determined from the phase vs. frequency plot according to

$$\gamma_o = - \frac{d\omega}{d\phi} \Big|_{\omega = \omega_o} \quad (3.8)$$

A similar Taylor series expansion may be made for a reactive mode⁸. Using this expansion the transfer function can be written in the form

$$T(\omega, m) = \frac{A_m / \omega^2}{(\omega - \omega_0)^2 + 2iB(\omega - \omega_0) + \gamma_0^2 + 2B\gamma_0} \quad (3.9)$$

where ω_0 is the instability frequency, γ_0 is the damping rate, and B is the dissipation constant. The amplitude and phase of T are given by

$$|T(\omega, m)| = \frac{A_m / \omega^2}{\{[(\omega - \omega_0)^2 + \gamma_0^2 + 2B\gamma_0]^2 + 4B^2(\omega - \omega_0)^2\}^{1/2}} \quad (3.10)$$

$$\tan(\phi + \phi_0) = \frac{2B(\omega - \omega_0)}{(\omega - \omega_0)^2 + \gamma_0^2 + 2B\gamma_0} \quad (3.11)$$

where ϕ_0 is the phase of A_m . The amplitude, $|T|$, can exhibit either one or two peaks, depending on the dissipative coefficient B and γ_0 . The phase changes rapidly for $\omega \approx \omega_0$ as the frequency is swept and the total change in phase is 360° , asymptotically. The phase change across the -3 db points of the amplitude plot is 130° for $\gamma_0 = B$. In order to determine γ_0 and B, a least squares fit of the amplitude and/or phase versus frequency to the data should be made.

The measured transfer function of the dissipative drift wave is shown in Fig. 3-9. For frequencies near 17 kHz, there is a rapid increase in the output amplitude. (This is also the frequency observed when the mode is barely unstable.) For these same frequencies there is a rapid change in phase; the total phase change is approximately 180° , and the phase drops by 90° across the -3 db points of the amplitude

Figure 3-9 Transfer function response (amplitude and phase) of a plasma which was marginally stable to a dissipative drift wave.

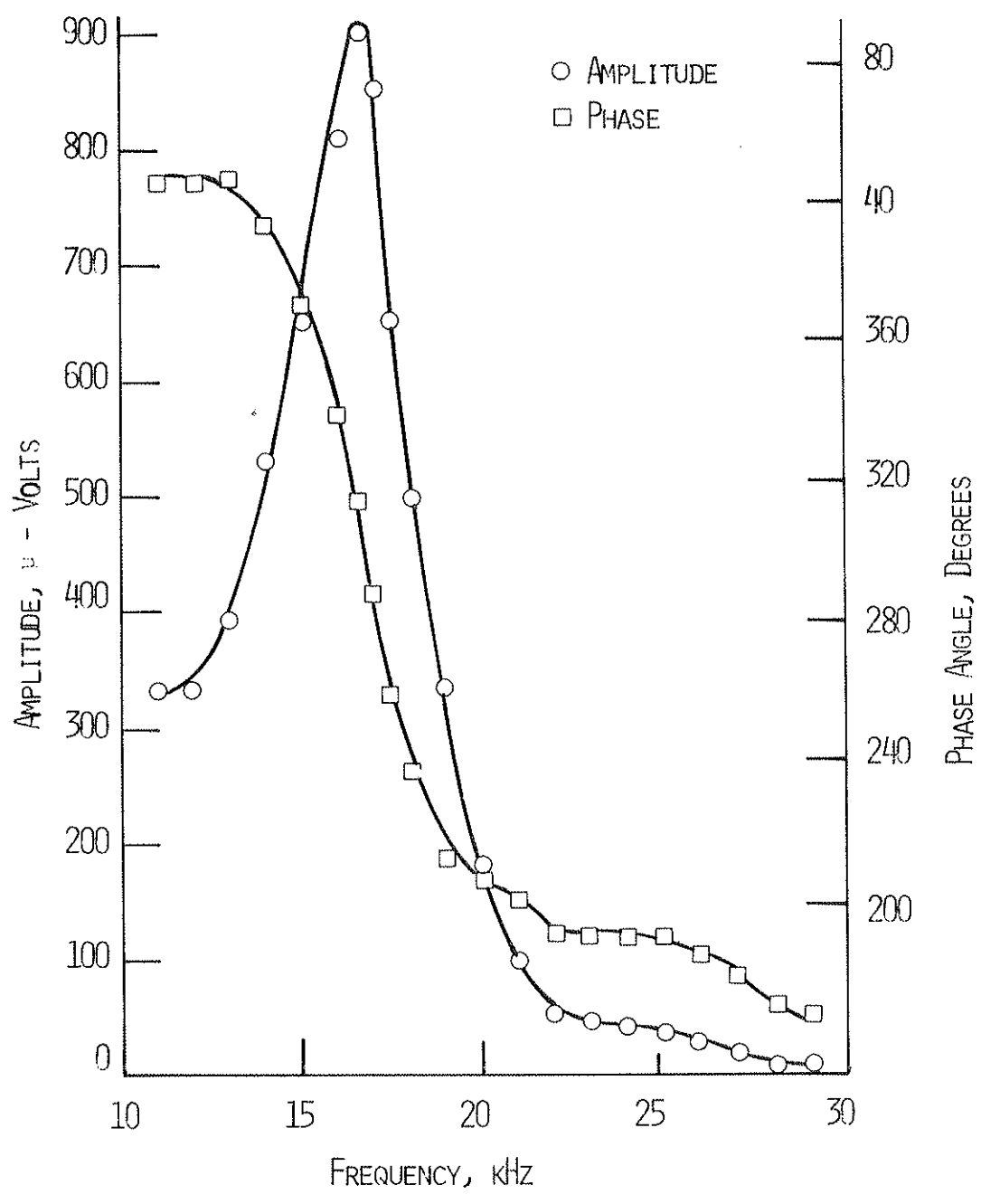


FIG. 3-9

plot. Calculating the damping rate, γ_0 , from both the amplitude and phase graphs yields a consistent value of $9.5 \times 10^3 \text{ sec}^{-1}$.

The corresponding results for the reactive type interchange instability are shown in Fig. 3-10. As in the case of the drift wave, there is a rapid increase in the output amplitude for frequencies around the last noted instability frequency, in this case, $f_0 = 3.2$ kHz; and there is a rapid change in phase. The phase change across the -3 dB points of the amplitude plot is 130° which is consistent with our prediction of the response of a reactive mode. Also shown in Fig. 3-10 are the theoretical amplitude and phase of $T(\omega, m)$ from Eqs. (3.10) and (3.11), where the parameters B , γ_0 , ω_0 are obtained by fitting the theoretical curves to the data. The values obtained in this way are $\omega_0 = 2.0 \times 10^4 \text{ sec}^{-1}$, $B = 7.0 \times 10^2 \text{ sec}^{-1}$, and $\gamma_0 = 6.8 \times 10^2 \text{ sec}^{-1}$.

Fig. 3-10 also illustrates a zero of the transfer function at $f \approx 3.7$ kHz. In the vicinity of a zero, one cannot neglect $1/\epsilon(\omega, -m)$ compared with $1/\epsilon(\omega, m)$, and must consider all the terms in the sum over m . The zero observed in Fig. 3-10 is apparently a root of the full transfer function

$$T(\omega) = \sum_m \frac{A_m}{\omega^2} \left[\frac{1}{\epsilon(\omega, m)} - \frac{1}{\epsilon(\omega, -m)} \right],$$

where the coupling of the input elements to the various m -numbers is contained in the A_m term. We have tried several theoretical models to explain the location of the zero shown in Fig. 3-10. So far, we have

Figure 3-10 Transfer function response (amplitude and phase) of a plasma which was marginally stable to a reactive type instability - an interchange instability. A zero in the transfer function was observed at 3.7 kHz.

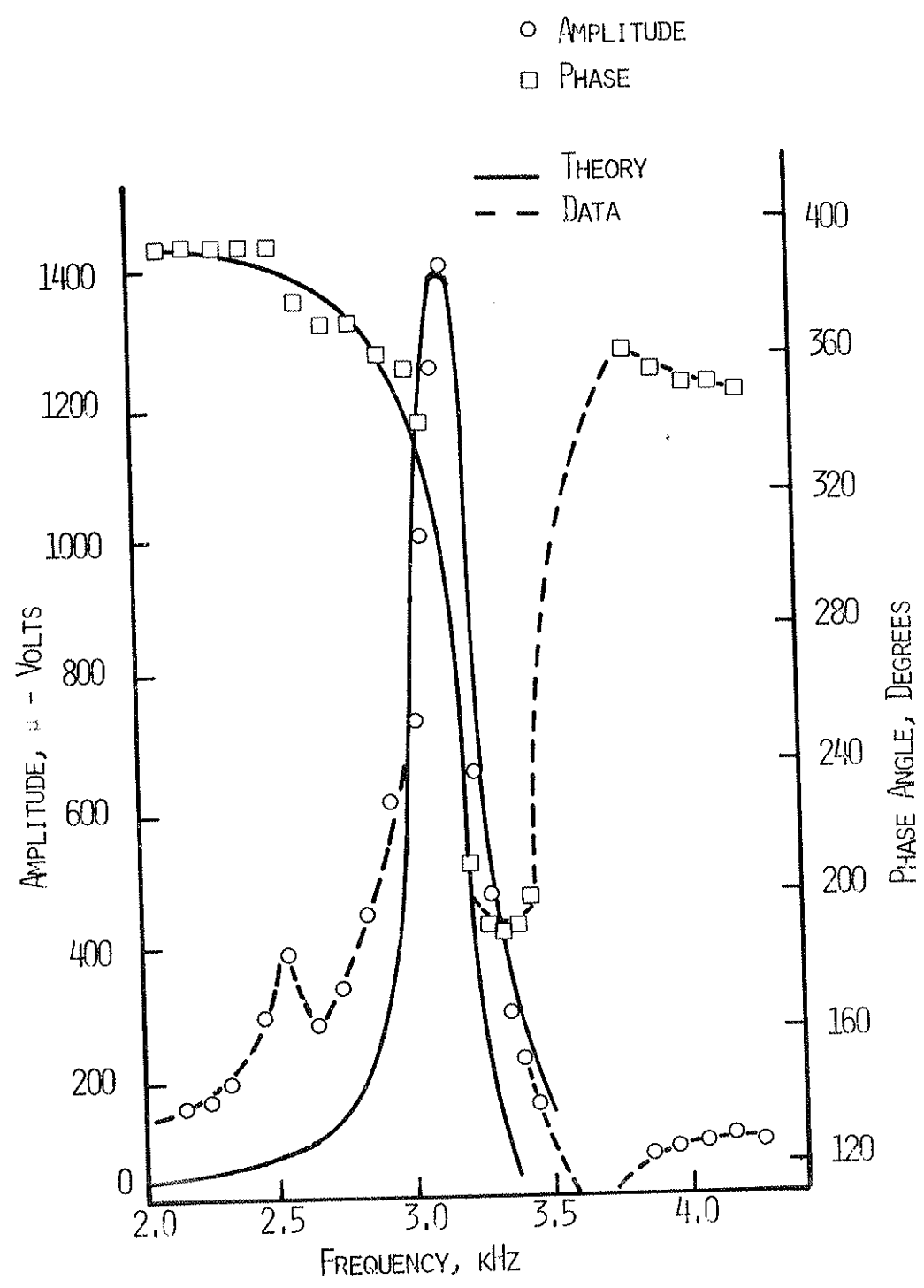


FIG. 3-10

been unable to do so.

2) Feedback Stabilization

A feedback stabilization system can be a very powerful diagnostic tool for the study of a plasma in the presence of instabilities. Among its uses are the following: 1) it can be used to suppress an instability so that the plasma properties can be studied without the perturbing effects of the instability; 2) it can be used to control the instability amplitude so the effect that the instability has on the plasma can be better understood (e.g. measurements of the cross field losses versus $\delta n/n$ can be made); 3) when gated on and off the feedback system allows the instability to be studied in the linear regime and during its approach to nonlinear saturation (e.g. nonlinear frequency shifts at saturation can be measured); 4) mode identification is simplified when feedback can be used to determine whether a mode is reactive or dissipative; 5) it is one of the few ways that the growth rate of an instability can be measured; and 6) using feedback, marginally stable or weakly damped modes ($\gamma_0 \lesssim 0$) in the plasma can be excited and identified. For these reasons a feedback stabilization system was developed for the LMM experiment.

The effect of feedback stabilization on a reactive instability has been studied in detail by R. K. Richards.¹⁰ We will make use of his work later in this paper. We now turn our attention to the analysis of the effect of feedback on a dissipative instability. The following analysis is modeled so as to be particularly applicable to the

where C is composed of two parts: C_o is the capacitance without the plasma and C_p is the additional capacitance added by the presence of the plasma. We assume here that C_p is small so that

$$C \approx C_o . \quad (3.23)$$

Using Eqs. (3.21), (3.22), and (3.23), Eq. (3.20) reduces to

$$\epsilon_o \int \nabla\phi^* \cdot \overleftrightarrow{K} \cdot \nabla\phi \, dv = - \frac{C_o}{A} \int \phi^* v_f \, ds . \quad (3.24)$$

The dielectric tensor \overleftrightarrow{K} is now divided into its Hermitian, \overleftrightarrow{K}_H , and anti-Hermitian, \overleftrightarrow{K}_A , parts and a Taylor series expansion in ω will be made for each part,

$$\overleftrightarrow{K} \approx \overleftrightarrow{K}_H(\omega_o) + \left. \frac{\partial \overleftrightarrow{K}_H}{\partial \omega} \right|_{\omega_o} (\omega - \omega_o) + \overleftrightarrow{K}_A(\omega_o) + \dots \quad (3.25)$$

For a dissipative instability near marginal stability

$$\int \nabla\phi^* \cdot \overleftrightarrow{K}_H(\omega_o) \cdot \nabla\phi \, dV = 0, \quad (3.26)$$

(which defines ω_o) so that when we insert Eq. (3.25) into Eq. (3.24) we obtain

$$\begin{aligned} \epsilon_o (\omega - \omega_o) \int \nabla\phi^* \cdot \left. \frac{\partial \overleftrightarrow{K}_H}{\partial \omega} \right|_{\omega_o} \cdot \nabla\phi \, dV + \epsilon_o \int \nabla\phi^* \cdot \overleftrightarrow{K}_A \cdot \nabla\phi \, dV = \\ - \frac{C_o}{A} \int \phi^* v_f \, ds . \end{aligned} \quad (3.27)$$

If we now divide Eq. (3.27) through by

$$\epsilon_0 \int \nabla\phi^* \cdot \frac{\overleftrightarrow{\partial\mathbf{K}}_H}{\partial\omega} \Big|_{\omega_0} \cdot \nabla\phi \, dV ,$$

we obtain an equation in ω of the form

$$(\omega - \omega_0) + ib = g(\omega)\hat{K} , \quad (3.28)$$

where

$$ib = \frac{\int \nabla\phi^* \cdot \overleftrightarrow{\mathbf{K}}_A \cdot \nabla\phi \, dV}{\int \nabla\phi^* \cdot \frac{\overleftrightarrow{\mathbf{K}}_H}{\partial\omega} \Big|_{\omega_0} \cdot \nabla\phi \, dV} ,$$

$$g(\omega)\hat{K} = \frac{-\frac{c}{A} \int \phi^* \nabla_f \, ds}{\int \nabla\phi^* \cdot \frac{\overleftrightarrow{\mathbf{K}}_H}{\partial\omega} \Big|_{\omega_0} \cdot \nabla\phi \, dV} .$$

Note that the Hermitian part of K gives real values for the scalar product,

$$\int \nabla\phi^* \cdot \frac{\overleftrightarrow{\mathbf{K}}_H}{\partial\omega} \Big|_{\omega_0} \cdot \nabla\phi \, dV ,$$

and the antiHermitian part gives imaginary values, so the constant b is real; the term $g(\omega)\hat{K}$ will be considered complex since it will be due to an unspecified feedback potential. $g(\omega)$ contains the phase shift and gain of the feedback loop.

Evaluation of the constant b is accomplished by considering the plasma in the absence of feedback ($g(\omega)\hat{K} = 0$). This gives

$$(\omega - \omega_0) + ib = 0 . \quad (3.29)$$

We require that the frequency, ω , be given by

$$\omega = \omega_0 + i\gamma_0$$

in the absence of feedback, where ω_0 is defined in Eq. (3.26). Substituting this into Eq. (3.29) yields

$$i\gamma_0 + ib = 0, \quad (3.30)$$

or

$$b = -\gamma_0 .$$

Substituting this value into Eq. (3.28) and letting

$$g(\omega)\hat{K} = A(\omega)e^{i\phi(\omega)} ,$$

we arrive at the desired relationship

$$(\omega - \omega_0) - i\gamma_0 = A(\omega)e^{i\phi(\omega)} . \quad (3.31)$$

Here we have allowed the feedback gain $A(\omega)$, and the feedback phase shift, $\phi(\omega)$, to be functions of the frequency, ω , since this is the case generally encountered in feedback experiments. By considering different forms for the frequency dependencies in $A(\omega)$ and $\phi(\omega)$ it is possible to determine from Eq. (3.31) the magnitude of the effect of these frequency dependencies on the effectiveness of the feedback circuit and to determine whether frequency compensation will be necessary.

As an example of the technique employed to study the effects of frequency dependence on a feedback circuit we will consider two cases.

Case I. No frequency dependence.

$$A(\omega) = A_o ,$$

$$\phi(\omega) = \phi_o .$$

For this case Eq. (3.31) becomes

$$(\omega - \omega_o) - i\gamma_o = A_o e^{i\phi_o} , \quad (3.32)$$

or

$$(\omega - \omega_o) - i\gamma_o - A_o \cos\phi_o - iA_o \sin\phi_o = 0 . \quad (3.33)$$

Using $\omega = \omega_r + i\gamma$ the imaginary part of Eq. (3.33) is

$$\gamma - \gamma_o - A \sin \phi_o = 0 . \quad (3.34)$$

For stability ($\gamma \leq 0$). Then

$$-A \sin \phi_o \geq \gamma_o . \quad (3.35)$$

Examining Eq. (3.35) we note the following: There is a minimum gain required for stabilization, $A > \gamma_o$; with sufficient gain, stabilization can be achieved over a phase range of 180° ($-\pi \leq \phi_o \leq 0$); and there is no maximum gain above which the feedback signal is destabilizing.

Case II. The gain has a $\frac{1}{\omega}$ dependence.

$$A = A_o \frac{\omega_o}{\omega}$$

$$\phi = \phi_o .$$

Eq. (3.31) now becomes

$$(\omega - \omega_0) - i\gamma_0 = A_0 \frac{\omega}{\omega_0} e^{i\phi_0} . \quad (3.36)$$

The right hand side of Eq. (3.36) is expanded in a Taylor series about ω_0 yielding

$$(\omega - \omega_0) - i\gamma_0 = A_0 e^{i\phi_0} \left[1 - \frac{\omega - \omega_0}{\omega_0} \right] . \quad (3.37)$$

Rearranging and expanding, Eq. (3.37) becomes

$$\begin{aligned} (\omega_r - \omega_0) + i\gamma \left(1 + \frac{2A_0}{\omega_0} \cos \phi_0 + \frac{A_0^2}{\omega_0^2} \right) = \\ A_0 \cos \phi_0 + \frac{\gamma_0}{\omega_0} A_0 \sin \phi_0 + \frac{A_0^2}{\omega_0^2} + \\ i\gamma_0 + iA_0 \sin \phi_0 + i\gamma_0 \frac{A_0}{\omega_0} \cos \phi_0 , \end{aligned} \quad (3.38)$$

using $\omega = \omega_r + i\gamma$. Equating the imaginary parts of Eq. (3.38) gives

$$\begin{aligned} \gamma \left(1 + \frac{2A_0}{\omega_0} \cos \phi_0 + \frac{A_0^2}{\omega_0^2} \right) = \\ \gamma_0 + A_0 \sin \phi_0 + \gamma_0 \frac{A_0}{\omega_0} \cos \phi_0 . \end{aligned} \quad (3.39)$$

The line of marginal stability ($\gamma = 0$) is, therefore, defined by

$$A_0 \sin \phi_0 + \frac{\gamma_0 A_0}{\omega_0} \cos \phi_0 = -\gamma_0 \quad (3.40)$$

for $\gamma_0/\omega_0 \ll 1$. This reduces to

$$A_0 \sin \phi_0 \approx -\gamma_0 , \quad (3.41)$$

which is the same result we obtained for Case I (no frequency dependence).

The effectiveness of feedback stabilization on a dissipative mode with $\gamma_o/\omega_o \ll 1$ is, therefore, only slightly affected by the ω^{-1} dependence in the gain. This is in contrast to the feedback stabilization of a reactive mode where a ω^{-1} dependence in the gain caused a significant reduction in the gain width.¹⁰

To see how such a ω^{-1} dependence can be generated in the feedback system consider the stabilization of an electrostatic instability in the linear machine. The ion density fluctuations caused by the instability are sensed by a Langmuir probe. The relationship between the ion density fluctuations and the potential for an electrostatic instability is given by¹²

$$\delta n_i = \frac{-iq}{\omega M_i \Omega_i} \frac{dn_o}{dx} E \left[1 + \frac{\omega}{\Omega_i} \frac{n_o}{\frac{dn_o}{dx}} k_\perp \right], \quad (3.42)$$

where δn_i is the ion density fluctuation, q is the ion charge, Ω_i is the ion cyclotron frequency, k_\perp is the perpendicular wave number, and E is the electric field,

$$E = -\nabla \phi_p, \quad (3.43)$$

where ϕ_p is the potential. For low frequency instabilities, $\omega/\Omega_i \ll 1$, Eq. (3.42) is of the form

$$\delta n_i \approx \frac{B}{\omega} \phi_p \quad (3.44)$$

where B is a function of the plasma parameters. So, in sensing δn_i , the probe has equivalently sensed $\frac{B}{\omega} \phi_p$. If this signal is then amplified (A_o/B), phase shifted ($e^{i\theta_o}$) and applied to the plasma in the form of a potential to suppress the instability, we note that a ω^{-1} dependence has been added to the gain;

$$\phi_{FB} = (A_o \omega^{-1} e^{i\theta_o}) \phi_p . \quad (3.45)$$

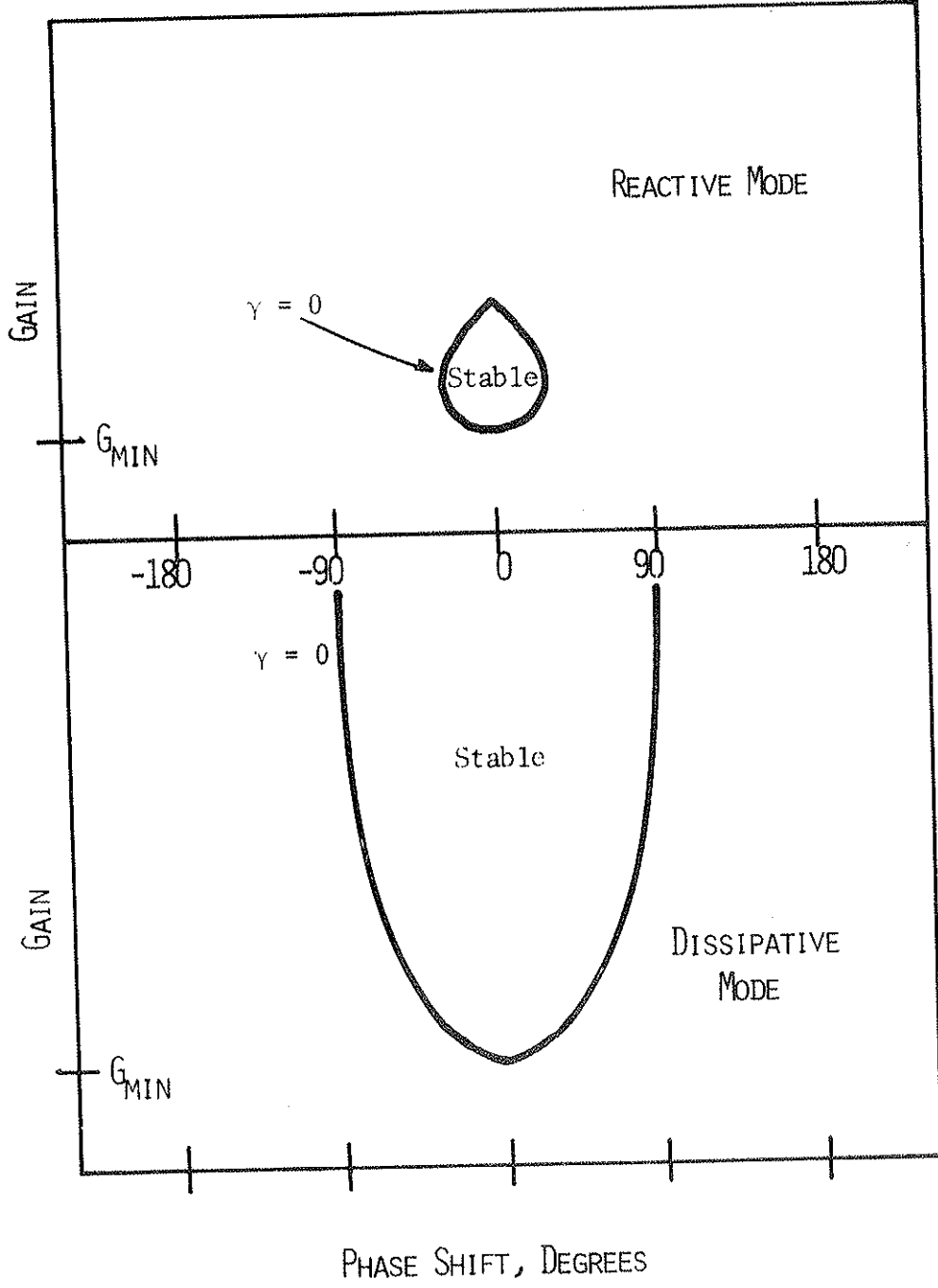
The major differences in the stabilization of reactive and dissipative instabilities can be discussed in terms of gain-phase plots (Fig. 3-11). Typically, the gain and phase widths over which significant suppression of a reactive mode may be achieved are small. The finite phase width is due to dissipative effects in the plasma (in the absence of these effects the phase width is zero).¹¹ The finite gain width is due to destabilizing frequency dependencies in the feedback circuit, i.e. if no frequency dependencies are present the gain width is infinite.

In contrast, the phase width for a dissipative mode approaches 180° , and while the gain width can be reduced by frequency dependencies in the feedback circuit, typically, it is a less severe problem.

As reported in Ref. 13, we obtained significant stabilization of both the interchange instability and the dissipative drift wave using feedback. Unfortunately, our efforts to stabilize the trapped electron instability have not met with this degree of success. To date, we have been plagued by two problems: nonlinear response to feedback and the

Figure 3-11 Stable regions of feedback gain-phase space
typical of reactive and dissipative instabilities.

FIG 3-11



appearance of new instabilities as the mode of interest is stabilized.

We have achieved significant stabilization of the trapped electron mode (Fig. 3-12). However, the response of the instability to changes in the phase shift introduced in the feedback loop was not in agreement with linear theory (Fig. 3-13). In a linear theory the frequency shift should be symmetric about f_0 according to $\Delta f = f_0 - A \cos \phi$ (Eq. 3.33), where f_0 is the instability frequency in the absence of feedback, A is the feedback gain, and ϕ is the phase shift. In Fig. 3-13 the frequency shift does appear to vary slightly as a function of the phase shift, but it varies about a frequency which is shifted by 7 kHz from f_0 . Such a response could be due to a change in the equilibrium plasma as the mode is stabilized. Indeed, such a change would be expected if the instability had saturated by changing the equilibrium plasma. However, it is also possible that the feedback system is modifying the equilibrium plasma and thereby stabilizing the trapped electron mode indirectly. In order to avoid this point of confusion we have tried a number of alternate arrangements and types of suppressing elements, but none have been as effective as the external foils.

The second problem, the appearance of new instabilities, is due to the fact that feedback can destabilize as well as stabilize. Destabilizing instabilities can occur due to either a direct or an indirect coupling between the feedback system and an instability. A weakly damped mode can be directly destabilized if sufficient feedback power is coupled into the mode with a phase shift which lies outside the

Figure 3-12 Feedback suppression of a trapped electron instability.

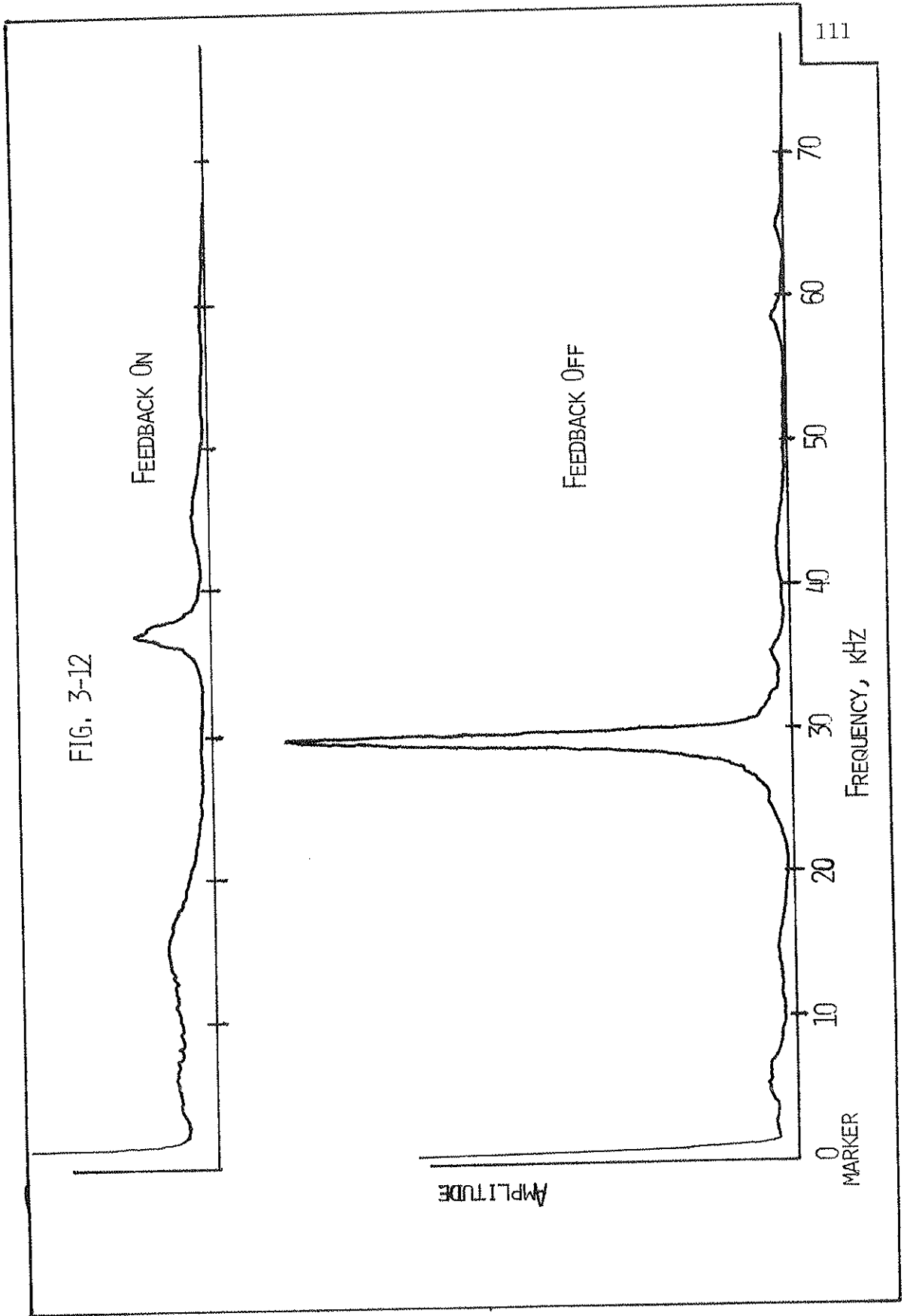
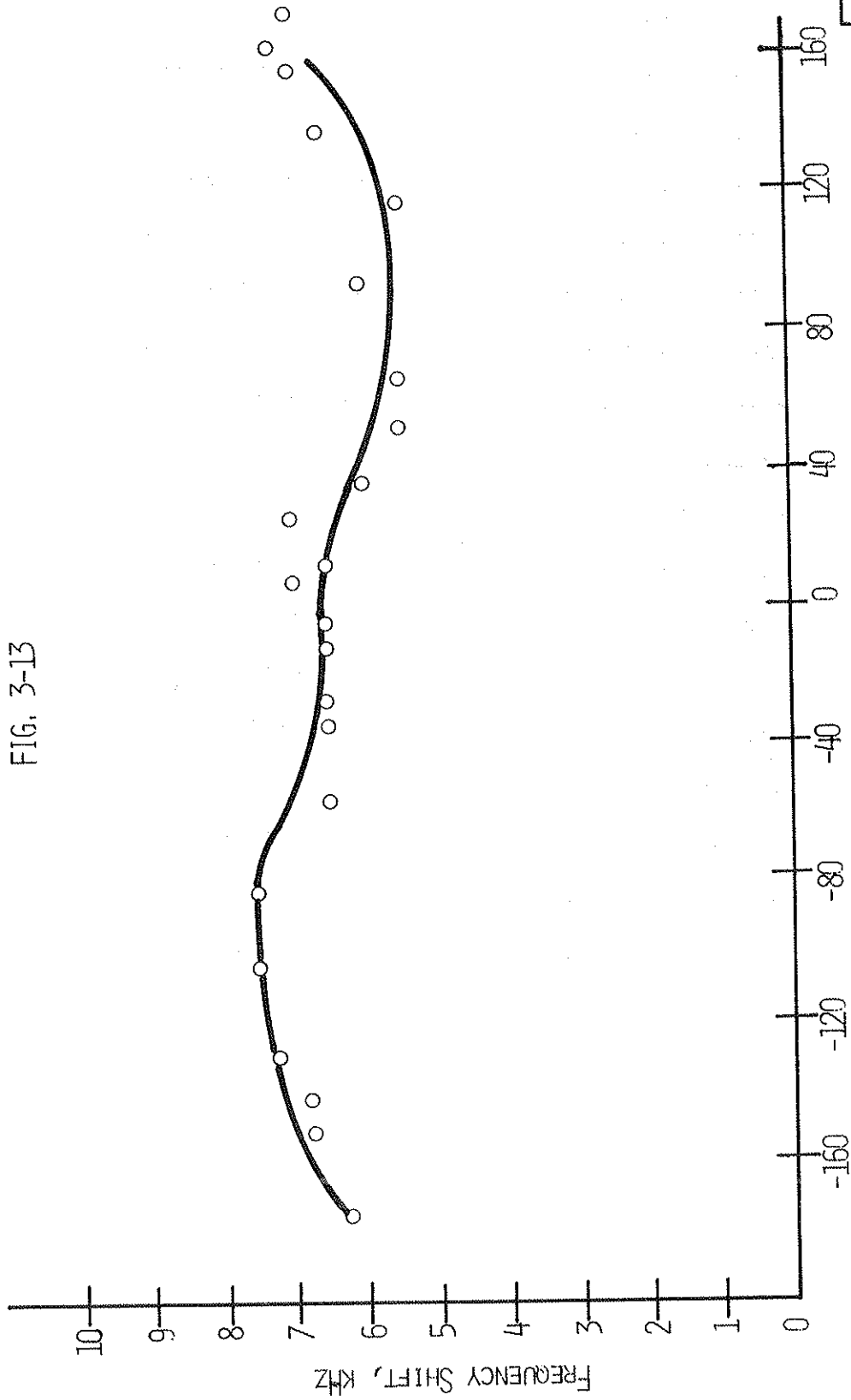


Figure 3-13 Frequency shift of a feedback suppressed trapped electron instability (maximum amplitude reduction factor - eight) versus the phase shift introduced in the feedback loop.

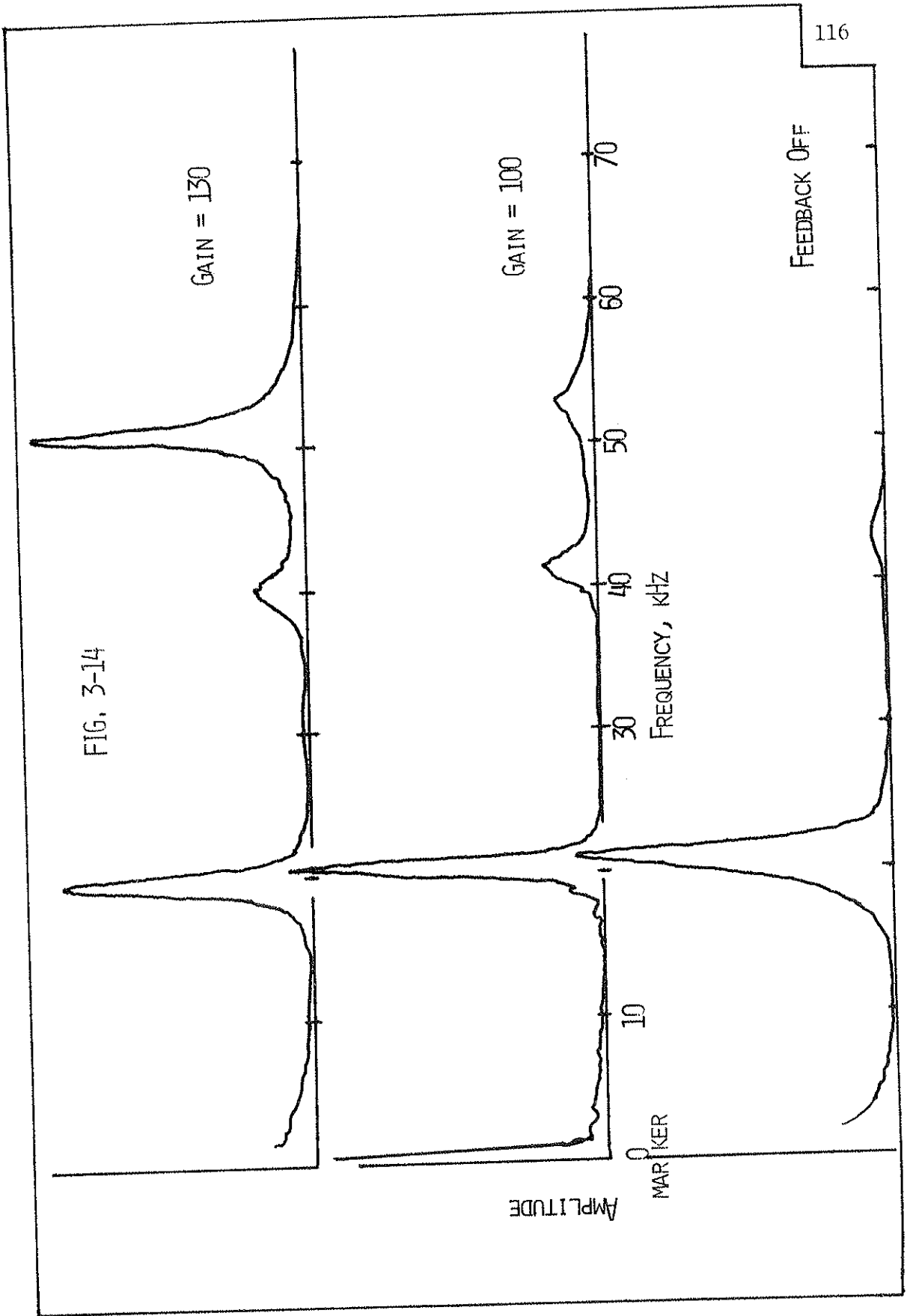
FIG. 3-13



stable region of the gain-phase space (Fig. 3-11). A mode can be indirectly destabilized if it was stable in the absence of feedback because it had "lost" in mode competition to the instability which is being feedback stabilized.¹⁴ Stabilizing the dominant mode can then lead to a "freeing" of the energy source required by the stable mode. Fig. 3-14 illustrates a situation where a second mode appeared as a trapped electron mode was being stabilized. Whether the second mode was directly or indirectly destabilized was not clear. In either case, the result was the same: no information on a stable equilibrium in the absence of the trapped electron mode could be made.

In order to circumvent the problems of nonlinear response and mode destabilization, we have made a systematic search of the available parameter space in the LMM. We had hoped to find a regime in which only a single trapped electron mode was present and in which we could obtain definitive results using feedback. It was this search which led us to the discovery of the FLR mode and the ULF oscillations described in Chapters 5 and 6. To date, though, we have not found a regime in which simple feedback experiments can be performed. Since our search has been reasonably extensive, I feel that we must now turn our attention to multi-mode feedback schemes like those employed by Richards.¹⁴ Such experiments are difficult at best and require a high degree of tuning and balancing of the feedback networks. At this time, however, I do not see a better alternative.

Figure 3-14 Destabilization of a second instability as the trapped electron instability is suppressed by feedback.



References for Chapter 3

1. A. W. Molvik, Wisconsin Plasma Physics Report PLP 341 (1970)
2. J. C. Sprott, Wisconsin Plasma Physics Report PLP 88 (1966)
3. D. W. Kerst, D. Lencioni, A. Cavallo, and J. Greenwood, Wisconsin Plasma Physics Report PLP 709 (1977)
4. J. D. Swift and M. J. R. Schwar, Electrical Probes for Plasma Diagnostics, American Elsevier, New York (1969)
5. J. G. LaFramboise, UTIAS No. 100 (University of Toronto, Toronto, 1966)
6. F. F. Chen in Plasma Diagnostic Techniques, ed. R. H. Huddleston and S. L. Leonard, Academic Press, New York (1965)
7. A. Hasegawa, Phys. Rev., 169, 204 (1968)
8. R. K. Richards and G. A. Emmert, Nuc. Fusion, 17, 205 (1977)
9. A. Sen, IEEE Trans. on Plasma Sci., PS-3, 163 (1975)
10. R. K. Richards, G. A. Emmert, and D. P. Grubb, Plasma Phys., 17, 271 (1975)
11. J. B. Taylor and C. N. Lashmore-Davis, Phys. Rev. Lett., 24, 1340 (1970)
12. N. A. Krall and A. W. Trivelpiece, Principles of Plasma Physics, McGraw-Hill Book Co., p. 617 (1973)
13. D. P. Grubb, R. K. Richards, and G. A. Emmert, Wisconsin Plasma Physics Report PLP 616 (1975)
14. R. K. Richards and G. A. Emmert, Wisconsin Plasma Physics Report PLP 617 (1975)

CHAPTER 4

EQUILIBRIUM PLASMA

All the experiments described in the following chapters were performed in the DC mode of operation of the Linear Multi-Mirror (LMM) experiment. (A pulsed mode of operation is available by gating the microwave power supply.) The plasma, therefore, was studied in a fully evolved, steady state equilibrium. The plasma parameters which describe such an equilibrium, e.g. n , T_e , ∇n , ∇T_e , etc. are strong functions of the controllable parameters of the experiment: the neutral gas pressure, pressure differential between the source and experimental regions, microwave power, average magnetic field strength, mirror ratio, and the length of the experimental region. Unfortunately (or realistically), changing one of the controllable parameters usually results in a non-negligible change in all of the plasma parameters.

This situation is further complicated by the fact that the equilibrium in the LMM is usually unstable, i.e. for almost any set of controllable parameters the plasma exhibits oscillations which are due to one or more instabilities. The effect which these instabilities have on the equilibrium plasma parameters is difficult to assess. It is nearly impossible to determine whether the instability modified the plasma parameters which then caused the mode to saturate at the observed amplitude or whether the observed equilibrium gives rise to the instability amplitude subject to a saturation mechanism which does not

require the alteration of the plasma parameters. Feedback stabilization of the instabilities is one of the few methods which can be employed to clearly reveal the changes in the equilibrium with and without the presence of the instabilities. As explained in Chapter 3, we have not yet been able to devise a feedback system which allows us to cleanly stabilize the trapped electron mode, so this question remains unresolved at this time.

With these provisos in mind, sets of typical plasma parameters are listed in Tables 4-1 through 4-5. Some of the values deserve further comment. In Table 4-3 it is noted that the ions are so collisional that they effectively do not see the mirrors and, therefore, random walk the length of the machine. This is in contrast to conventional mirror machine experiments where $T_i \gg T_e$ and the ions are the magnetically confined species. We can still define an effective mirror ratio which is analogous to that of conventional mirror machines¹

$$R_{\text{eff}} = \frac{B_{\text{MAX}}/B_{\text{MIN}}}{1 + T_i/T_e} .$$

Defining the mirror ratio in this manner takes account of the ambipolar electric field which is established to equalize the flow of ions and electrons out of the mirrors. For the LMM, however, $T_i \ll T_e$ so $R_{\text{eff}} \cong R$.

Also in Table 4-3 it is noted that the ionization and recombination rates are exceedingly small. The other possible source of plasma creation in the main body of the experiment would be due to ECRH from

TABLE 4-1

Plasma Parameters

Density	$n \sim 1 \times 10^{11} \text{ cm}^{-3}$
Electron Temperature	$kT_e \sim 5 \text{ eV}$
Ion Temperature	$kT_i \sim .1 \text{ eV}$
Ratio of plasma pressure to magnetic field pressure	$\beta \sim 1 \times 10^{-4} (\sim m_e/M_i)$
Low Frequency Dielectric Constant	$K \sim 1 \times 10^4$

TABLE 4-2

Velocities

Electron Thermal Velocity	$V_{T,e} \sim 1 \times 10^8 \text{ cm/s}$
Ion Thermal Velocity	$V_{T,i} \sim 2 \times 10^5 \text{ cm/s}$
Ion Sound Speed	$C_s \sim 2 \times 10^6 \text{ cm/s}$
Alfén Speed	$V_A \sim 2 \times 10^8 \text{ cm/s}$

TABLE 4-3

Frequencies

Electron Plasma	$\omega_{pe} \approx 2 \times 10^{10} \text{ sec}^{-1}$
Ion Plasma	$\omega_{pi} \approx 2 \times 10^8 \text{ sec}^{-1}$
Electron Cyclotron	$\Omega_e \approx 6 \times 10^9 \text{ sec}^{-1}$
Ion Cyclotron	$\Omega_i \approx 2 \times 10^6 \text{ sec}^{-1}$
Electron Bounce	$\omega_{be} \approx 1 \times 10^7 \text{ sec}^{-1}$ (short mirrors)
" "	" $\approx 2 \times 10^6 \text{ sec}^{-1}$ (long mirror)
Ion Bounce*	$\omega_{bi} \approx 1 \times 10^4 \text{ sec}^{-1}$ (short mirrors)
Electron Diamagnetic Drift	$\omega_{*e} \approx 3 \times 10^5 \text{ sec}^{-1}$

Collision Frequencies

Electron - Ion	$\nu_{ei} \approx 3 \times 10^5 \text{ sec}^{-1}$
Electron - Electron	$\nu_{ee} \approx 2\nu_{ei}$
Electron - Neutral	$\nu_{en} \approx 6 \times 10^5 \text{ sec}^{-1}$
Ion - Ion	$\nu_{ii} \approx 3 \times 10^5 \text{ sec}^{-1}$
Ion - Neutral	$\nu_{in} \approx 2 \times 10^4 \text{ sec}^{-1}$
Ionization Rate	$\nu_{ionize} \approx 3 \times 10^2 \text{ sec}^{-1}$
Recombination Rate	$\nu_{recomb.} \approx 10 \text{ sec}^{-1}$

* Since the ion mean free path is typically less than the connection length of the short mirror cells, the ions are not trapped but execute a random walk through the mirrors.

TABLE 4-4

Time Scales

Ion Thermalization	$\tau_{\theta ii} \sim 3 \mu\text{sec}$
Electron Thermalization	$\tau_{\theta ee} \sim 2 \mu\text{sec}$
Particle Confinement Time	$\tau_n \sim 0.5 \text{ msec}$
Energy Confinement Time	$\tau_E \sim 50 \mu\text{sec}$

TABLE 4-5

Scale Lengths

Density Scale Length	$\nabla n/n \sim 3 \text{ cm}^{-1}$ (radial)
Electron Temperature Scale Length	$\nabla T_e/T_e \sim 3 \text{ cm}^{-1}$ (radial)
Density Scale Length	$\partial n/\partial z \sim 0$ (axial)
Electron Temperature Scale Length	$\partial kT_e/\partial z \sim 0$ (axial)
Electron Gyro-radius	$\rho_e \sim 2 \times 10^{-2} \text{ cm}$
Ion Gyro-radius	$\rho_i \sim 0.3 \text{ cm}$
Ion Gyro-radius evaluated at the electron temperature	$\rho_H \sim 2 \text{ cm}$
Electron Debye Length	$\lambda_{De} \sim 5 \times 10^{-3} \text{ cm}$
Ion Debye Length	$\lambda_{Di} \sim 7 \times 10^{-4} \text{ cm}$

microwaves leaking out of the source. Measurements by the Radiation Safety department with detectors which are capable of detecting microwave levels as low as 0.1 mW/cm^2 failed to detect any leaking radiation. In addition, there are no resonance surfaces within the multi-mirror region except at the face of the end mirror which is over four meters from the plasma source. It is, therefore, believed that all of the plasma in the experimental region is created in the source region.

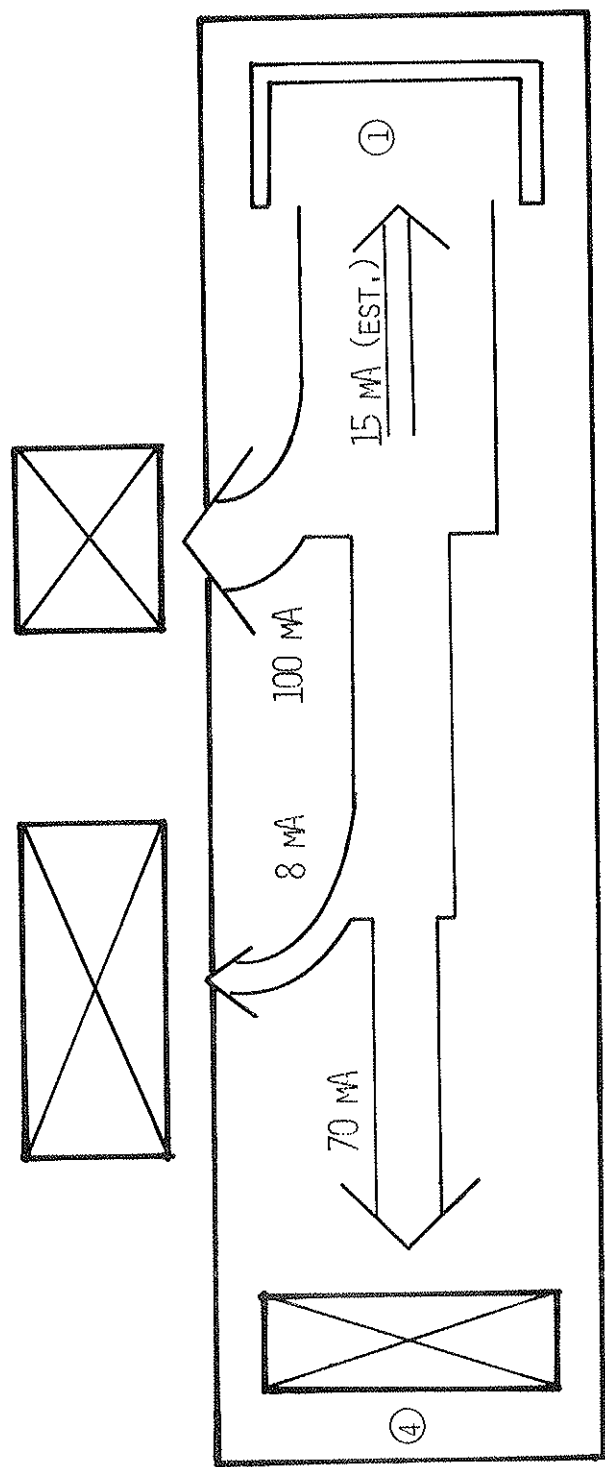
ECRH plasma sources are potential sources of anisotropic electron velocity distributions because the microwave energy is being pumped selectively into the perpendicular motion of the electrons. However, as shown in Table 4-4, the time for an electron to scatter through 90° by collisions with other electrons is short. The electrons, therefore, quickly relax to a Maxwellian.

The particle flux to striped collectors mounted on the walls of the vacuum chamber and the end mirror is shown schematically in Fig. 4-1. For these measurements the plasma was stable at a mirror ratio of 1.38. The dominance of the flux to the wall inside of the corrector coils is due to the bowing out of the field lines at these points. Particles that are cross-field diffusing radially outward will encounter a field line which intercepts the wall inside a corrector coil long before they reach a field line which intersects the wall inside of a main field coil.

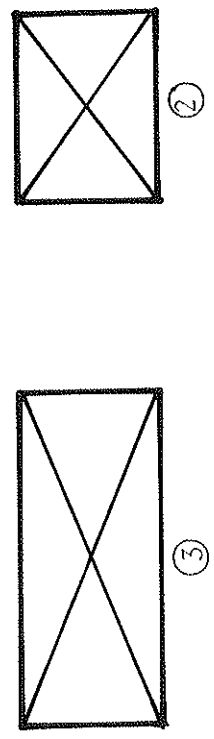
In equilibrium, the rate at which particles are lost to the walls and ends of the device must be equal to the rate at which particles are being created in the source. An approximate value for the particle

Figure 4-1 Schematic representation of the particle losses in the LMM as measured by striped collectors.

FIG. 4-1
SCHEMATIC OF PARTICLE FLUXES IN THE LM



- ① PLASMA SOURCE
- ② CORRECTOR COILS
- ③ MAIN FIELD COILS
- ④ END MIRROR



confinement time (Table 4-4) was obtained, therefore, by dividing the total number of particles in the experiment by the rate at which they were being created in the source (as determined by the flux to the collectors). The value thus obtained compares favorably with the value obtained by measuring the decay time of the ion saturation current when the source was gated off, $\tau_n \sim 0.3$ ms.

Similarly, the energy confinement time was estimated by equating the rate at which energy was being supplied to the source coil to the total energy in the plasma. The low value for τ_E probably reflects the rate at which energy is being lost to neutrals via charge exchange and electron-neutral collisions.

As noted in Table 4-5 the density and temperature gradients parallel to the magnetic field are zero. This is in contrast to the operation of the experiment when the plasma was terminated on a floating end plate. (For that situation $\partial T_e / \partial z \approx 0$, but there was a large density gradient parallel to \vec{B} .) The removal of the parallel density gradient is attributed to the large mirror ratio associated with the end mirror. The effectiveness of the end mirror is also apparent when the ion saturation current in the center of the plasma is measured along the z-axis. Even with a mirror ratio of 2.0, the ion saturation current only peaks by 10% in the mirrors which attests to the high degree of isotropy of the electrons.

In Table 4-6 I have listed the ranges over which the relevant collision mean free paths can be varied in LMM by changing the control-

TABLE 4-6

Mean Free Path

$$20 \text{ cm} \lesssim \lambda_{ei} \lesssim 10^3 \text{ m}$$

$$20 \text{ cm} \lesssim \lambda_{en} \lesssim 200 \text{ m}$$

$$.5 \text{ cm} \lesssim \lambda_{ii} \lesssim 7 \text{ cm}$$

$$3 \text{ cm} \lesssim \lambda_{in} \lesssim 10 \text{ m}$$

lable parameters. The range of electron mean free paths which are given in Table 4-6 cover the range from collisionless, $\lambda_e \gg L$, where L is the length of the plasma column in the experimental region ($L \approx 300$ cm) to collisional, $\lambda_e < l_c$ where l_c is the connection length of the short mirror cells ($l_c \approx 35$ cm).

In order to estimate the radial ambipolar electric field required to make the net current zero to the Pyrex walls of the vacuum chamber, we solve the zero order fluid equations for the ions and the electrons.² Using a slab model with a zero order density gradient in the minus x-direction and a uniform magnetic field in the z-direction we obtain for the electrons and ions

$$0 = -T_e \frac{\nabla n}{n} + e\nabla\phi - \frac{e}{c} (\vec{V}_e \times \vec{B}) - \frac{m \vec{V}_e}{\tau_e} \quad (4.1)$$

$$M_i \frac{d\vec{V}_i}{dt} = -e\nabla\phi + \frac{e}{c} (\vec{V}_i \times \vec{B}) - \frac{M_i \vec{V}_i}{\tau_i} \quad (4.2)$$

where we have assumed that $T_i \approx 0$.

Solving Eq. (4.1) for V_{oex} and Eq. (4.2) for V_{oix} we obtain

$$V_{oex} = \frac{b_e}{1 + (\Omega\tau)_e^2} \frac{d\phi_o}{dx} - \frac{D_e}{1 + (\Omega\tau)_e^2} \frac{1}{n_o} \frac{dn_o}{dx} \quad (4.3)$$

and

$$V_{oix} = - \frac{b_i}{1 + (\Omega\tau)_i^2} \frac{d\phi_o}{dx} \quad (4.4)$$

where $b_j = \frac{e\tau_j}{M_j}$, $D_e = \frac{T_e \tau_e}{m_e}$, $\Omega_j = \frac{eB}{M_j c}$, and τ_j is the inverse collision frequency for the j^{th} species. Setting $V_{oix} = V_{oex}$ we obtain

$$\frac{d\phi_o}{dx} = \frac{D_e}{b_e} \frac{1}{n_o} \frac{dn_o}{dx} \left[1 + \frac{b_i}{b_e} \left(\frac{1 + (\Omega\tau)_e^2}{1 + (\Omega\tau)_i^2} \right) \right]^{-1} \quad (4.5)$$

Noting that $(\Omega\tau)_i = \frac{b_i}{b_e} (\Omega\tau)_e$ and assuming $(\Omega\tau)_e \gg 1$ we obtain

$$\frac{d\phi_o}{dx} \approx \frac{D_e}{b_e} \frac{1}{n_o} \frac{dn_o}{dx} \left[\frac{(\Omega\tau)_i (\Omega\tau)_e}{1 + (\Omega\tau)_i^2} \right]^{-1} \quad (4.6)$$

Evaluating Eq. (4.6) for typical LMM parameters of $T_e = 5$ eV, $\tau_i = 5 \times 10^{-5}$, $\tau_e = 1 \times 10^{-6}$, $B = 250$ G, $1/n_o \frac{dn_o}{dx} = 3 \text{ cm}^{-1}$, we obtain

$$\frac{d\phi_o}{dx} \approx 4 \times 10^{-5} \frac{\text{statvolts}}{\text{cm}} = 1 \times 10^{-7} \frac{\text{V}}{\text{cm}} .$$

Since this value would cause an $\vec{E} \times \vec{B}$ rotation of the plasma which is much less than one radian per second, we will assume that the plasma frame is the same as the lab frame for a stable plasma.

In the unstable state the magnitude of the radial electric field will be determined by the transport processes characteristic of the nonlinearly saturated instabilities present. For example, it has been shown by Manheimer³ that the trapped electron instability which is nonlinearly saturated due to mode-mode coupling does not cause a radial electric field, and Cheng and Okuda⁴ have shown that in the saturated state convective cells cause an electric field which points radially inward.

As stated earlier in this chapter the equilibrium in the LMM is generally unstable to one or more modes of instability.

1) Flute Instability: One of the first modes of oscillation observed in the LMM was an $m = 1$ interchange instability driven by the average bad curvature in the multimirror region of the LMM. This mode propagates in the direction of the electron diamagnetic direction at a frequency, $f \sim 5$ kHz. The interchange mode is highly localized radially in the region of strong density gradient. The parallel wavenumber is ≈ 0 . This mode dominates in the plasma for low neutral gas pressures when the mirror ratio $\gtrsim 2.0$.

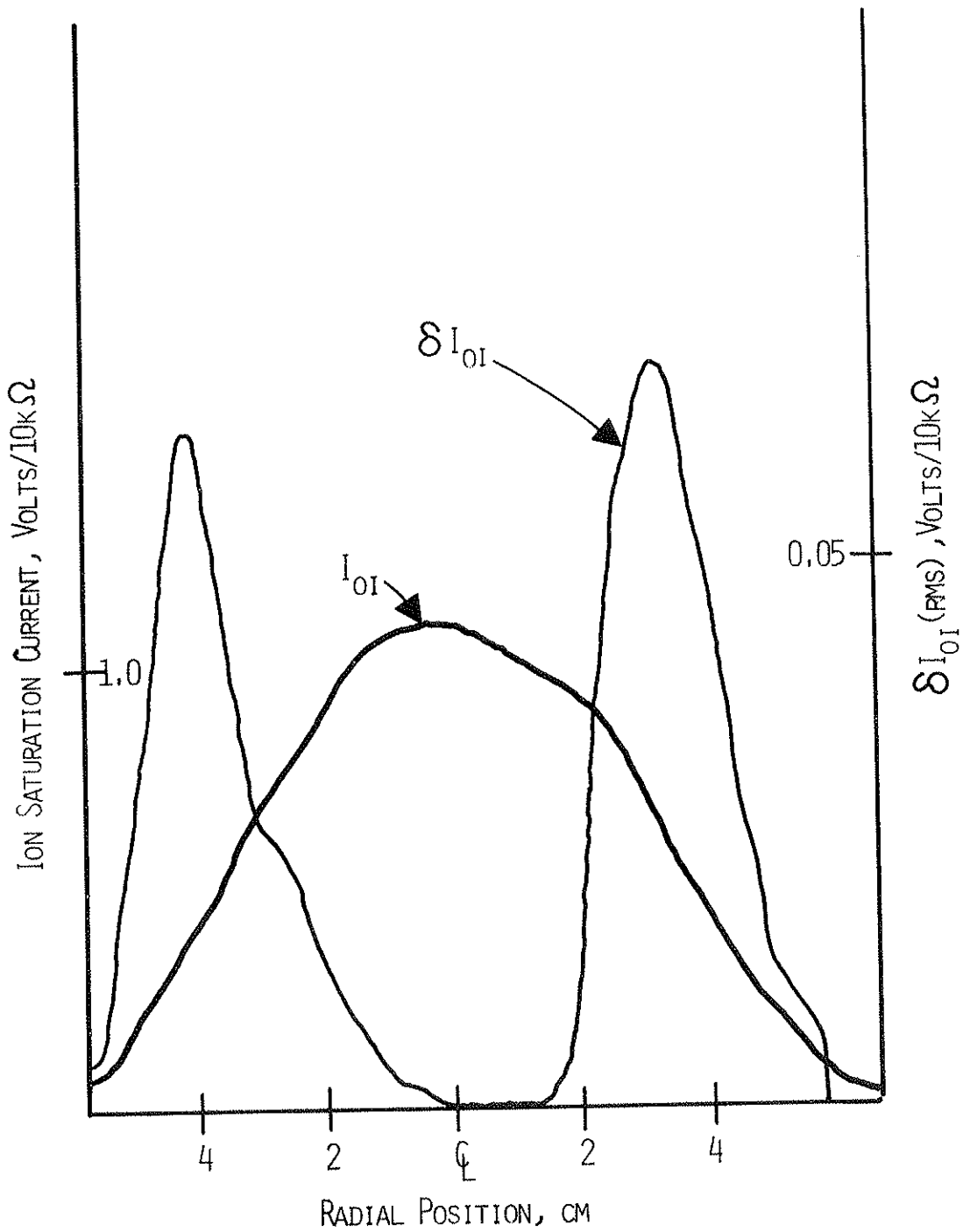
2) Collisional Drift Wave: A second instability appears when the LMM is operated at high neutral gas pressures. This instability has been identified as an $m = 1$ dissipative drift wave driven by electron-neutral collisions.⁵ The oscillations propagate in the direction of the electron diamagnetic drift at the diamagnetic frequency. The mode is highly localized radially in the region of strong density gradient (Fig. 4-2). The parallel wavenumber is $k_{||} \approx 2\pi/L$, where L is the length of the plasma column in the experimental region. The drift wave is observed in the plasma for mirror ratios $\lesssim 1.4$ with neutral gas pressures greater than 2×10^{-3} Torr. Both the interchange mode and the dissipative wave have been successfully studied using feedback stabilization.⁶

A third class of instabilities observed in the LMM is that of instabilities driven trapped electrons. These modes will be discussed in detail in Chapter 5.

There are at least three other modes which have been observed in

Figure 4-2 Radial profiles of the ion saturation current and the fluctuations caused by a dissipative drift wave.

FIG. 4-2



the LMM under very atypical operating conditions. Very little is known about these modes except that they occur at typical frequencies of 8 kHz, 60 kHz, and 100 kHz, respectively. They could be unidentified instabilities or presently recognized modes with different values of k_{\perp} and/or k_{\parallel} . Since they only appear for atypical operating conditions, they were not considered relevant to the present research and, therefore, not investigated further.

References for Chapter 4

1. D. J. Rose and M. Clark, Jr., Plasmas and Controlled Fusion, M.I.T. Press, Cambridge, Mass. (1961), page 379
2. A. V. Timofeev, Soviet Physics - Technical Physics, 8, 682 (1964)
3. W. M. Manheimer, E. Ott, K. R. Chu, J. P. Boris, and J. D. Callen, Nuc. Fusion, 16, 203 (1976)
4. C. Z. Cheng and H. Okuda, Phys. Rev. Lett., 38, 708 (1977)
5. R. J. Fonck, W. C. Guss, and D. M. Meade, Bull. Am. Phys. Soc., 18, ser 2, 1320 (1973)
6. D. P. Grubb, G. A. Emmert, and R. K. Richards, Wisconsin Plasma Physics Report PLP 616 (1975)

CHAPTER 5

THE DISSIPATIVE TRAPPED ELECTRON INSTABILITY
IN THE LINEAR MULTI-MIRROR DEVICE

As noted in Chapter 1 the plasma in a linear multimirror experiment has all the properties necessary for the excitation of the dissipative trapped electron mode (DTEM): trapped and pseudo-transit electrons, radial gradients of both the density and the electron temperature, and finite ion Larmor radius effects. When operated in the correct collisionality regime such a plasma should be unstable to the DTEM. In this chapter we derive a dispersion relation for the DTEM which includes the plasma phenomena relevant to the stability of the DTEM in the Linear Multi-Mirror (LMM) and compare the theoretical predictions with the experimental data.

Theory

A slab model geometry (Fig. 5-1) is assumed for the analysis; the magnetic field is oriented in the (+) Z-direction and the zero-order gradients of the density and electron temperature are in the (-) X-direction. A list of the symbols used appears in Table 5-1. The perturbed quantities have the form $\tilde{A} = A_0 \exp[i(\vec{k} \cdot \vec{x} - \omega t)]$. Since $\beta < m_e/M_i$ for the plasma in the LMM we will only consider electrostatic instabilities. We also restrict the analysis to low frequency, drift type modes such that the frequency of the oscillation is less than the ion cyclotron frequency, $\omega < \Omega_i$, and the parallel phase velocity is

Figure 5-1 Slab model co-ordinate system used in the derivation of the dispersion relation of the dissipative trapped electron instability.

FIG. 5-1

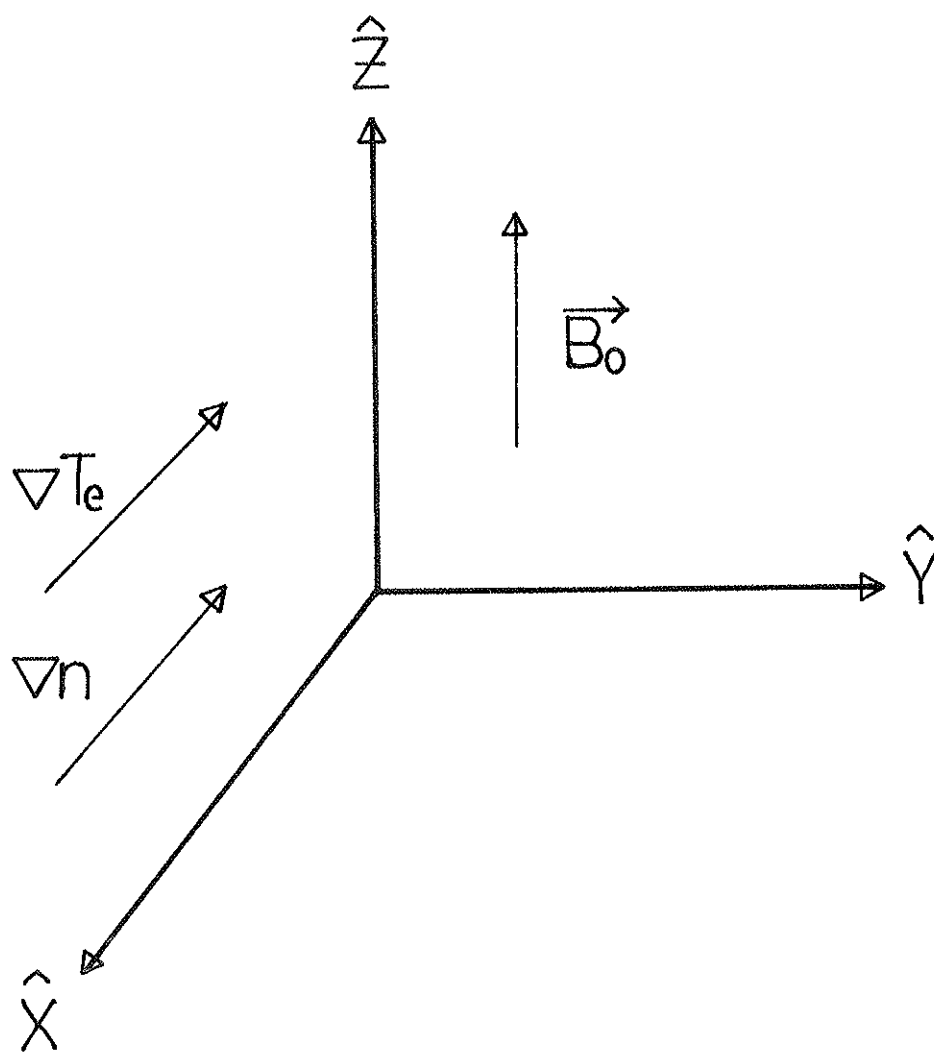


Table 5-1

M	Mirror ratio
ϵ	$= (M-1)/M \approx \sqrt{2} r/R$ in a toroid
$\sqrt{\epsilon}$	\approx fraction of trapped electrons
m_e	electron mass
M_i	ion mass
n_0	plasma density
$\tilde{n}_{e,c}$	perturbation of circulating electron density
$\tilde{n}_{e,t}$	perturbation of trapped electron density
\tilde{n}_i	perturbation of ion density
ρ	charge density
T_e	electron temperature ($k_{\text{Boltzmann}}$ included)
T_i	ion temperature ($k_{\text{Boltzmann}}$ included)
β	ratio of plasma pressure to magnetic field pressure
ϕ	potential oscillations associated with a wave
\vec{E}	electric field associated with a wave
\vec{B}	magnetic field
ω	$= \omega_r + i\gamma$
ω_r	real frequency
γ	growth rate
ω_{be}	$= 2\pi \sqrt{\epsilon} v_{T,e} / \lambda_c$
ω_{*i}	ion diamagnetic frequency
ω_{*e}	electron diamagnetic frequency
ω_{*t}	$= \omega_{*e} [1 + \eta_e (E/T_e - 3/2)]$

ν_{ii}	ion-ion collision frequency
ν_e	electron Coulomb collision frequency
ν_{en}	electron-neutral collision frequency
ν_{eff}	$= (\nu_e/\epsilon)(\nu_{T,e}/v)^3$
Ω_i	ion cyclotron frequency
$k_{ }$	parallel wave number
k_{\perp}	perpendicular wave number
l_c	connection length of mirror cells
ρ_i	ion gyro-radius
r_{Di}	ion Debye length
η_e	ratio of electron temperature scale length to density scale length
η_i	ratio of ion temperature scale length to density scale length
$v_{T,e}$	electron thermal speed
$v_{T,i}$	ion thermal speed
\vec{v}_d	guiding center drift velocity
$S_0(b)$	$= I_0(b)e^{-b}$
$I_0(b)$	modified Bessel function
κ	dielectric function
b	$= \frac{1}{2}(k_y \rho_i)^2$

greater than the ion thermal velocity but less than the electron thermal velocity, $v_{T,i} < \omega/k_{\perp} < v_{T,e}$. Finally, we limit the effective electron collision frequency to values less than the effective electron bounce frequency in the short mirror cells, $\nu_{\text{eff}} < \omega_{be}$.

The perturbation of the ion density is derived from the continuity equation

$$\frac{\partial \tilde{n}}{\partial t} + \nabla \cdot \vec{n}\vec{v} = 0, \quad (5.1)$$

which to 1st order in the perturbed quantities is

$$\frac{\partial \tilde{n}}{\partial t} + \nabla n_o \cdot \vec{v}_d + n_o (\nabla \cdot \vec{v}_d) = 0. \quad (5.2)$$

For the drift velocity of the ions we include the $\vec{E} \times \vec{B}$ drift with finite ion Larmor radius corrections¹ (FLR) and the polarization drift,

$$\vec{v}_d = \frac{-ik_y \tilde{\phi}}{B} \left(1 - \frac{k_y^2 \rho_i^2}{4}\right) \hat{x} - \frac{\omega}{\Omega_i} \frac{k_y \tilde{\phi}}{B} \hat{y}. \quad (5.3)$$

Inserting Eq. (5.3) into Eq. (5.2) and defining $\omega_{*i} = \frac{-c}{eB} k_y T_i \frac{\nabla n}{n}$ and $b = \frac{1}{2} (k_y \rho_i)^2$ we arrive at the perturbation of the ion density

$$\frac{\tilde{n}_i}{n_o} = \frac{e\tilde{\phi}}{T_i} \left[\frac{\omega_{*i}}{\omega} (1-b) - b \right]. \quad (5.4)$$

In deriving Eq. (5.4) we have ignored the following: (1) the ion ∇B and curvature drifts, (2) the ion response along the field line, (3) the presence of trapped ions, (4) ion Landau damping, and (5) ion viscosity.

For the ions in the LMM $T_i \approx .1$ eV so it is easy to show that the first four effects are negligible. We will return to the subject of ion viscosity later in this chapter.

We consider now the perturbed density of the two classes of electrons. We assume that the circulating electrons are in equilibrium with the wave so that they have a Boltzmann distribution, which for $e\tilde{\phi}/T_e \ll 1$ has the approximate form

$$\tilde{n}_{e,c}/n_o \approx (e\tilde{\phi}/T_e)(1 - \sqrt{\epsilon}) \quad (5.5)$$

where we have assumed that the fraction of trapped electrons is approximately equal to $\sqrt{\epsilon}$ (Table 5.1). The perturbation of the circulating electron density given by Eq. (5.5) is adequate when the plasma is deeply in the trapped electron regime so that the plasma is dominated by the DTEM. However, in the limit that the fraction of trapped electrons goes to zero ($\sqrt{\epsilon} \rightarrow 0$) this form for the perturbed density will not give rise to either collisional or collisionless drift waves in those collisionality regimes.

To find the perturbation of the density of trapped electrons we solve the drift kinetic equation:

$$\frac{\partial f}{\partial t} + v_z \frac{\partial f}{\partial z} + q/m E_z \frac{\partial f}{\partial v_z} + \nabla \cdot (\vec{v}_d f) = \left. \frac{\partial f}{\partial t} \right|_C \quad (5.6)$$

For the collision term we choose a simple relaxation model operator²

$$\left. \frac{\partial f}{\partial t} \right|_C = -\nu_{\text{eff}} (f - f_o) \quad (5.7)$$

where $v_{\text{eff}} = \frac{v_e}{\epsilon} \left(\frac{v_{T,e}}{v} \right)^3$. Since a trapped electron need only scatter through a small angle in velocity space to become detrapped, the collision frequency for the trapped electrons is enhanced by a factor $1/\epsilon$. This term can be derived from a random walk argument. However, in deriving this term, it is necessary to assume that the sine of the angle of the trapped region of velocity space is equal to the angle itself, $\sin\theta \approx \theta$. This limits the applicability of this form of the collision operator to mirror ratios less than three. The velocity dependence in Eq. (5.7) arises from the velocity dependence of the Rutherford cross section for Coulomb collisions.

This relaxation model collision operator is useful to describe electron-ion collisions. It is less accurate, though, at describing electron-electron collisions. Other authors^{3,4} have shown, however, that its use leads to qualitatively correct results, which is all we require at this time.

The $\vec{E} \times \vec{B}$ drift is assumed to be the only important guiding center drift in Eq. (5.6) so we set $v_j = -i k_y \tilde{\phi}/B$. In doing so, we have neglected the ∇B and curvature drifts. These terms are important in the low collisionality regime; however, for the experiments described in this chapter these terms are negligible. After putting v_d into Eq. (5.6), assuming that f_0 is a Boltzmann distribution, and grinding through a lot of algebra, we arrive at the perturbation of the trapped electron density,

$$\frac{\tilde{n}_{e,t}}{n_0} = \sqrt{\epsilon} \frac{e\tilde{\phi}}{T_e} \left(1 - \left\langle \frac{\omega - \omega_T^*}{\omega + i\nu_{\text{eff}}} \right\rangle \right) \quad (5.8)$$

where $\omega_T^* = \omega_{*e} [1 + \eta_e (E/T_e - 3/2)]$, $\eta_e = \frac{d \ln T_e}{d \ln n}$, and the brackets indicate that the enclosed quantity is averaged over a Maxwellian distribution in velocity space, i.e.

$$\langle A \rangle = \frac{1}{n_0} \int \frac{A}{(2\pi)^{3/2}} \exp(-v^2/v_{T,e}^2) \frac{d^3v}{v_{T,e}^3} \quad (5.9)$$

Invoking quasi-neutrality, $\tilde{n}_i = \tilde{n}_{e,c} + \tilde{n}_{e,t}$, we obtain

$$\frac{1}{T_i} \left[\frac{\omega_{*i}}{\omega} (1-b) - b \right] = \frac{1}{T_e} \left[1 - \sqrt{\epsilon} \left\langle \frac{\omega - \omega_T^*}{\omega + i\nu_{\text{eff}}} \right\rangle \right] \quad (5.10)$$

If we define $\tau = T_e/T_i$ and rearrange the terms in Eq. (5.10) we obtain the result

$$1 + \tau - \left(\tau + \frac{\omega_{*e}}{\omega} \right) (1-b) = \sqrt{\epsilon} \left\langle \frac{\omega - \omega_T^*}{\omega + i\nu_{\text{eff}}} \right\rangle . \quad (5.11)$$

In the limit that the FLR effects are negligible ($b \rightarrow 0$) and assuming that the real part of the frequency is approximately equal to the electron diamagnetic frequency ($\omega_r \approx \omega_{*e}$), we obtain the dispersion relation derived by Kadomtsev and Pogutse⁵

$$\omega \approx \omega_{*e} + i\sqrt{\epsilon} \left\langle \frac{(\omega_T^* - \omega_{*e})}{\omega_{*e}^2 + \nu_{\text{eff}}^2} \nu_{\text{eff}} \right\rangle . \quad (5.12)$$

Because of the velocity space averaging required to evaluate Eq. (5.12) it is necessary to employ numerical techniques in order to calculate the growth rate for an arbitrary collision frequency. The growth rate as a function of the normalized collision frequency (collisionality)

calculated from Eq. (5.12) is shown in Fig. 5-2. The curve labeled $v_{en}/(v_e/\epsilon) = 0$ is that for a fully ionized plasma. However, the plasma in the LMM is only partially ionized with the ratio $v_{en}/(v_e/\epsilon) \lesssim 1$. In order to predict the effects of electron-neutral collisions, it is necessary to include a velocity independent collision term in v_{eff} . (For the temperature range $T_e \lesssim 20$ eV, the electron-neutral collision frequency in a Helium plasma is approximately independent of the electron temperature.) The result of one of these calculations is the curve labeled $v_{en}/(v_e/\epsilon) = 1$ in Fig. 5-2. As is shown in this figure, the inclusion of the collisions with neutrals shifts the point of maximum growth rate towards lower Coulomb collisionality and reduces the maximum growth rate. It is easy to show that the growth rate predicted by Eq. (5.12) goes to zero in the limit that the ratio $v_{en}/(v_e/\epsilon)$ approaches infinity.

Eq. (5.11) is the same as the dispersion relation derived by Liu, Rosenbluth, and Tang⁶ in the limit that $S_0(b) \approx 1-b$ and neglecting ion Landau damping. In these same limits and assuming that $v_{eff} > \omega$, they find that the real part of the frequency and the growth rate are given by the approximate relations

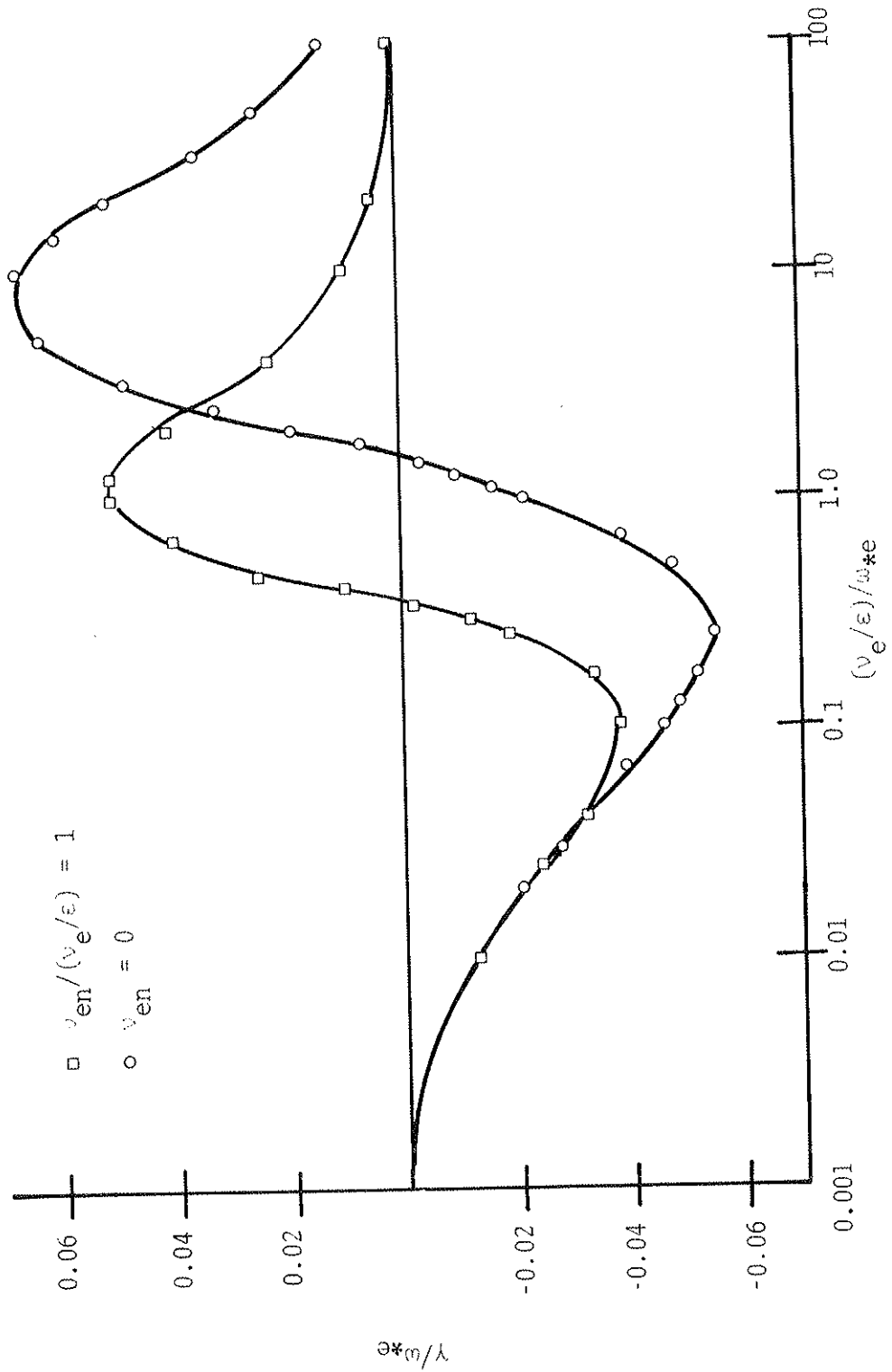
$$\omega_r = \frac{\omega_{*e}(1-b)}{1+\tau b}, \quad (5.13)$$

$$\gamma \approx \left(\epsilon^{\frac{3}{2}} \frac{\omega_{*e}^2}{v_e} \right) \left[\frac{(3\eta/2)[1+b(\tau-1)] + (1+\tau)b}{(1+\tau b)^3} \right]. \quad (5.14)$$

Once again, in the limit $b \rightarrow 0$, we recover the DTEM driven by the elec-

Figure 5-2 The growth rate of the trapped electron mode as a function of the electron collisionality calculated without the finite ion Larmor radius corrections to the theory or ion viscosity. Since the plasma in the Linear Multi-Mirror is only partially ionized, the electron - neutral collision frequency has been included as a parameter. For a fully ionized plasma, $\nu_{en} = 0$.

FIG. 5-2



tron temperature gradient, the ∇T_e mode. However, in the limit $\nabla T_e \rightarrow 0$ ($\eta_e \rightarrow 0$) the DTEM still can have a positive growth rate. In this case, the mode is driven by the finite Larmor radius effects through the term b , an FLR mode.

In order to include the effects of ion viscosity in our analysis we return to the basic dispersion relation for electrostatic instabilities

$$\delta\rho = \frac{k^2}{4\pi} (1 - \kappa) \phi \quad (5.15)$$

where $\kappa = 1 + \delta\kappa_e + \delta\kappa_i$. $\delta\kappa_e$ and $\delta\kappa_i$ are the contributions to the dielectric function due to the perturbations of the electron density and ion density, respectively, so that

$$\delta\kappa = -\frac{k^2}{4\pi} (\delta\kappa_e + \delta\kappa_i) \phi \quad (5.16)$$

Using a derivation similar to that of Braginskii⁷, Rukhadze and Silin⁸ found that the contribution to the dielectric function due to the effects of ion viscosity is given by

$$\begin{aligned} \delta\kappa_{ii} = \frac{i}{10} \frac{v_{ii}}{\omega} \frac{v_{T,i}^4}{k^2 r_{Di}^2} & \left[\left(\frac{16k_z^4}{\omega^4} + \frac{28k_z^2 k_y^2}{\omega^2 \Omega_i^2} + \frac{7k_y^4}{\Omega_i^4} \right) \cdot \right. \\ & \left. \left(1 - \frac{k_y v_{T,i}^2}{\omega \Omega_i} \frac{\partial \ln n}{\partial x} \right) - \left(\frac{24k_z^4}{\omega^4} + \frac{33}{2} \frac{k_z^2 k_y^2}{\omega^2 \Omega_i^2} - \frac{3}{4} \frac{k_y^4}{\Omega_i^4} \right) \cdot \right. \\ & \left. \left. \frac{k_y v_{T,i}^2}{\omega \Omega_i} \frac{\partial \ln T_i}{\partial x} \right] \quad (5.17) \end{aligned}$$

for drift waves. Since the ions are not magnetically trapped in the

mirror cells of the LMM, Eq. (5.17) also describes the effects of ion viscosity for the DTEM in this device.

For the trapped electron modes observed in the LMM $k_z \ll k_y$ so Eq. (5.17) can be simplified considerably;

$$\begin{aligned} \delta\kappa_{ii} \approx & \frac{i}{10} \frac{v_{ii}}{\omega} \frac{v_{T,i}^4}{k^2 r_{Di}^2} \left[\frac{7k_y^4}{\Omega_i^4} \left(1 - \frac{k_y v_{T,i}^2}{\omega \Omega_i} \right) \frac{\partial \ln x}{\partial x} \right. \\ & \left. + \frac{3}{4} \frac{k_y^4}{\Omega_i^4} \left(\frac{k_y v_{T,i}^2}{\omega \Omega_i} \frac{\partial \ln T_i}{\partial x} \right) \right] . \end{aligned} \quad (5.18)$$

Rearranging terms and using the definitions of b and ω_{*i} , we arrive at

$$\delta\kappa_{ii} = .7i \frac{v_{ii}}{\omega} \frac{b^2}{k^2 r_{Di}^2} \left(1 - \frac{\omega_{*i}}{\omega} \left(1 - \frac{3}{28} \eta_i \right) \right) . \quad (5.19)$$

Putting Eq. (5.19) into Eq. (5.16) we find that the contribution to the perturbed ion density due to ion viscosity is given by

$$\delta\rho_{ii} = e \delta n_{ii} = \frac{i}{4\pi} \left[.7 \frac{v_{ii}}{\omega} \frac{b^2}{r_{Di}^2} \left(1 - \frac{\omega_{*i}}{\omega} \left(1 - \frac{3}{28} \eta_i \right) \right) \right] \tilde{\phi} . \quad (5.20)$$

Recalling that $r_{Di}^2 = kT_i/4\pi n e^2$, we obtain

$$\delta n_{ii} = \frac{e\tilde{\phi}}{T_e} \left[0.7i \frac{v_{ii}}{\omega} \tau b^2 \left(1 - \frac{\omega_{*i}}{\omega} \left(1 - \frac{3}{28} \eta_i \right) \right) \right] \tilde{\phi} . \quad (5.21)$$

For the plasma in the LMM $\omega_{*i}/\omega \ll 1$ and $\eta_i \approx 0$ so

$$\delta n_{ii} \approx -i \left[\frac{e\tilde{\phi}}{T_e} \left(0.7 \frac{v_{ii}}{\omega} \tau b^2 \right) \right] . \quad (5.22)$$

When we add Eq. (5.22) to Eq. (5.4) and reevaluate the quasi-neutrality condition we find

$$\omega \left[1 - \sqrt{\epsilon} \left\langle \frac{\omega - \omega_T^*}{\omega + i v_{\text{eff}}} \right\rangle + \tau b \right] = \omega_{*e} - 0.7i v_{ii} \tau b^2 \quad (5.23)$$

We note that $\omega = \omega_r + i\gamma$ and assume that $\gamma^2 \ll \omega_R^2$. We further assume that $\gamma < v_{\text{eff}}$. With these assumptions we expand Eq. (5.23) and rearrange terms to get

$$\begin{aligned} (\omega_r + i\gamma) \left[(1 + \tau b) - \sqrt{\epsilon} \left\langle \frac{\omega_r^2 - \omega_r \omega_T^* + v_{\text{eff}} \gamma}{\omega_r^2 + v_{\text{eff}}^2} \right\rangle - \right. \\ \left. i\sqrt{\epsilon} \left\langle v_{\text{eff}} \frac{(\omega_T^* - \omega_r)}{\omega_r^2 + v_{\text{eff}}^2} \right\rangle \right] = \omega_{*e} - 0.7i \tau b^2 v_{ii} . \quad (5.24) \end{aligned}$$

For convenience we define

$$\langle (1) \rangle = \left\langle \frac{\omega_r^2 - \omega_r \omega_T^* - v_{\text{eff}} \gamma}{\omega_r^2 + v_{\text{eff}}^2} \right\rangle \quad (5.25)$$

and

$$\langle (2) \rangle = \left\langle \frac{v_{\text{eff}} (\omega_T^* - \omega_r)}{\omega_r^2 + v_{\text{eff}}^2} \right\rangle . \quad (5.26)$$

Equating the real and imaginary parts of Eq. (5.24) we obtain

$$(1 + \tau b)\omega_r - \sqrt{\epsilon}[\omega_r \langle (1) \rangle - \gamma \langle (2) \rangle] = \omega_{*e} \quad (5.27)$$

and

$$(1 + \tau b)\gamma - \sqrt{\epsilon}[\gamma \langle (1) \rangle + \omega_r \langle (2) \rangle] = -0.7i v_{ii} \tau b^2 \quad (5.28)$$

These equations reduce to

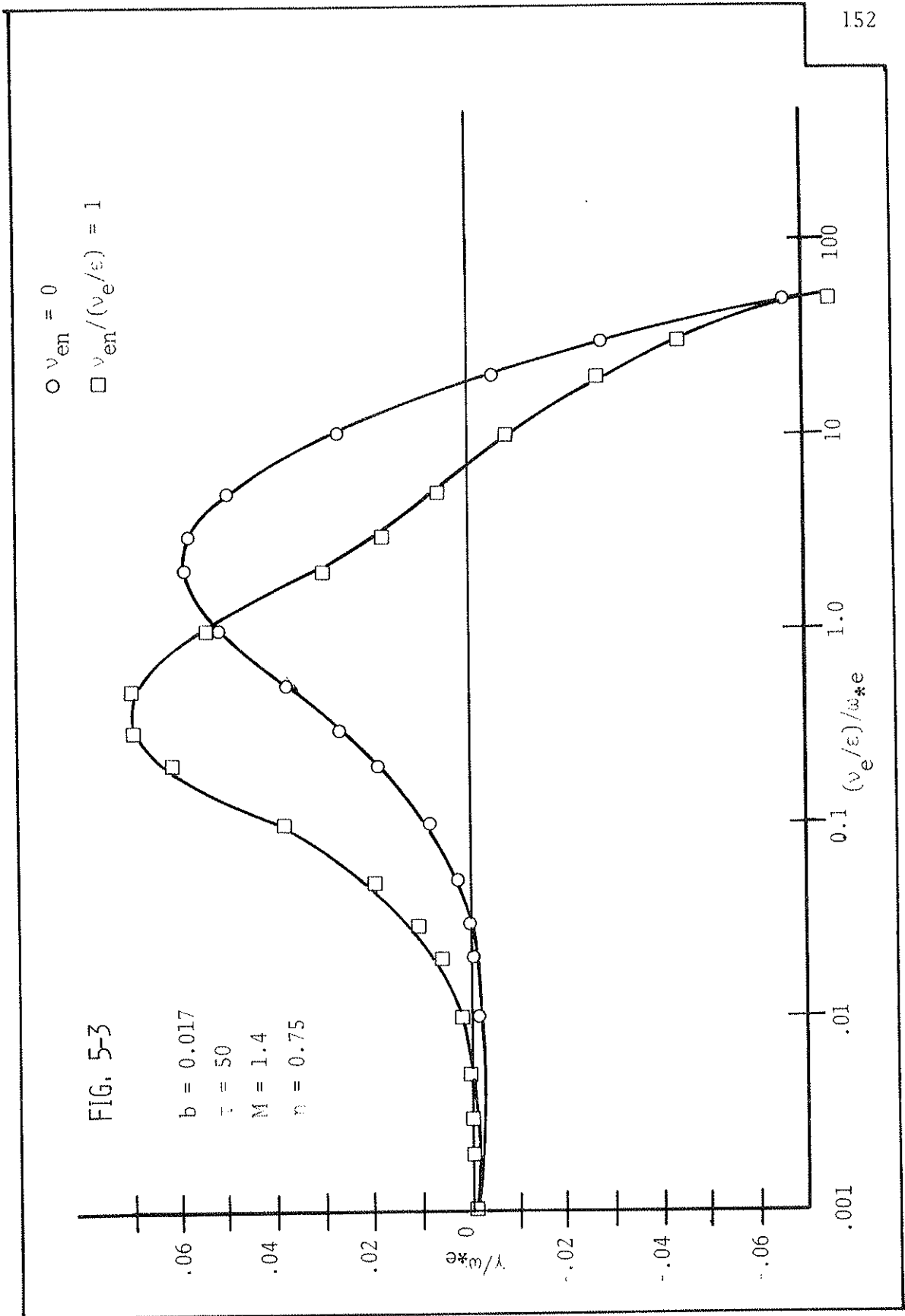
$$\omega_r = \frac{\omega_{*e} - \sqrt{\epsilon} \gamma \langle(2)\rangle}{1 + \tau b - \sqrt{\epsilon} \langle(1)\rangle} \quad , \quad (5.29)$$

$$\gamma = \frac{\sqrt{\epsilon} \omega_r \langle(2)\rangle - 0.7v_{ii} \tau b^2}{1 + \tau b - \sqrt{\epsilon} \langle(1)\rangle} \quad . \quad (5.30)$$

Values for ω_r and γ are found by making an initial guess of the magnitude of these terms and then numerically evaluating the velocity space averages $\langle(1)\rangle$ and $\langle(2)\rangle$. Eq. (5.29) and (5.30) are then solved to generate new values for ω_r and γ . This process is iterated until the values for both ω_r and γ converge.

A code using this process was developed and used to calculate the variations of the growth rate as a function of the collisionality. The result, shown in Fig. 5-3, indicates a very different parametric dependence of the growth rate on the collisionality than that shown in Fig. 5-2. These differences arise due to the non-zero value of b (FLR effects). For the values of the growth rate shown in Fig. 5-3, $\tau b = 0.84$. The shift in the peak of the growth rate toward lower collisionality is due to ion viscosity, which causes the rapid decrease of the growth rate at high collisionality and the addition of the FLR driving terms in the growth rate, which allow the DTEM to be unstable at lower collisionality. The inclusion of electron-neutral collisions again shifts the peak in the growth rate toward lower Coulomb collisionality. However, with the inclusion of large FLR effects the maximum growth rate is now slightly larger with electron-neutral collisions than without. It appears, therefore, that the trapped electron instability

Figure 5-3 The growth rate of the trapped electron mode as a function of the electron collisionality including the finite ion Larmor radius effects and ion viscosity. Since the plasma in the Linear Multi-Mirror is only partially ionized, the electron-neutral collision frequency is included as a parameter. For a fully ionized plasma, $\nu_{en} = 0$.



described by the parameters given in Fig. 5-3 is not damped by the presence of electron-neutral collisions even for $\nu_{en}/(\nu_e/\epsilon) = 1$.

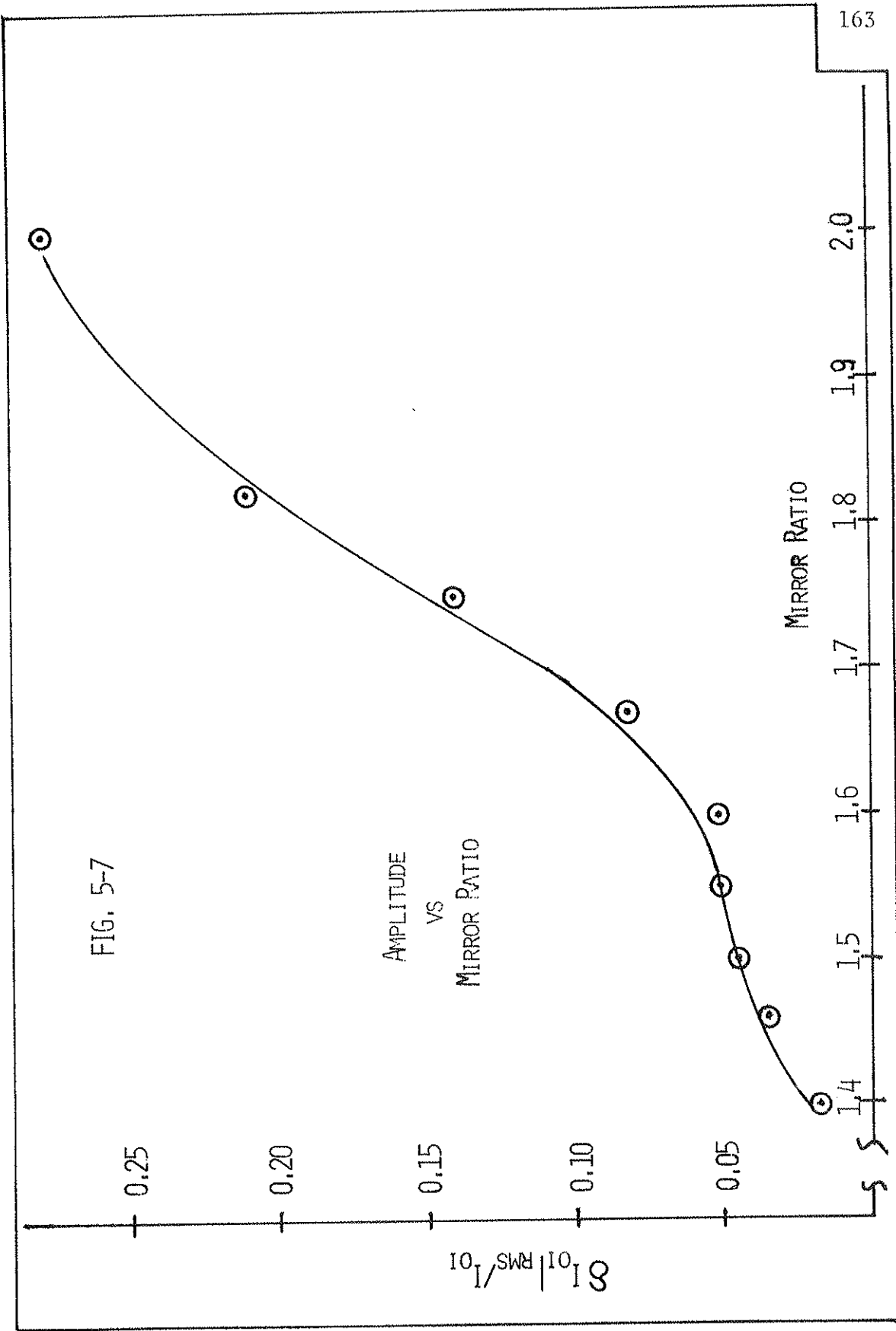
Other theoretical predictions obtained using this code will be presented later in this chapter.

Experimental Observations

The initial experiments aimed at the detection of the DTEM were performed in the low collisionality regime where Deschamps et al.⁹ had reported observation of this instability. The plasma density was a few times 10^{10} cm^{-3} with electron temperatures in the range 10 - 20 eV. The collisionality of this plasma was in the range $0.01 \lesssim (\nu_e/\epsilon)/\omega_{*e} \lesssim 0.1$. In this regime we observed an instability which had an azimuthal mode number, m , equal to one, propagated in the direction of the electron diamagnetic drift, and increased in amplitude as the mirror ratio was increased. However, the mode frequency was much less than the electron diamagnetic drift frequency, and the mode exhibited a parallel wavelength which was at least many times the length of the experiment. We subsequently employed feedback stabilization techniques to determine whether the mode was reactive or dissipative.

The change in the mode frequency and amplitude as a function of the phase shift introduced in the feedback loop are shown in Fig. 5-4. The frequency jump at the point of maximum suppression is clearly evident in this figure; this labels the mode we were studying as being reactive. Based upon this data, it appeared that the only instability which we observed in the very low collisionality regime was a collision-

Figure 5-7 Response of the V_{T_e} mode to an increase in the mirror ratio: saturation amplitude versus mirror ratio.



dissipative. (The phase change would have been $\gtrsim 130^\circ$ for a reactive mode.)

The data presented so far are in agreement with the theoretically predicted behavior of the DTEM. A closer check on the correlation between the theory and the experiment required us to vary a critical parameter, such as the collisionality, and relate the observed changes to those predicted by the theory. This is not an easy experiment to perform in the LMM. As noted in Chapter 4, changing one of the controllable parameters typically results in changes in more than one of the plasma parameters. It is possible, however, to vary either the microwave power or the neutral gas pressure without significantly changing the gradients of the density and electron temperature. The density and electron temperature change almost uniformly across the plasma column as these parameters are varied. By monitoring the changes in the density and electron temperature as the microwave power or the neutral gas pressure is varied, it is possible to determine the values of $(\nu_e/\epsilon)/\omega_{*e}$ and $\nu_{en}/(\nu_e/\epsilon)$ and put these terms into the dispersion relation code and calculate the resulting frequency and growth rate for each incremental change of the controllable parameter.

The dispersion relation predicts the value of the growth rate. Without feedback stabilization we are only able to measure the saturated amplitude of the instability and assume that is directly related to the growth rate. The comparisons which are made between the experimental data and the theoretically predicted growth rate, therefore, are only of a qualitative nature and are not meant to imply quantitative agree-

Figure 5-8 Transfer function response - amplitude - of a plasma which was marginally stable to a trapped electron instability.

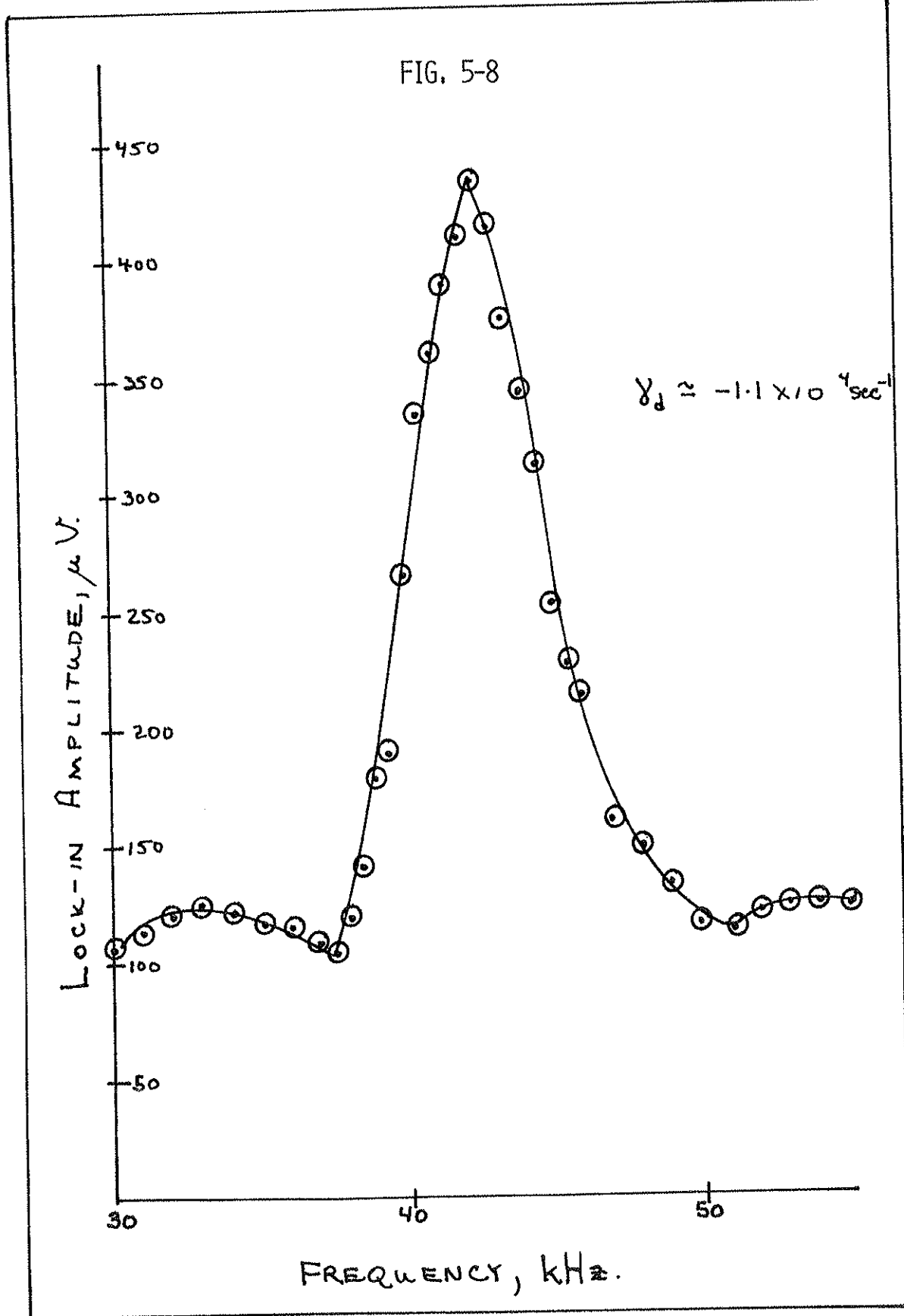


Figure 5-9 Transfer function response - phase - of a plasma which was marginally stable to a trapped electron instability.

Figure 5-10 Variation of the theoretically predicted and the experimentally observed frequency of the VI_e mode as functions of the microwave power supplied to the source.

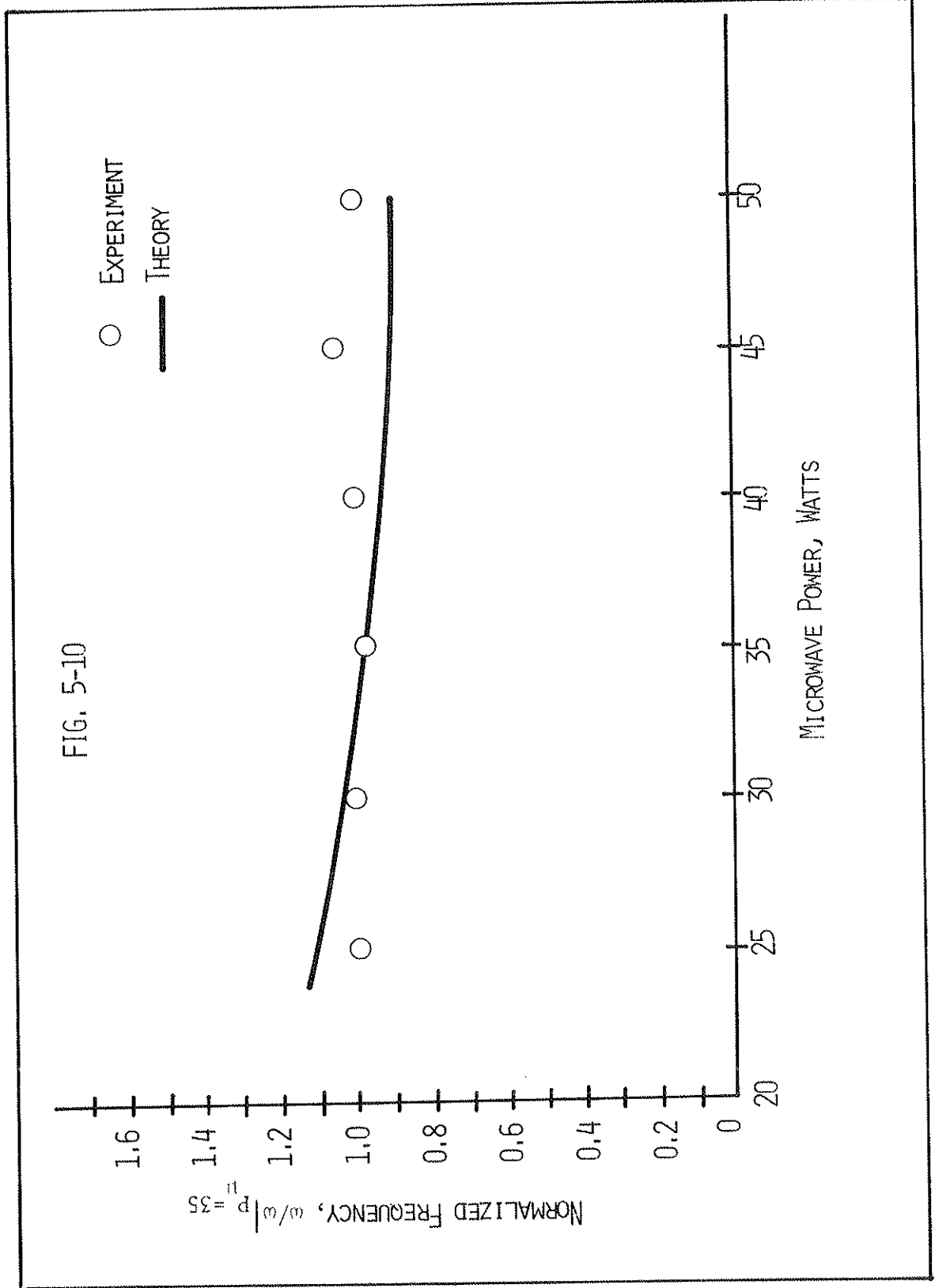


Figure 5-11 Theoretically predicted variation of the growth rate and the experimentally observed change in the fluctuation amplitude of the ∇T_e mode as functions of the microwave power supplied to the source.

FIG. 5-11

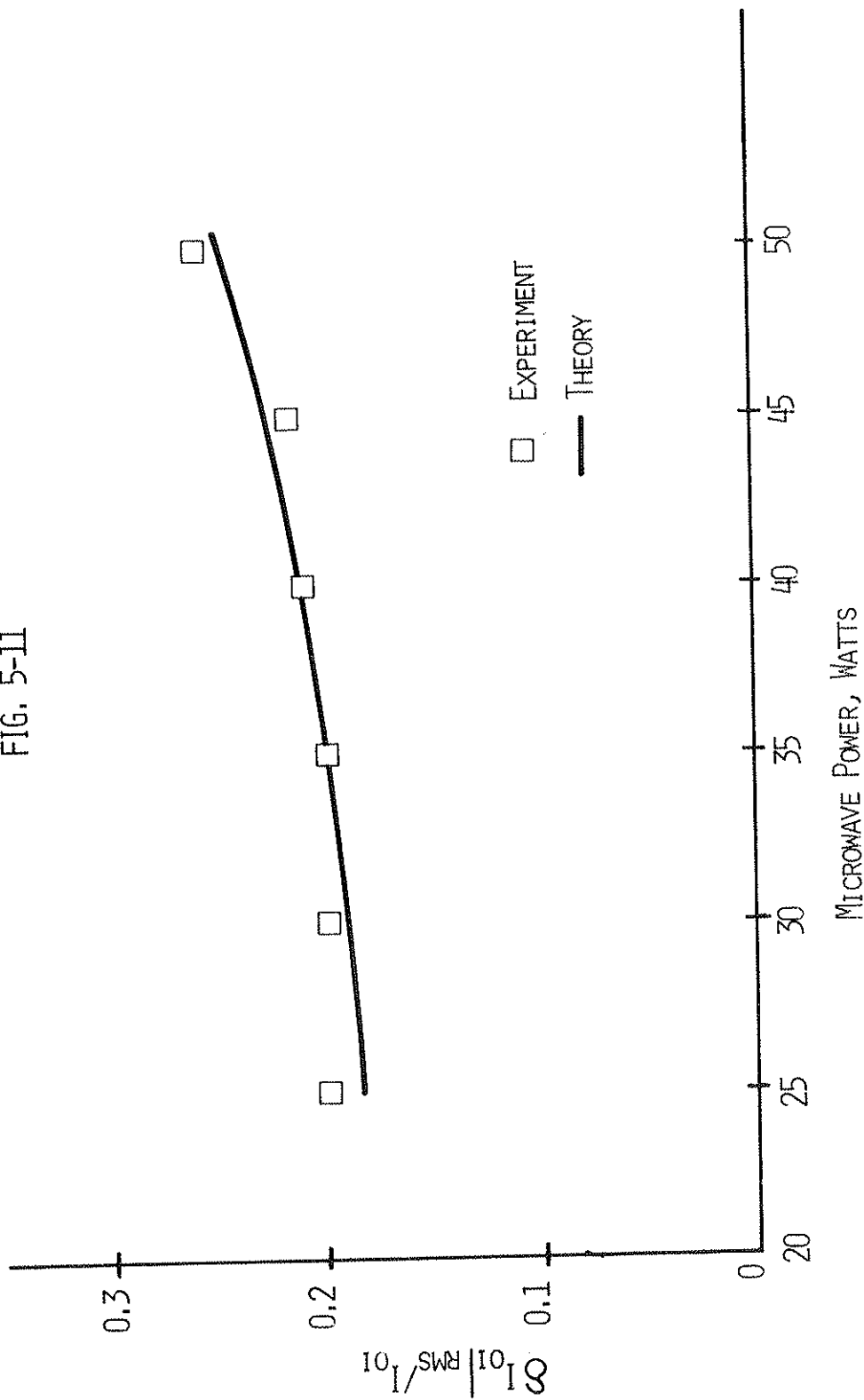


Figure 5-12 Variation of the theoretically predicted and the experimentally observed frequency of the V_{Te} mode as functions of the neutral gas pressure.

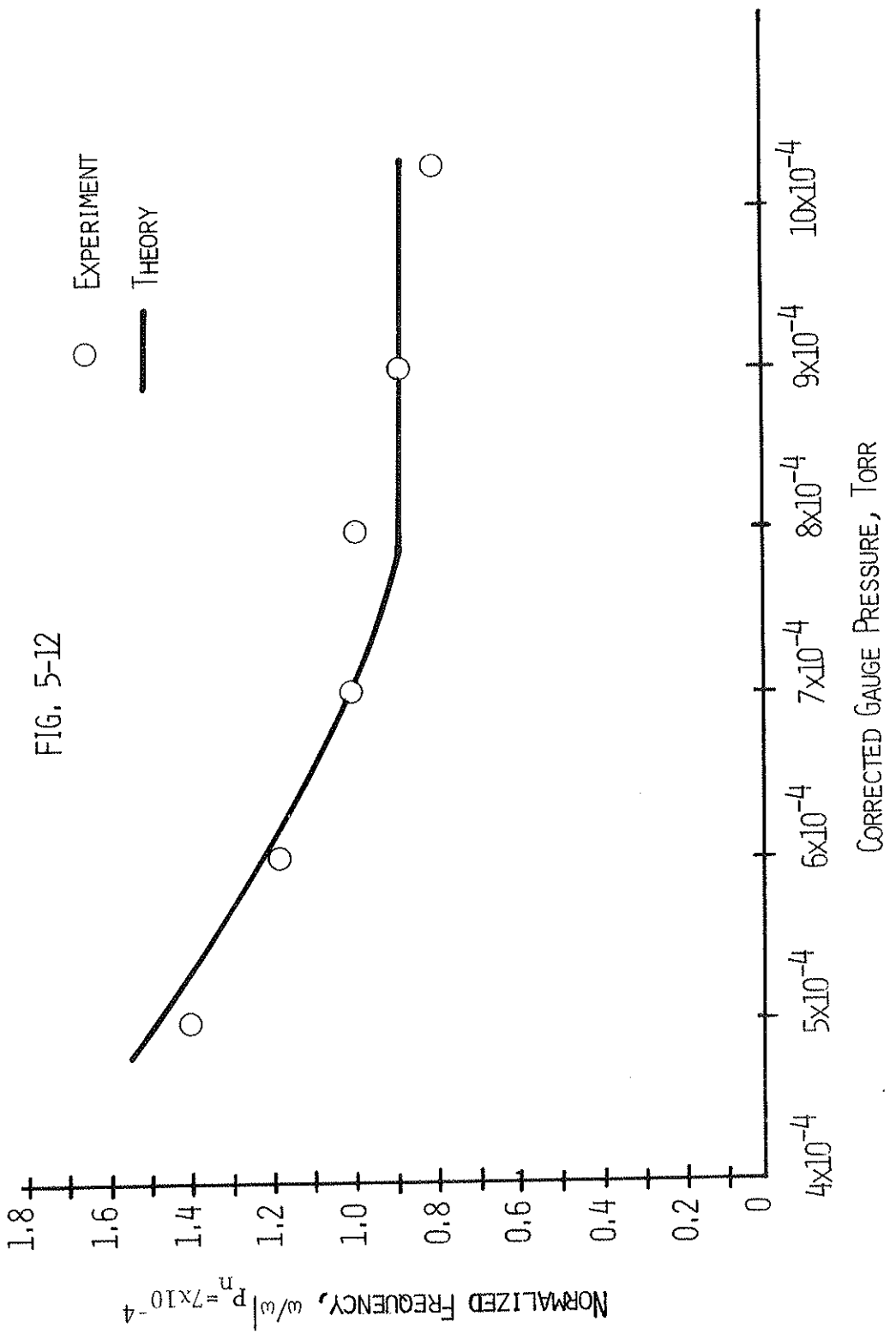
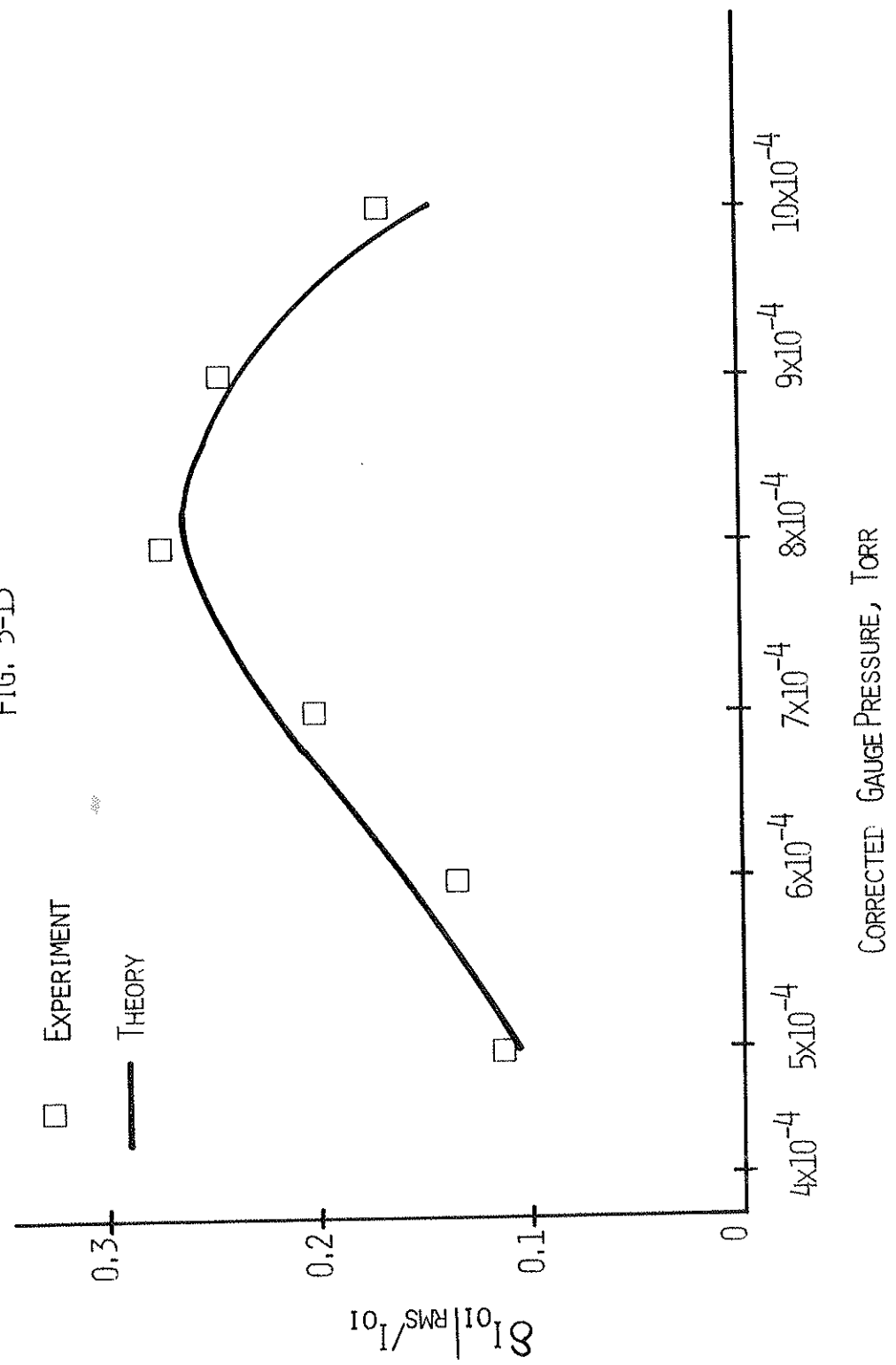


FIG. 5-12

Figure 5-13 The theoretically predicted variation of the growth rate and the observed change in the fluctuation amplitude of the ∇T_e mode as functions of the source gas pressure.

FIG. 5-13



□ EXPERIMENT
— THEORY

observed. The comparison between the predicted growth rate and the changes in the saturated amplitude are shown in Fig. 5-13; qualitative agreement is found in this figure, also.

These experiments were performed when an $m=1$ mode dominated in the plasma. We have since observed the $m=2$ and $m=3$ azimuthal mode numbers of this instability. Whether an $m=1, 2,$ or 3 mode dominates in the plasma appears to be a complex function of the collisionality, mirror ratio, and the average field strength. It has been possible to observe the transition from a mode with one m -number to a mode with a higher m -number as the magnetic field strength was increased. These transitions are marked by the onset of ultra low frequency oscillations, which will be discussed further in the next chapter.

For the initial investigations of the instability the field strength was large enough that the additions to the growth rate of the DTEM due to finite ion Larmor radius effects were much smaller than the driving term due to the electron temperature gradient. Based upon the agreement between theoretical predictions for a DTEM and our experimental observations, therefore, we have identified this mode as a DTEM driven by the electron temperature gradient (∇T_e mode).

We found that at very low magnetic field strengths, where the FLR corrections to the theory are very important, a second new instability appeared in the plasma of the LMM when it was operated in the trapped electron regime. The fluctuations of the ion saturation current and the floating potential associated with the instability were highly

coherent and monochromatic (Fig. 5-14) with $\delta I_{oi}/I_{oi} \approx e\tilde{V}_f/T_e$. The oscillations propagated in the direction of the electron diamagnetic drift with a frequency which was $\sim 1/4$ to $1/2$ of the diamagnetic drift frequency. The mode had an azimuthal mode number, m , equal to 3. Radially, the mode was not well localized (it extended almost all the way out to the wall of the vacuum chamber, Fig. 5-15), and the fluctuations peaked at a radial position where the electron temperature gradient was significantly reduced from its value near the center of the plasma column.

This second new instability was also a full wavelength standing wave parallel to the magnetic field with $\lambda_{||} = 1.2 L$, where L is the length of the plasma column in the experimental region. Similar to the ∇T_e mode, it exhibited nodes at the entrance to the experimental region and in the center of that region (with 180° phase inversion), and did not have a zero fluctuation level at the face of the end mirror. With this parallel wavelength, the parallel phase velocity of the wave was greater than the ion thermal speed, but less than the electron thermal speed: $v_{T,i} \approx 2 \times 10^5$ cm/s $< \omega/k_{||} = 6 \times 10^6$ cm/s $< v_{T,e} \approx 1 \times 10^8$ cm/s. Therefore, this second new instability also appeared to be a drift type of instability.

When the response of the instability to an increase in the mirror ratio (at constant average field strength) was measured, it was found that the saturation amplitude of the instability increased with increasing mirror ratio (Fig. 5-16). This new instability appeared to be very

Figure 5-14 Frequency analysis of the fluctuations in the ion saturation current, unfiltered signal.

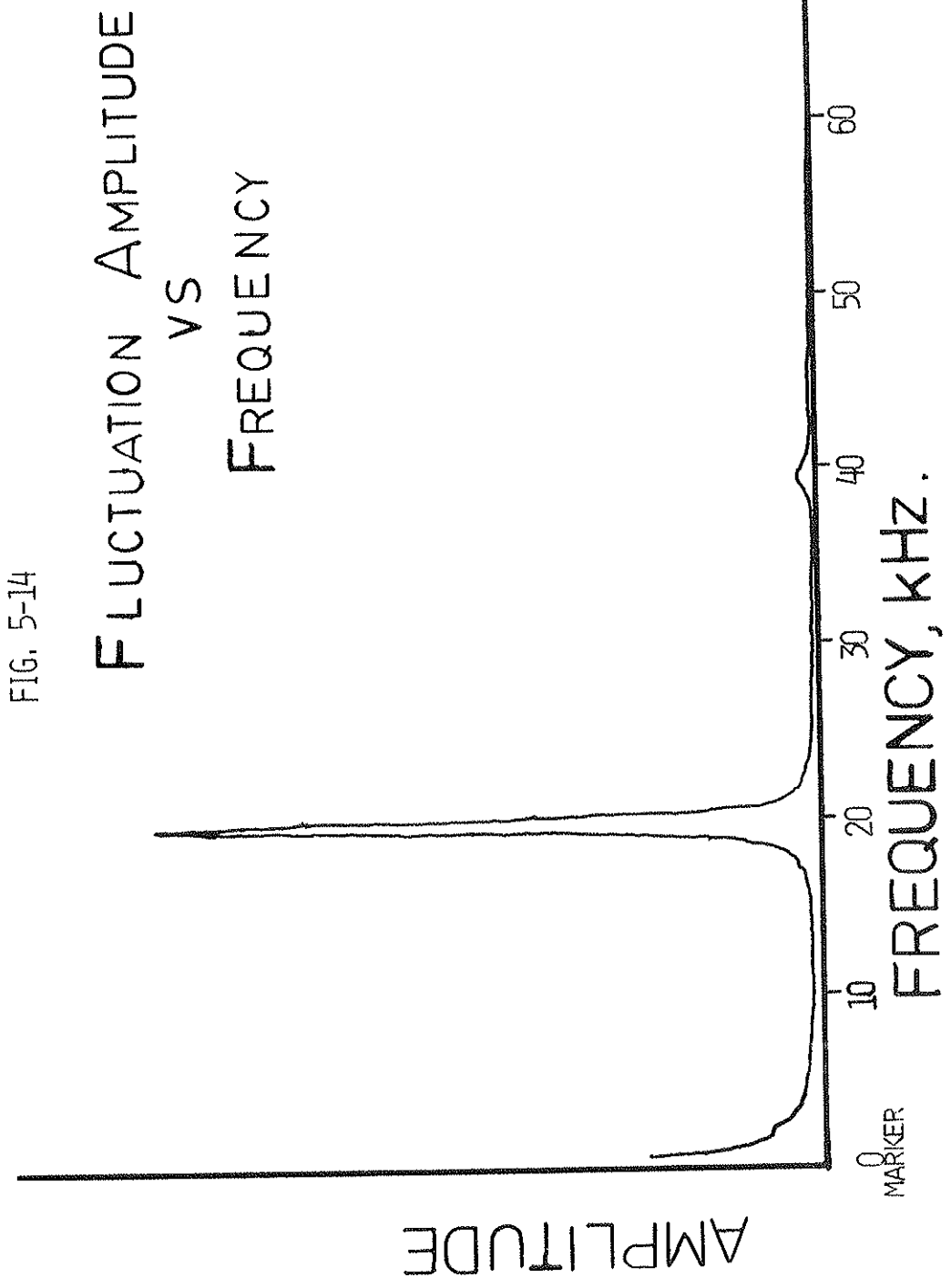


Figure 5-15 Radial localization of the fluctuations in the ion saturation current due to the trapped electron instability driven by finite ion Larmor radius effects (FLR mode). The radial profiles of the density and the electron temperature are also shown.

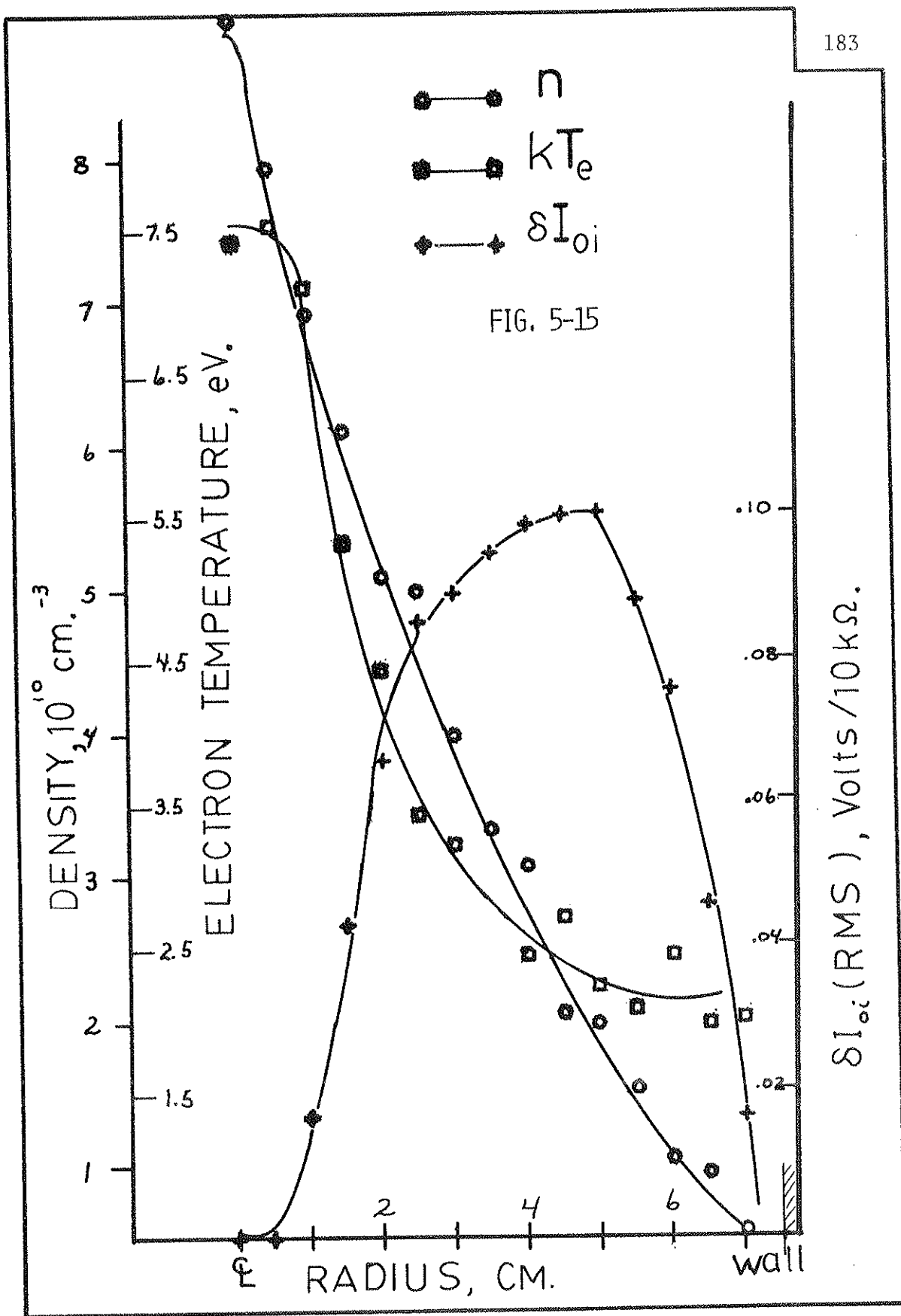
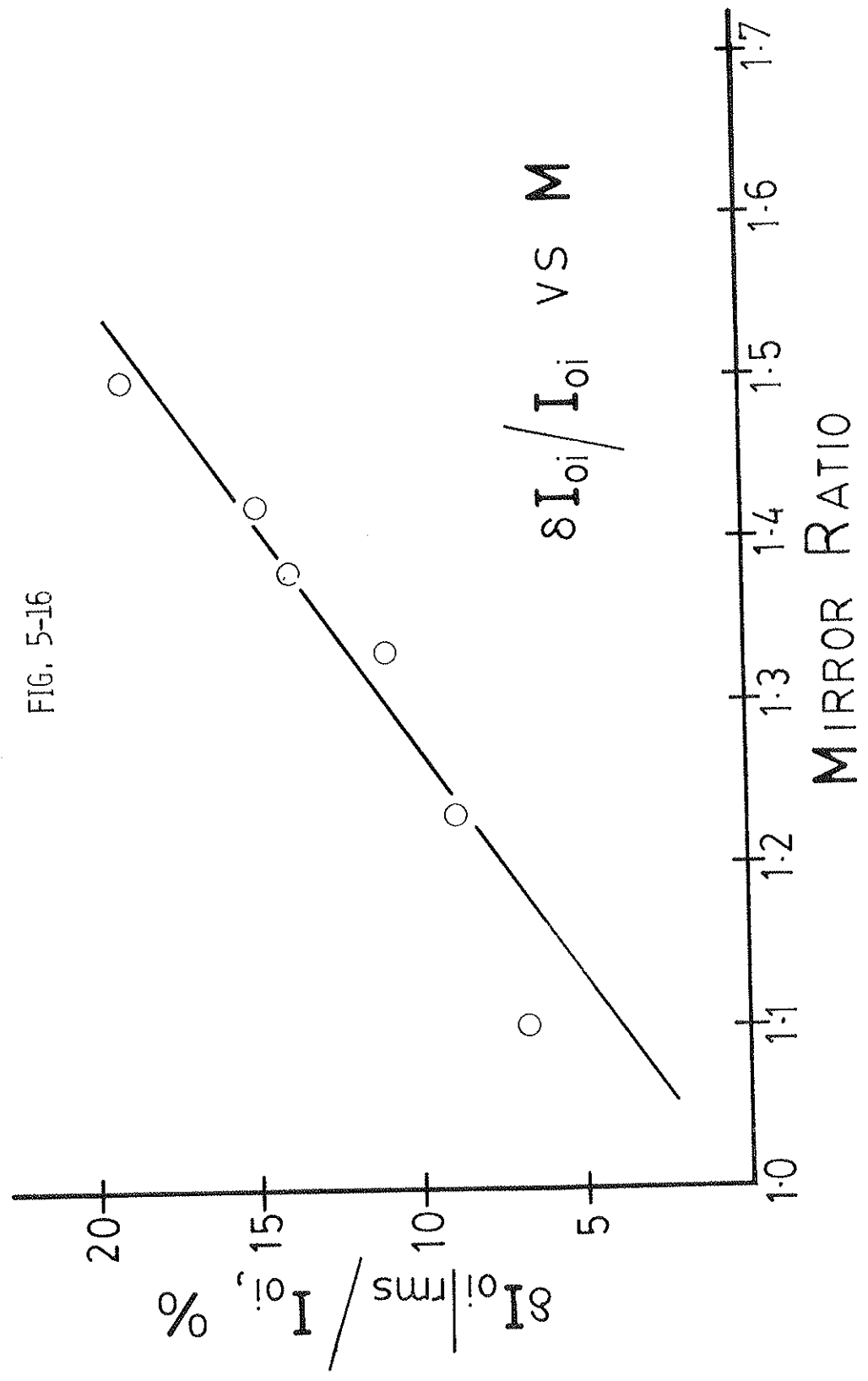


Figure 5-16 Response of the FLR mode to an increase in the magnetic mirror ratio: saturation amplitude versus mirror ratio.

FIG. 5-16



similar to the ∇T_e mode identified earlier except that it was localized at a radial position where the electron temperature gradient was relatively weak. This second new mode, therefore, also appeared to be a DTEM, but driven primarily by the FLR effects (FLR mode).

Theoretically, the amplitude of an FLR mode is very sensitive to the magnetic field strength. In order to check our hypothesis that we were now observing a DTEM driven by FLR effects, we varied the magnetic field strength at a constant mirror ratio and recorded the changes in the amplitude and frequency of the instability. The plasma parameters for each value of $|B|$ were then used to calculate the frequency and the growth rate of a DTEM with the same azimuthal mode number as the mode which we were studying, $m = 3$. The results of this experiment are presented in Fig. 5-17 and 5-18. The agreement between the theory and the experiment shown in Fig. 5-17 is both qualitative and quantitative for $B \gtrsim 100$ G, e.g. for $|B| = 250$ G the predicted frequency was 22kHz and the observed frequency was 23.5 kHz. Since the difference between the two values lies within the range of experimental errors, the data in Fig. 5-17 were normalized to give agreement for this value of $|B|$. As shown in Fig. 5-18 the theory correctly predicts the change in the instability amplitude over the entire range of values for $|B|$ if one assumes a direct relationship between the mode's amplitude and its growth rate.

For $|B| < 100$ G, however, the theory and the experiment no longer agree in Fig. 5-17. This may be due to a breakdown in the theory at

Figure 5-17 Theoretically predicted and experimentally observed changes in the frequency of the FLR mode as a function of the magnetic field strength.

FIG. 5-17

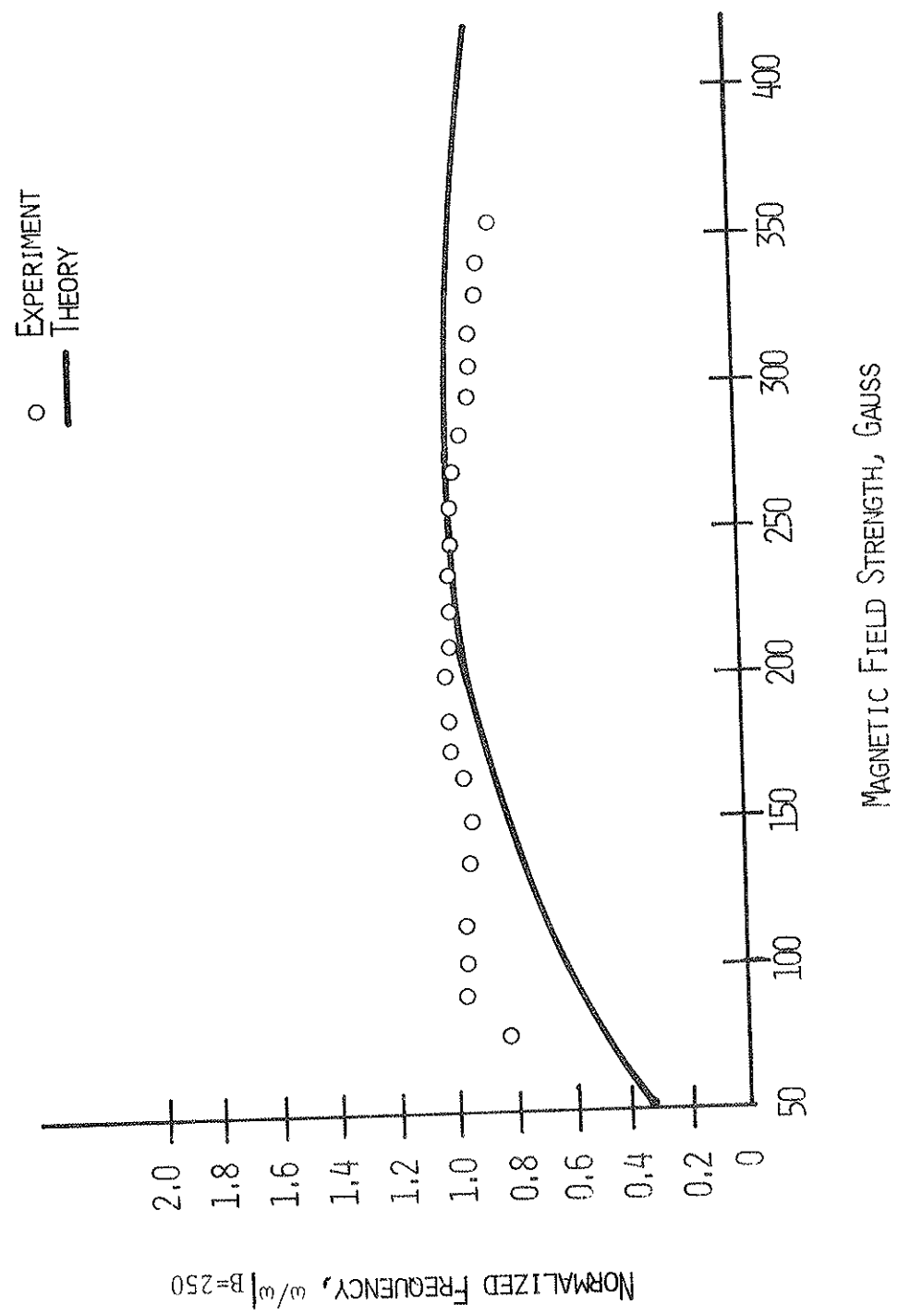


Figure 5-18 Theoretically predicted variation of the growth rate and the experimentally measured change in the saturation amplitude of the FLR mode as functions of the magnetic field strength.

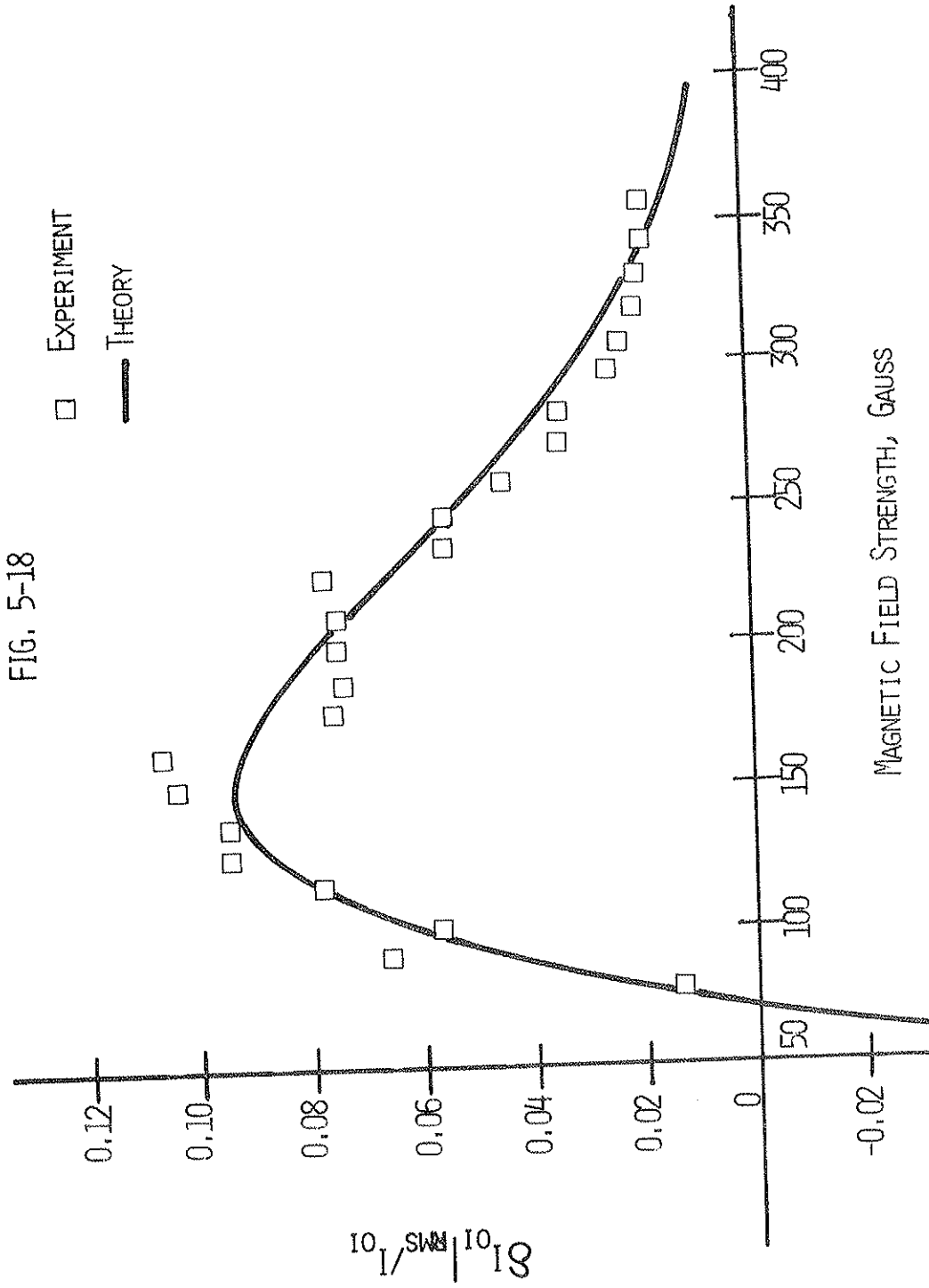


FIG. 5-18

this point because the FLR parameter, b , is $\gtrsim 0.1$ for $|B| \lesssim 100$ G so that it is necessary to retain higher order terms in the expansion $S_o(b) \approx 1 - b + \dots$, which is used in the theory. It is not clear at this time why a similar departure from the theoretical values was not observed for $|B| < 100$ G in Fig. 5-18.

Based upon the basic drift wave nature of this second new instability and the fact that its amplitude increases with increasing mirror ratio and is a strong and predictable function of the magnetic field strength, we have identified this mode as a DTEM driven by FLR effects (FLR mode).

We have observed azimuthal mode numbers $m=1, 2, 3,$ and 4 of the FLR mode. As in the case of the ∇T_e mode, the determination of which m -number dominates in the plasma appears to be a complex function of the collisionality, mirror ratio, and average field strength. We have observed the transition from a mode with one m -number to another mode with a higher m -number as the magnetic field strength was increased. These transitions are marked by the excitation of ultra low frequency oscillations which are the subject of Chapter 6.

It should be noted that both the mode which we have labeled the ∇T_e mode and the one which we have labeled the FLR mode are the same instability: the DTEM. Since the two modes are localized in regions of different plasma parameters so that the driving terms for the two modes are different, it was possible to label the modes in this manner to facilitate bookkeeping. In general, however, it is necessary to retain

Figure 5-19 Frequency analysis of the fluctuations in the ion saturation current measured when the plasma was unstable to both the ∇T_e and FLR trapped electron modes, unfiltered signal.

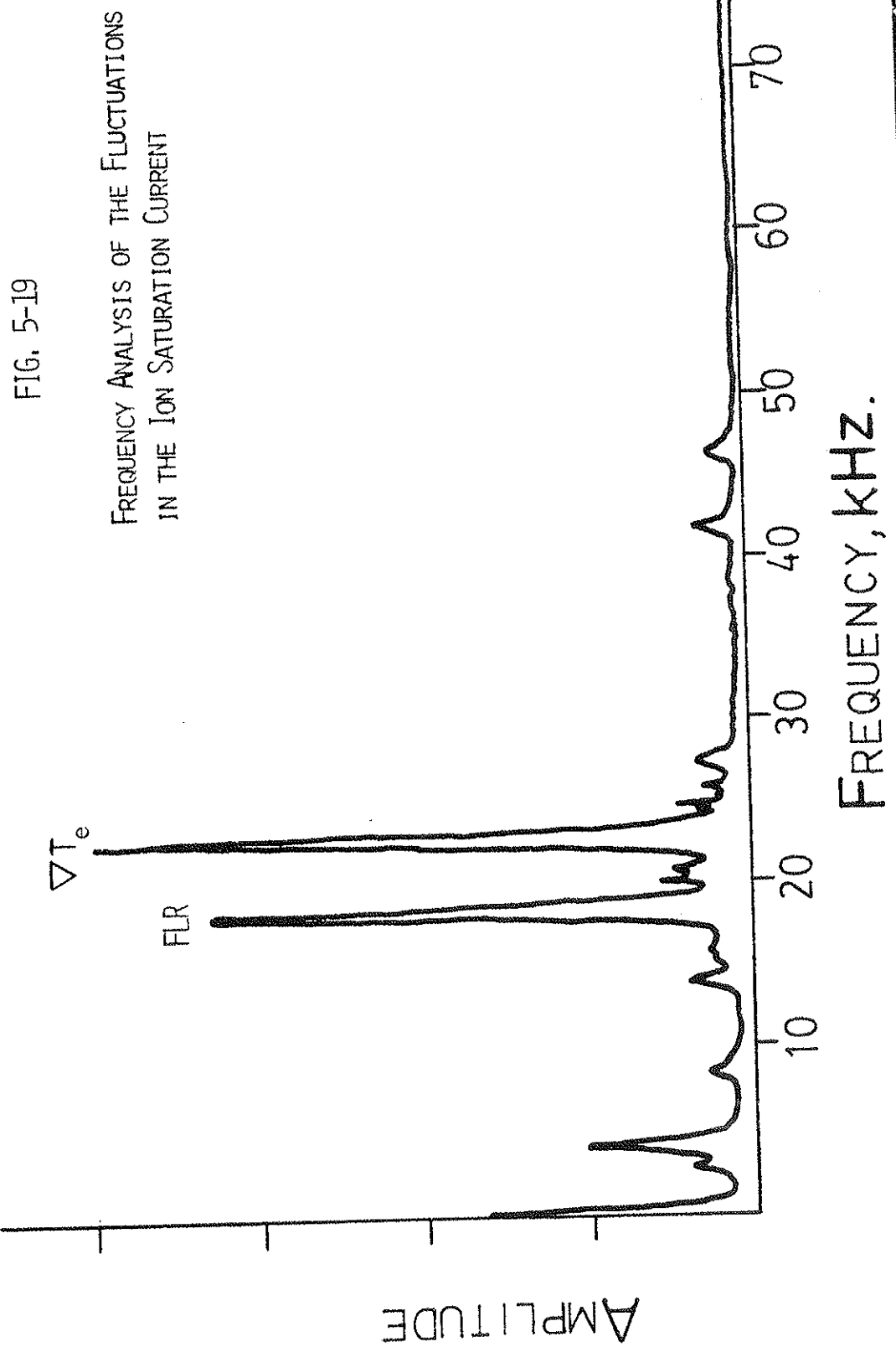
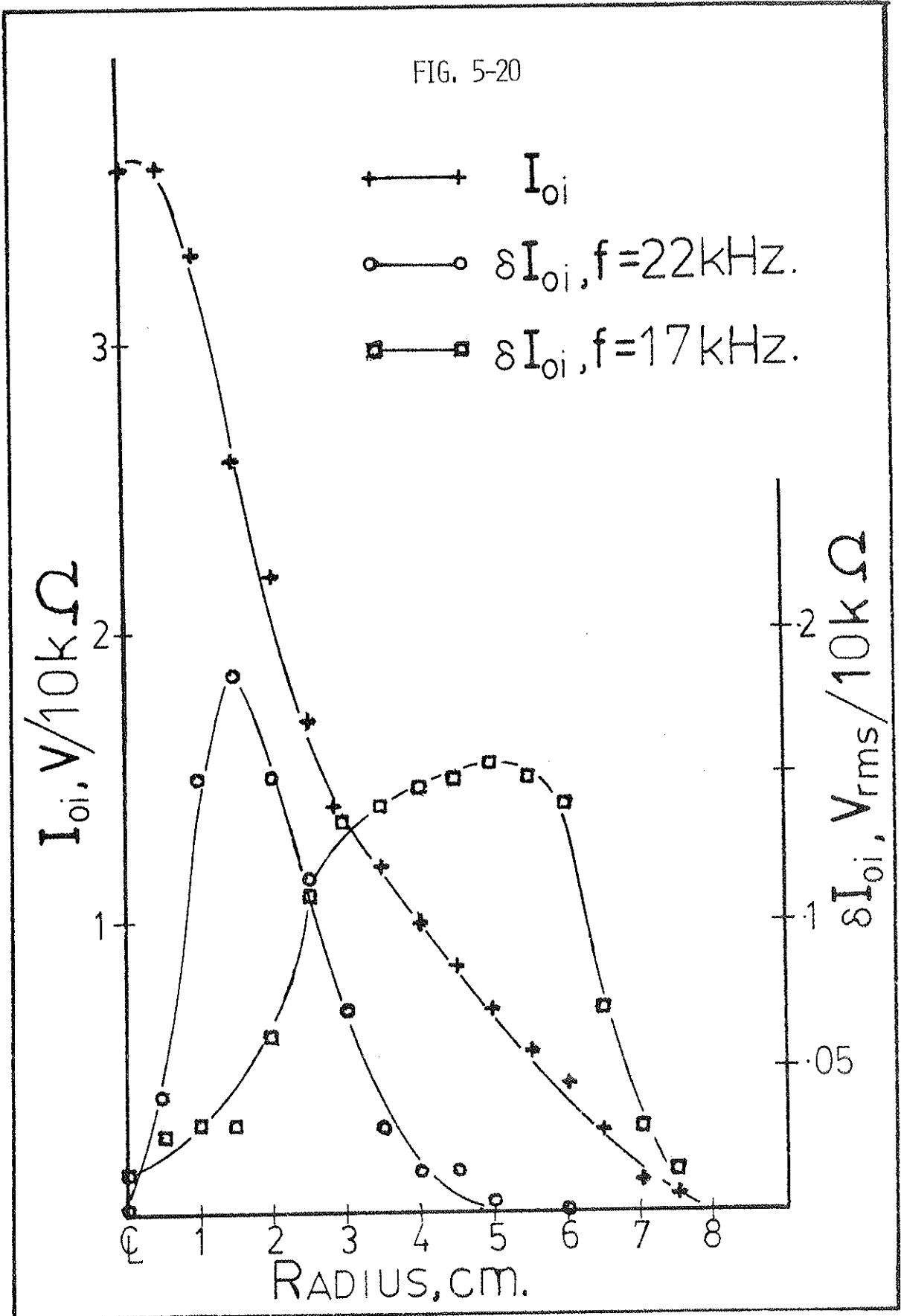


FIG. 5-19

FREQUENCY ANALYSIS OF THE FLUCTUATIONS
IN THE ION SATURATION CURRENT

Figure 5-20 Radial localization of the VT_e mode and the FLR mode measured when the plasma was unstable to both modes simultaneously.



the FLR corrections to the theory to correctly predict the behavior of the ∇T_e mode; and, conversely, the ∇T_e terms must be included to correctly describe the FLR mode.

For values of the magnetic field strength between those where the ∇T_e mode is present alone and those where the FLR mode is present alone, the plasma can be unstable to both modes simultaneously (Fig. 5-19). In this intermediate field strength regime the ∇T_e mode is again localized in the region of strong electron temperature gradient, and the FLR mode has a broad radial extent in the region of weak temperature gradient (Fig. 5-20). The two modes typically appear at different frequencies, but the frequency of each mode is accurately predicted by the dispersion relation if the local values of the plasma parameters are used in the calculation for each mode. When the two trapped electron modes are present at the same time it has been noted that the fluctuations due to each mode are uncorrelated one with the other. It has also been noted that the two DTEM's (∇T_e & FLR) do not appear together with the same m-number. The most commonly observed phenomenon is an $m=1$, ∇T_e mode with an $m=3$, FLR mode.

In Figs. 5-21 through 5-24 the growth rate as a function of the azimuthal mode number is plotted for plasma parameters which are typical of the following regimes: Fig. 5-21, ∇T_e mode alone; Fig. 5-22, transition regime parameters for the region where the ∇T_e mode is localized; Fig. 5-23, transition regime parameters for the region where the FLR mode is localized; and Fig. 5-24, FLR mode alone. For the

parameters of each of the four figures only one mode with a unique azimuthal mode number was unstable in the region of the plasma described by those parameters; and yet, the theory predicts many linearly unstable modes at each location. This may be interpreted as additional evidence that the mode competition which we believe to be a major cause of the problems which we have experienced while trying to perform feedback stabilization experiments is indeed occurring.

As noted earlier in this chapter, we have observed the plasma to be simultaneously unstable to more than one m -number of the same instability. When this occurs the plasma exhibits what appears to be another kind of mode-mode interaction: the excitation of ultra low frequency oscillations. We now turn our attention to this phenomenon in Chapter 6.

Figure 5-21 Growth rate versus azimuthal mode number for the trapped electron instability. The dispersion relation was evaluated using plasma parameters typical of those for which the V_{Te} mode is the only unstable mode.

FIG. 5-21

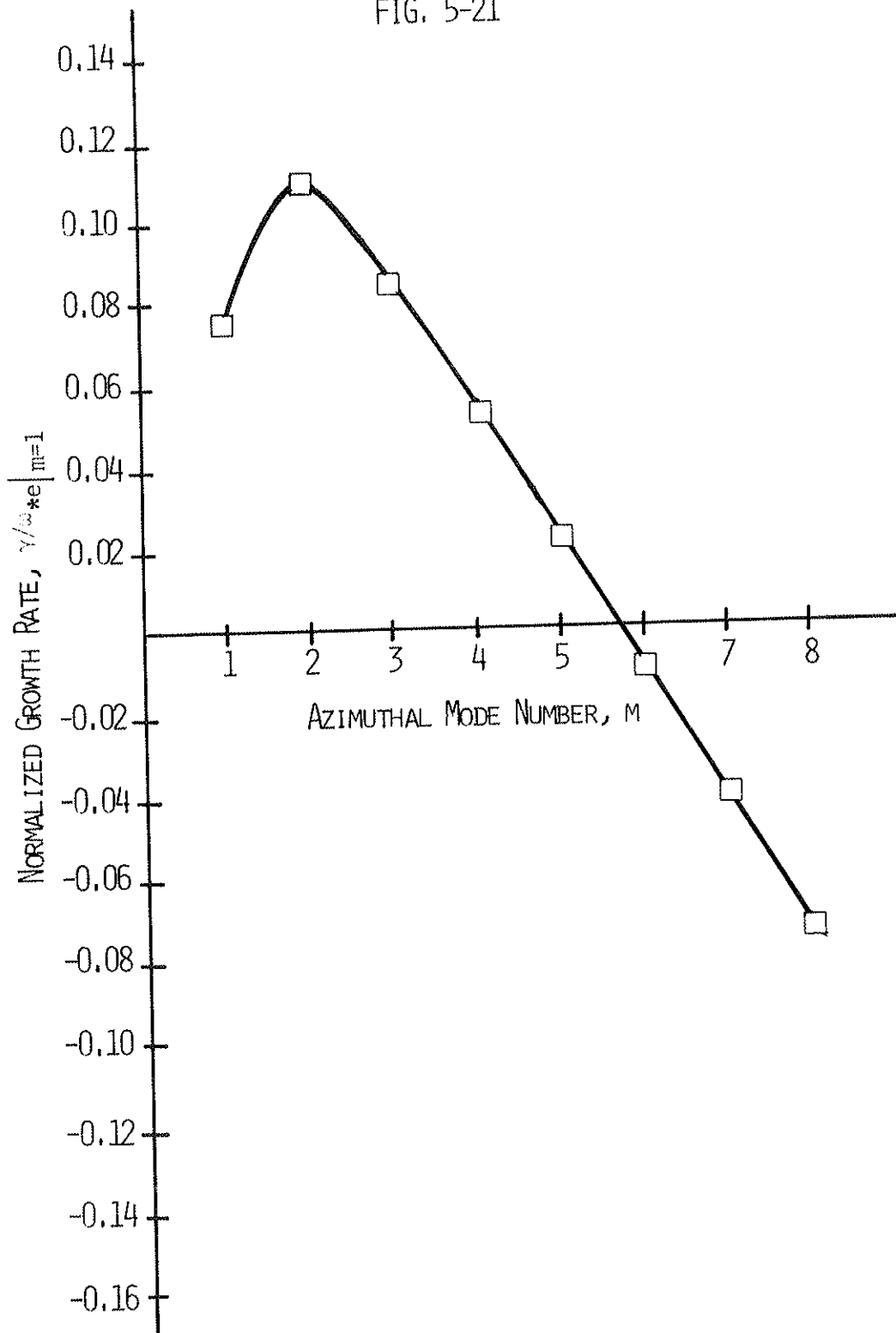


Figure 5-22 Growth rate versus azimuthal mode number for the trapped electron instability. The dispersion relation was evaluated using plasma parameters which are typical of those at the radial position where the ∇T_e mode has maximum amplitude in the transition field strength regime.

FIG. 5-22

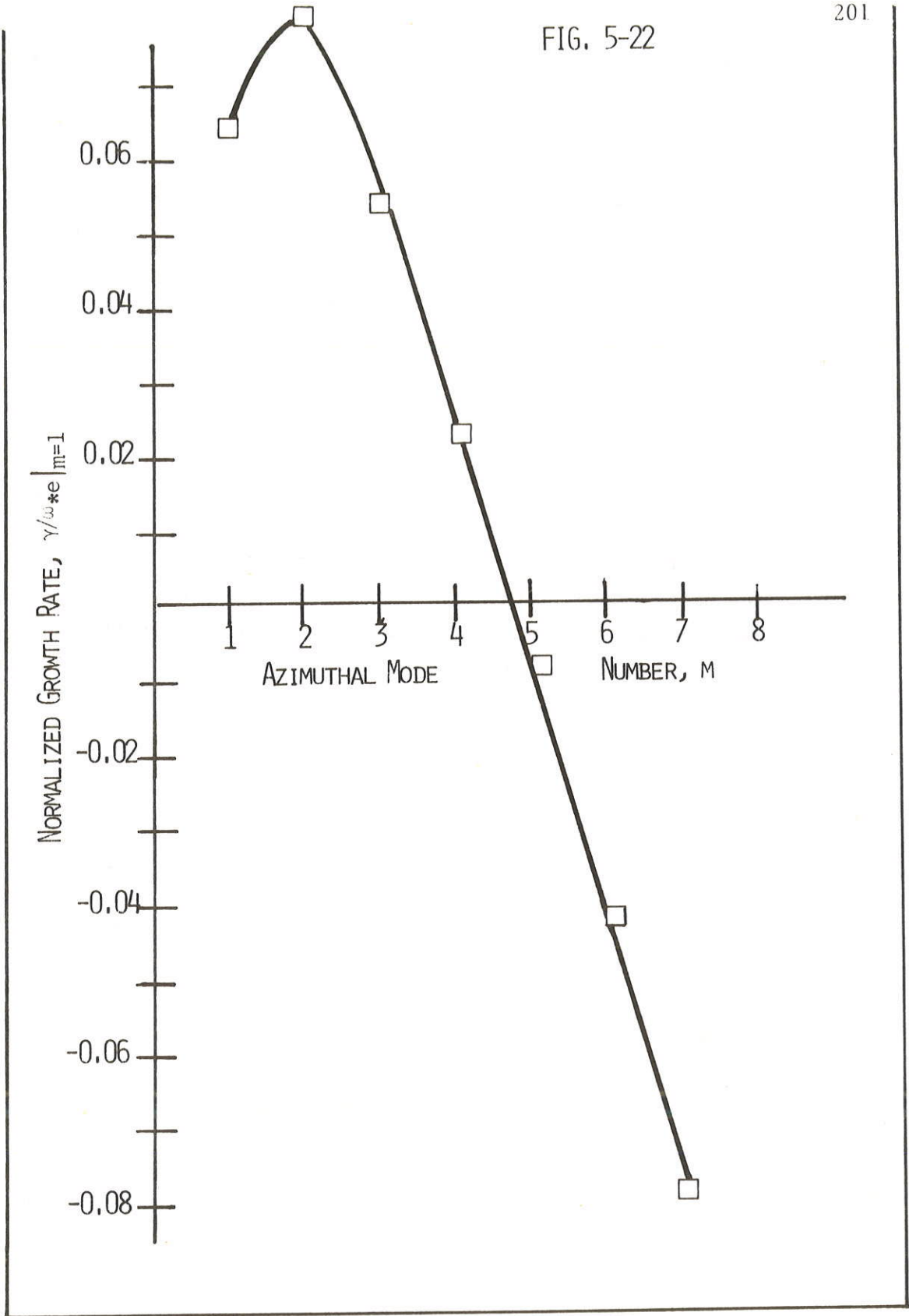


Figure 5-23 Growth rate versus azimuthal mode number for the trapped electron instability. The dispersion relation was evaluated using plasma parameters which are typical of those at the radial position where the FLR mode has maximum amplitude in the transition field strength regime.

FIG. 5-23

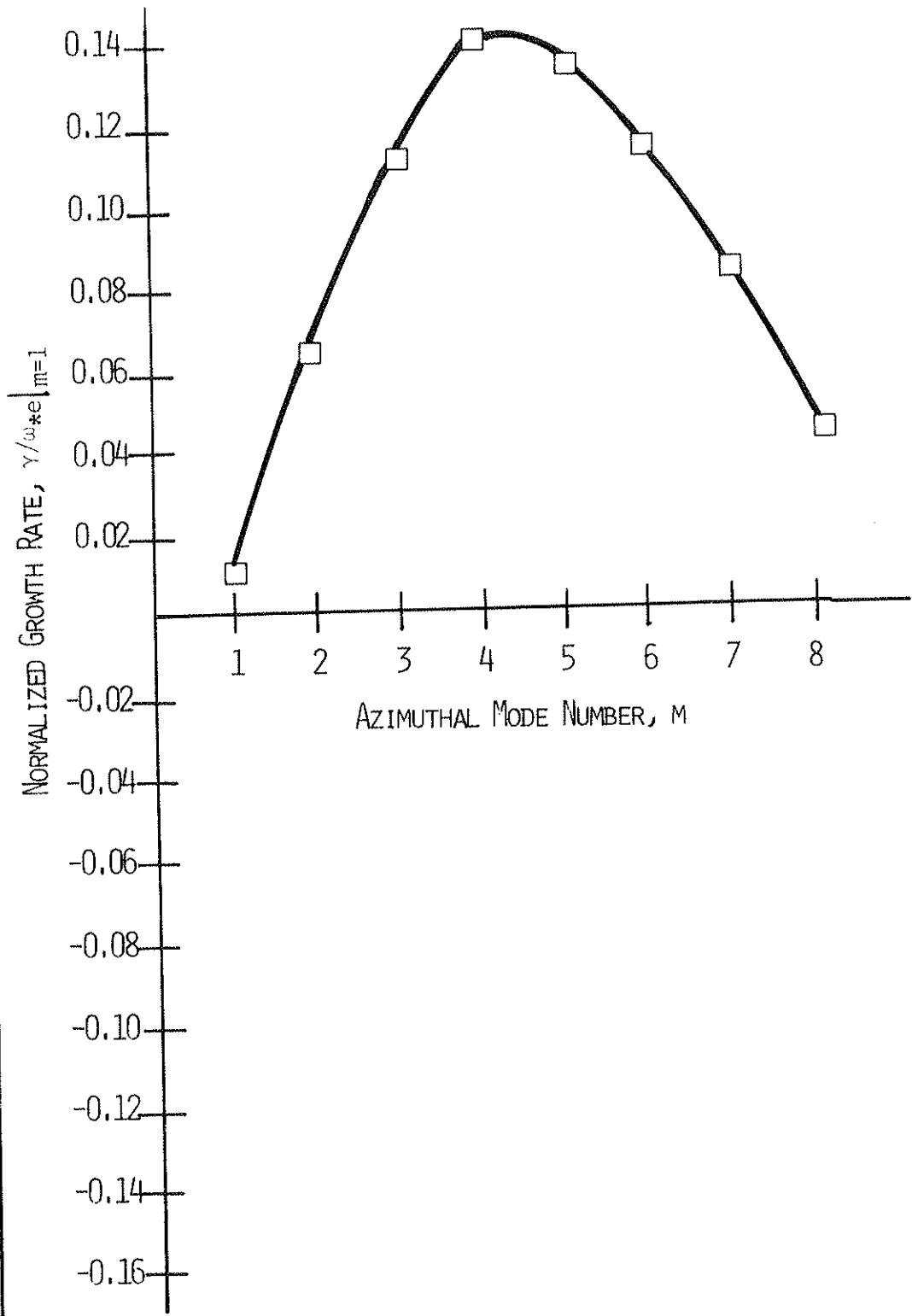
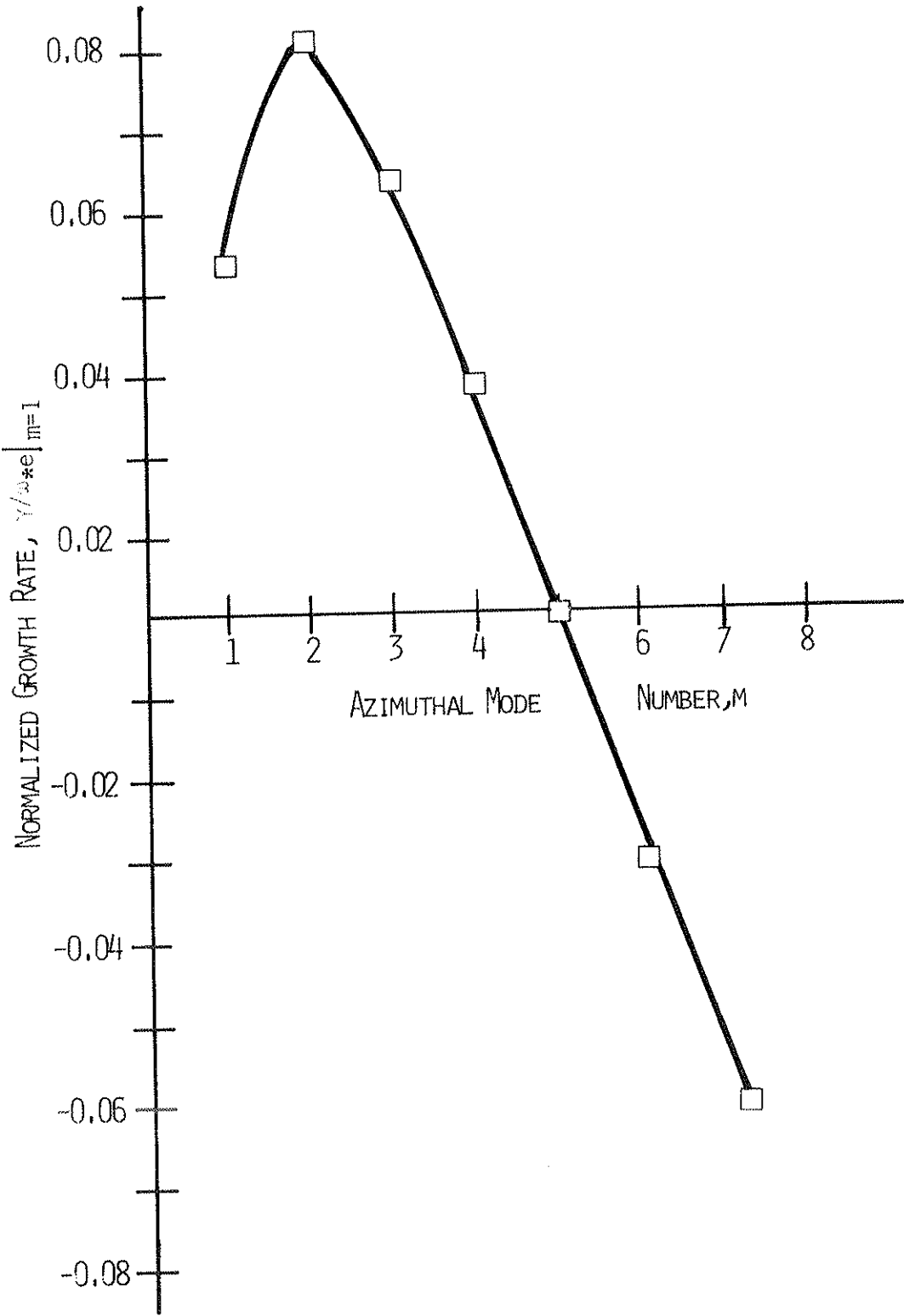


Figure 5-24 Growth rate versus azimuthal mode number for the trapped electron instability. The dispersion relation was evaluated using plasma parameters which are typical of those for which the FLR mode is the only unstable mode.

FIG. 5-24



References for Chapter 5

1. G. Schmidt, Physics of High Temperature Plasmas, Academic Press, New York (1966), p. 293
2. P. L. Bhatnagar, E. P. Gross, and M. Krook, *Physical Rev.*, 94, 511 (1954)
3. J. C. Adam, G. Laval, and R. Pellat, *Nuc. Fusion*, 13, 47 (1973)
4. W. Horton, Jr., et al. in *Plasma Physics and Controlled Nuclear Fusion Research, Proceedings of the Fifth International Conference*, Tokyo (IAEA, Vienna, 1974), p. 541
5. B. B. Kadomstev and O. P. Pogutse, *Soviet Physics-Doklady*, 14, 470 (1969)
6. C. S. Liu, M. N. Rosenbluth, and W. M. Tang, *Phys. of Fluids*, 19, 1040 (1976)
7. S. I. Braginskii, Reviews of Plasma Physics, (Consultants Bureau, New York, 1965), Vol. 1, p. 214
8. A. A. Rukhadze and V. P. Silin, *Soviet Physics-USPEKHI*, 11, 659 (1969)
9. P. Deschamps, R. Gravier, C. Renaud, and A. Samain, *Phys. Rev. Lett.*, 31, 1457 (1973)
10. F. F. Chen, *J. Nucl. Energy, Pt. C*, 7, 399 (1965)
11. R. K. Richards and G. A. Emmert, *Nuc. Fusion*, 17, 205 (1977)

CHAPTER 6

NEAR ZERO FREQUENCY OSCILLATIONS

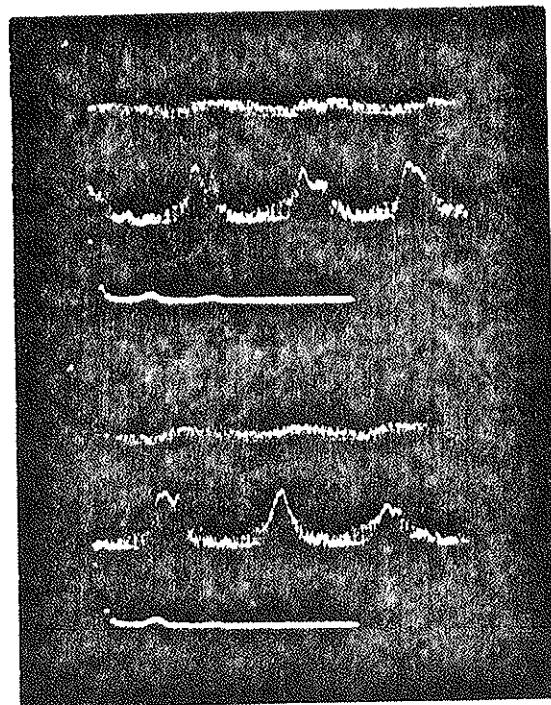
While operating in the trapped electron regime it was noted that the plasma would sometimes break into ultra low frequency (ULF) oscillations, $f \approx 100$ Hz, as the plasma parameters were varied. Initial investigations of these oscillations centered around attempts to correlate them with ripples in the power supply currents, variations in the microwave power, and similar phenomena. No such correlations were found. Indeed, these investigations revealed that the ULF oscillations were confined to the multimirror region (Fig. 6-1) except in cases of extremely large scale ULF oscillations, in which case a perturbation of the plasma in the source could be detected. (The data presented in this chapter were taken only for the case of oscillations which did not perturb the source.) It was also discovered that the frequency of the ULF oscillations was weakly dependent upon the source gas pressure and the magnetic field strength. Based upon these observations it appeared that the oscillations were actual plasma phenomena so they were subsequently investigated as such.

Careful examination of the available data on the ULF oscillations revealed that they were present only in the parameter range in which two trapped electron instabilities were unstable at the same time. The two trapped electron instabilities can be either two ∇T_e modes or two FLR modes with different azimuthal mode numbers, m , or a ∇T_e mode and

Figure 6-1 ULF oscillations of the ion saturation current as measured by Langmuir probes in the source region (top trace) and in the experimental region (middle trace). The bottom trace is a frequency analysis of the signal from the probe in the source region (top trace).

The two sets of trace (top three and bottom three traces) were recorded a few minutes apart.

FIG. 6-1



δI_{OI}

0.50/cm

2 MS/CM

FREQUENCY ANALYSIS
100 Hz/cm

a FLR mode localized on different radial surfaces (Fig. 6-2 and 6-3). The characteristics of the excited ULF oscillations appear to be a function of the type of trapped electron modes present. More will be said about this point later in the chapter.

The waveform of the ULF fluctuations is very nonlinear, but may be quite coherent. In Fig. 6-4 the frequency spectrum of the floating potential oscillations and the oscillations in the ion saturation current at the same spatial location are shown. The high degree of nonlinearity is apparent in the spectrum of fluctuations of the ion saturation current where the fundamental and three harmonics are clearly visible. $\delta I_{oi}/I_{oi}$ evaluated for the fundamental is 13% and the total, summing over the harmonics, is 21%. It is a little more difficult to evaluate the oscillations of the floating potential since we cannot resolve the contribution due to electron temperature fluctuations. Recall that $V_f = V_s - |\alpha| kT_e$ where $|\alpha| = 4.45$ for a Helium plasma so $\delta V_f = \delta V_s - 4.45 \delta kT_e \cos \theta$ where θ is the phase angle between the oscillations of the space potential and the electron temperature. This coupling of space potential oscillations and electron temperature fluctuations may explain the fact that the amplitude of the first harmonic is equal to that of the fundamental (the peak at 120 Hz is pick-up from a full wave rectified 60 Hz power supply). The value of $e \frac{\tilde{V}_f}{kT_e}$ is 5% for the fundamental and 10% for the fundamental plus the first harmonic.

When the ULF oscillations are coherent, definitive measurements of

Figure 6-2 Frequency analysis of the fluctuations in the ion saturation current measured when the plasma was unstable to both the ∇T_e mode and the FLR mode: unfiltered signal.

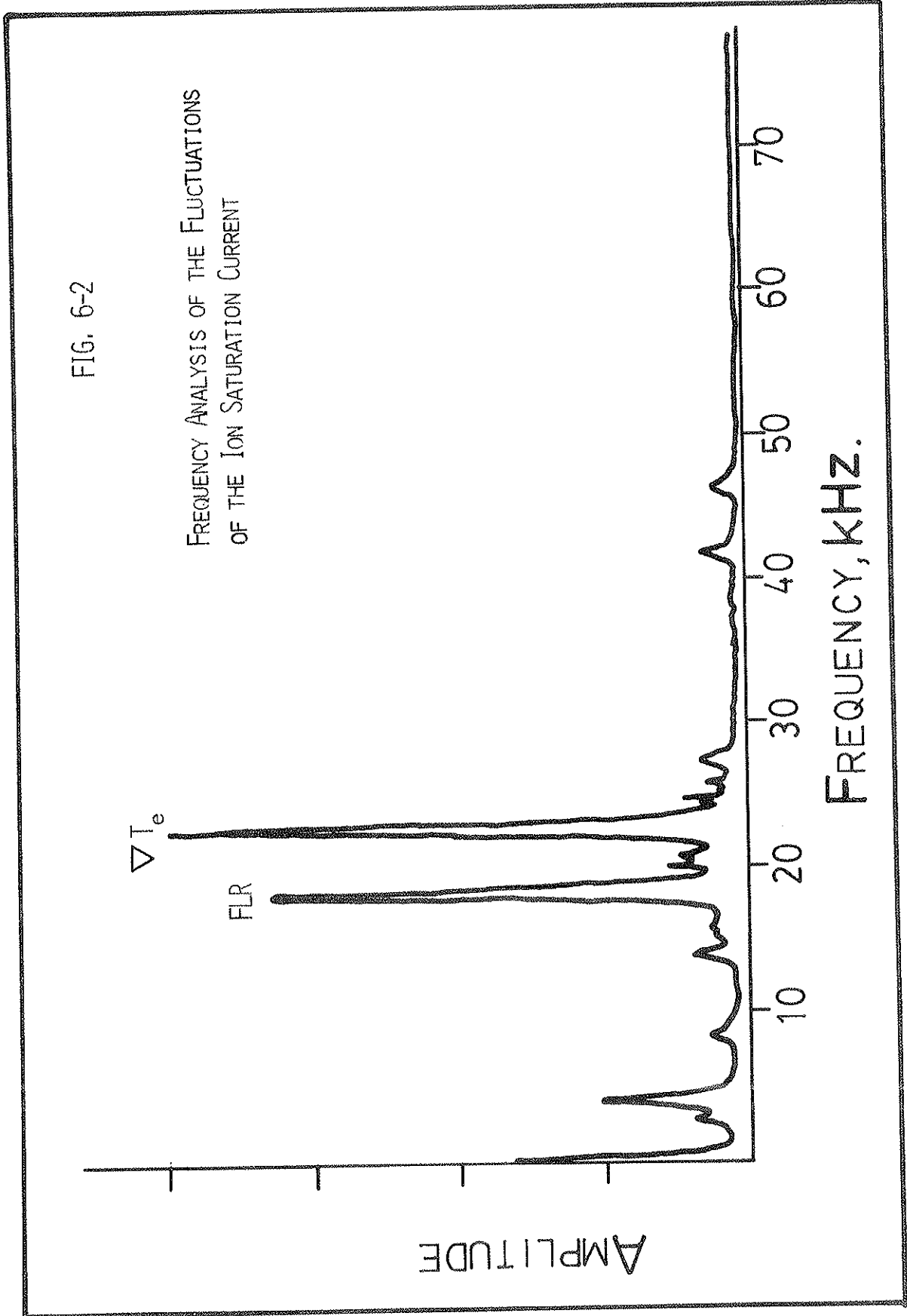


FIG. 6-2
FREQUENCY ANALYSIS OF THE FLUCTUATIONS
OF THE ION SATURATION CURRENT

AMPLITUDE

FREQUENCY, KHZ.

Figure 6-3 Radial localization of the VI_e mode and the FLR mode measured when the plasma was unstable to both modes simultaneously.

FIG. 6-3

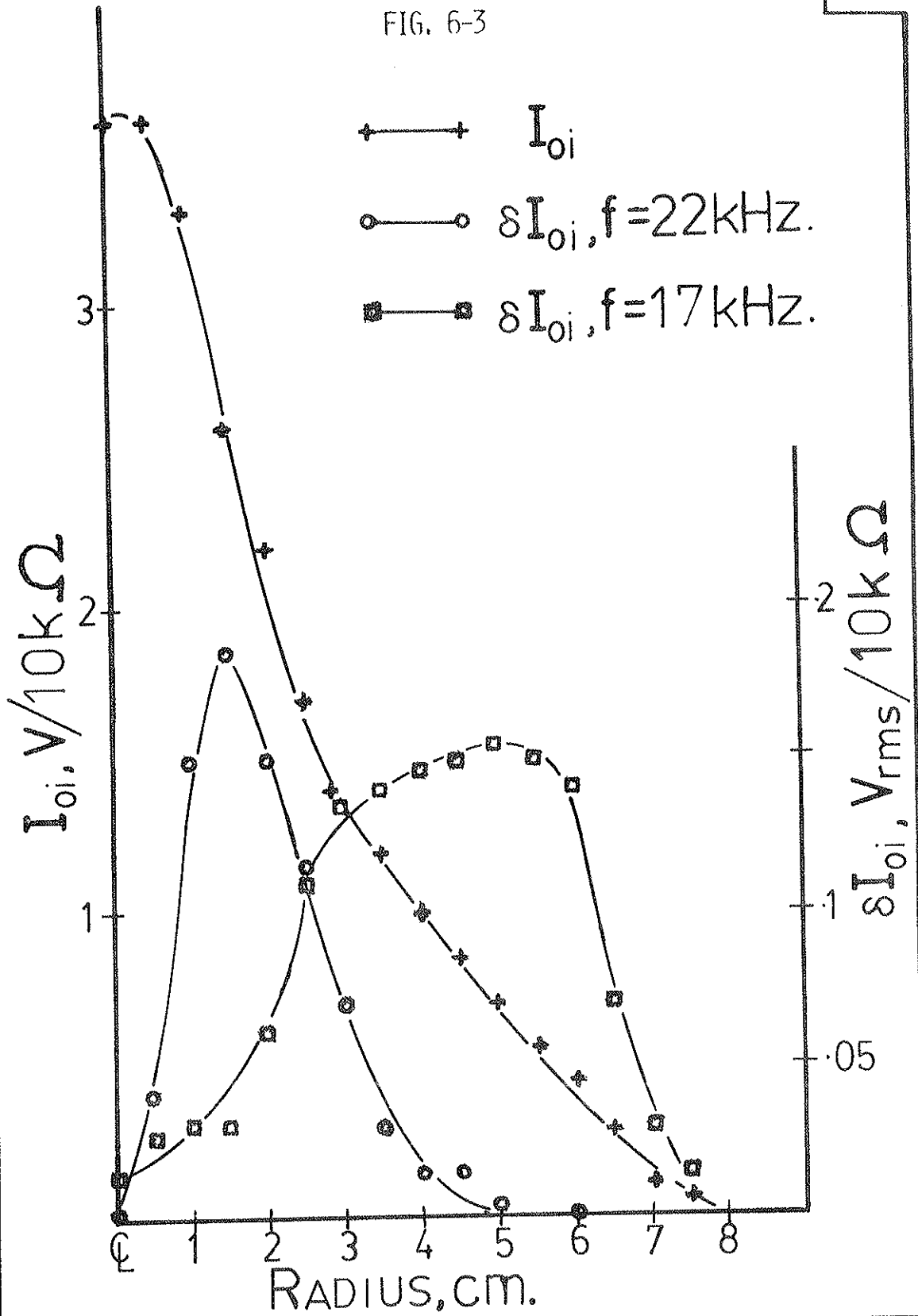
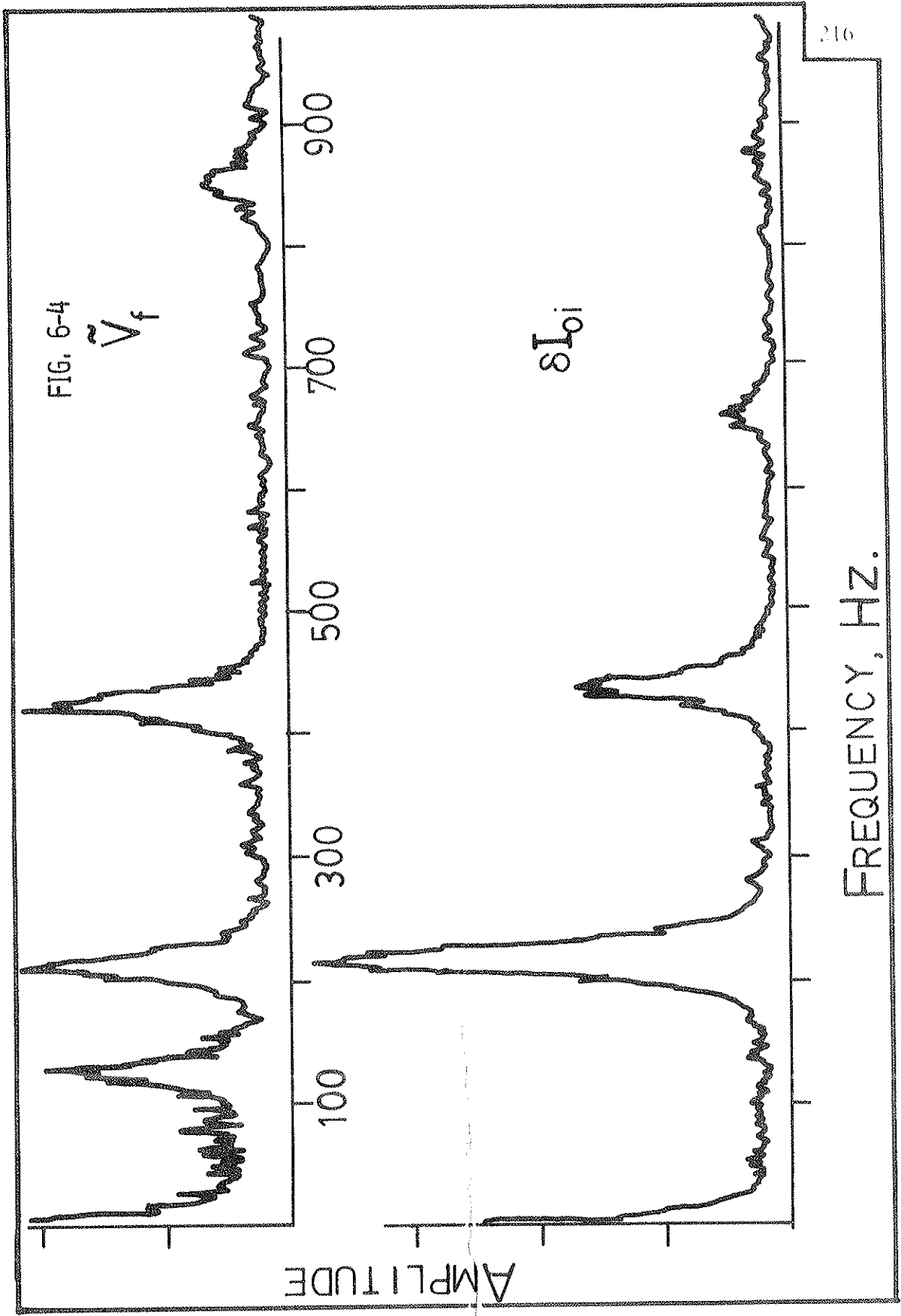


Figure 6-4 Frequency analysis of the fluctuations in the floating potential (top) and the ion saturation current (bottom) measured at the same radial position. (The peak at 120 Hz in the spectrum of the floating potential oscillations is due to pick up.)

The total fluctuation amplitudes (summing over harmonics) are $\delta I_{oi}/I_{oi} \approx 21\%$ and $e\tilde{V}_f/T_e = 10\%$.

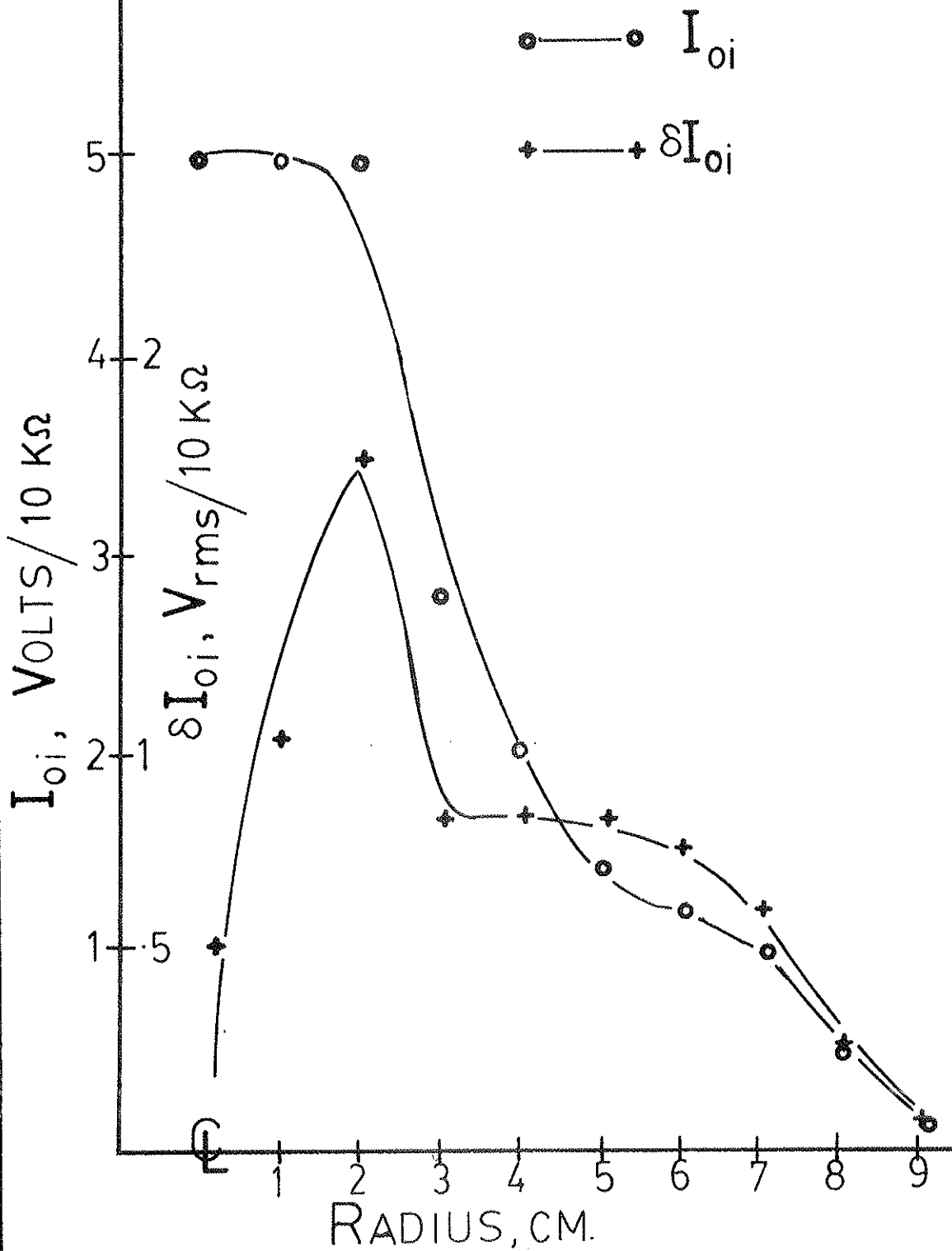


the azimuthal mode number, direction of propagation, radial extent, and parallel wavelength can be made. We have found that the azimuthal waveforms are nonlinear and, therefore, difficult to assign a single azimuthal mode number (Fig. 6-5). To correctly describe the waveform, many mode numbers--both odd and even--would be required. However, in a rudimentary sense we can describe the waveforms which we have observed as being either $m=1$ or $m=2$; i.e. the waveforms, while not true sinusoids, exhibit the correct phase relationships between probes separated by 90° and 180° in azimuth from a fixed reference probe. These oscillations propagate in the direction of the electron diamagnetic drift, but at a frequency far less than that corresponding to either the diamagnetic frequency ($f \approx 30$ kHz) or the electron magnetic curvature drift frequency ($f \approx 5$ kHz). Radially, the ULF oscillations extend from the centerline of the plasma column to the walls of the device (Fig. 6-6). Finally, the parallel wavelength appears to be infinite, or at least many times the length of the machine. This is in sharp contrast to the trapped electron modes which are one full wavelength standing waves parallel to the magnetic field.

The method of excitation of the ULF oscillations can be clearly seen in Fig. 6-7. In this figure the fluctuations of the ion saturation current detected by two Langmuir probes are displayed as the magnetic field strength is continuously increased from 154 G to 340 G at a fixed mirror ratio of 1.38. The probes were 180° apart in azimuth and on slightly different radial surfaces. The signals in Fig. 6-7 are

Figure 6-5 Coherent ULF oscillations of the ion saturation current as recorded by two probes separated by 180° in azimuth and on slightly different radial surfaces.

FIG. 6-6



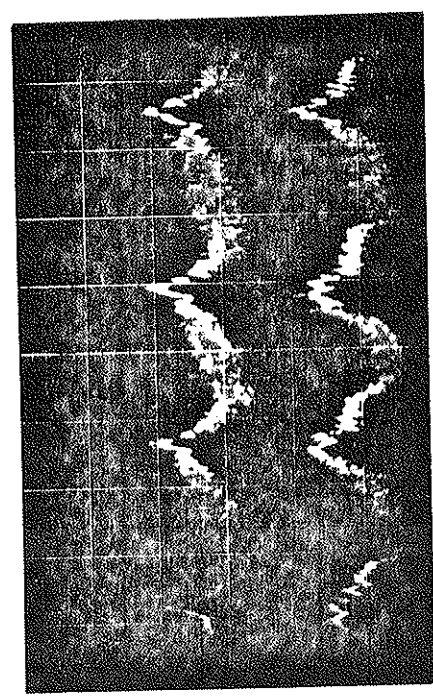
unfiltered as are all the signals in this chapter and all other chapters.

At 154 G the plasma was observed to be unstable to a single, highly coherent oscillation. This mode was identified as an $m=1$, FLR, trapped electron mode at a frequency $f = 18.0$ kHz. (Using the dispersion relation derived in Chapter 5, we calculated a frequency $f = 18.7$ kHz for the measured plasma parameters.) As the field strength was increased a second trapped electron mode was destabilized and grew larger. At the same time the $m=1$ mode decreased in amplitude as \bar{B} was increased until, at $\bar{B} = 196$ G, the only instability present in the plasma was the new mode. This mode was identified as an $m=2$, FLR, trapped electron mode at a frequency, $f = 19.0$ kHz (theoretically predicted frequency, $f = 22.0$ kHz). In the transition regime ($\bar{B} \approx 181$ G) both the $m=1$ and $m=2$ modes were present and the plasma broke into highly coherent ULF oscillations at a frequency, $f = 170$ Hz. (The high frequency oscillations superimposed upon the ULF oscillations in Fig. 7b are due to the trapped electron instabilities.)

As the magnetic field strength was increased still further, the plasma evolved into a third high frequency oscillation which was identified as an $m=3$, ∇T_e , trapped electron mode at a frequency, $f = 30.0$ kHz (theoretically predicted value, $f = 33.0$ kHz). Again, the transition field strength regime was characterized by ULF oscillations. This time, however, these oscillations exhibited a broadband frequency spectrum. A pattern, therefore, appeared with respect to the type of ULF

FIG. 6-5

δI_{01}



0.2 VOLT/cm

5 MS/cm

Figure 6-6 Radial profile of the coherent ULF oscillations.



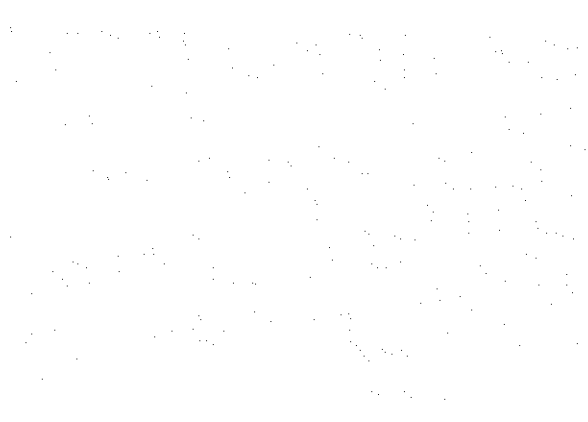
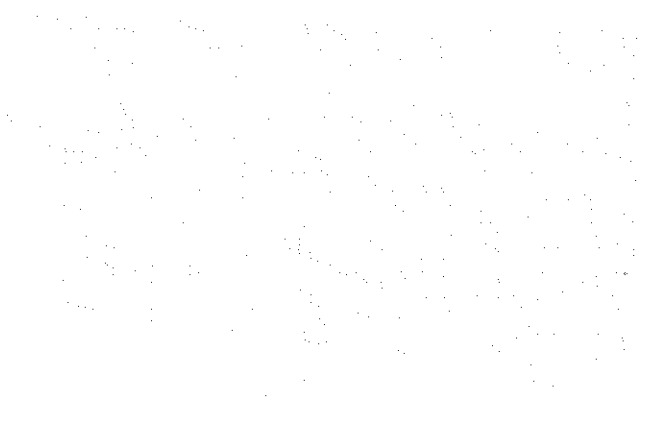


Figure 6-7 a,e Excitation of coherent ULF oscillations during the transition from an $m=1$ FLR mode to an $m=2$ FLR mode at nearly the same frequency (a-c). Excitation of broadband ULF oscillations during the transition from an $m=2$ FLR mode to an $m=3$ V_{Te} mode at very different frequencies (c-e).

The signals shown in this figure are the fluctuations in the ion saturation current as measured by two probes separated by 180° in azimuth and on slightly different radial surfaces.



$B = 154 \text{ G}$

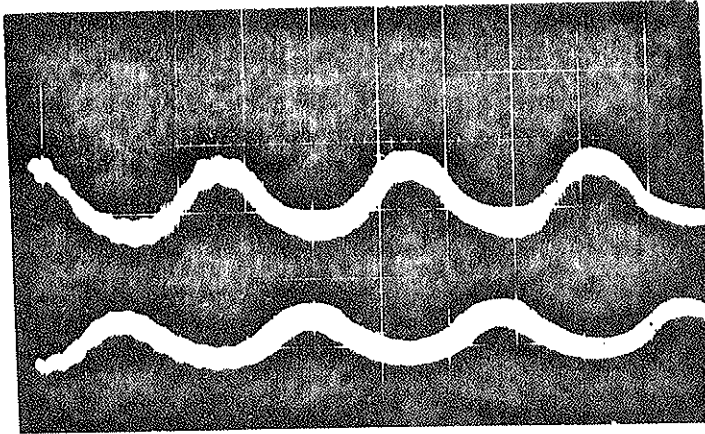


FIG. 6-7

$M = 1$

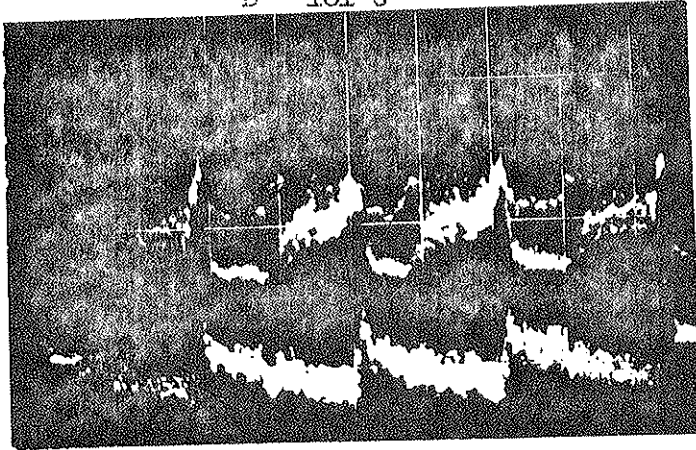
A.

$F = 18.5 \text{ kHz.}$

$.05 \text{ V/cm}$

$20 \text{ } \mu\text{s/cm}$

$B = 181 \text{ G}$



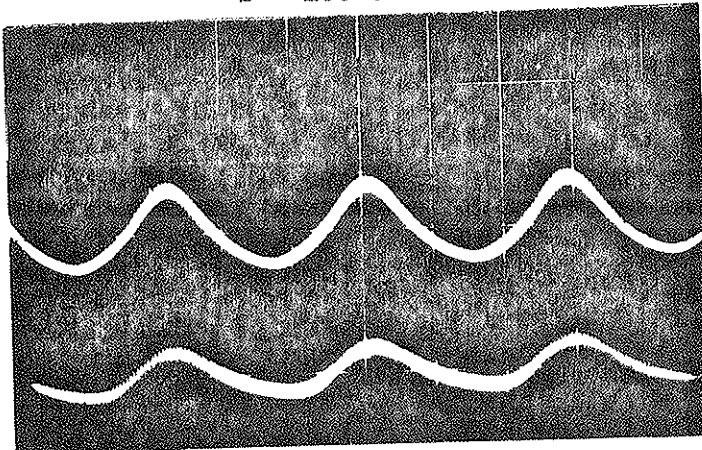
B.

$F = 170 \text{ Hz.}$

$.1 \text{ V/cm}$

5 ms/cm

$B = 196 \text{ G}$



C.

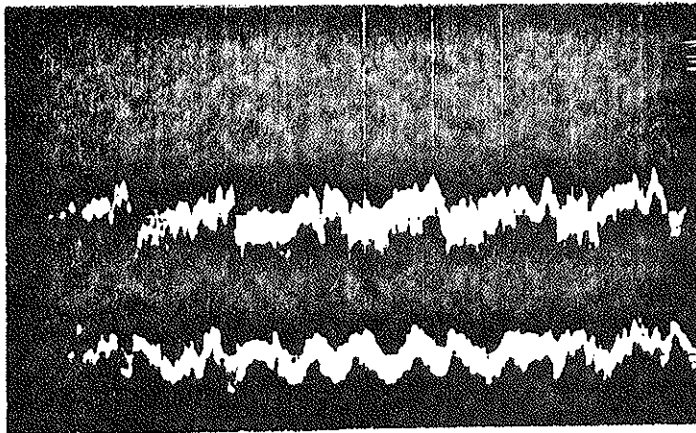
$M = 2$

$F = 19.0 \text{ kHz.}$

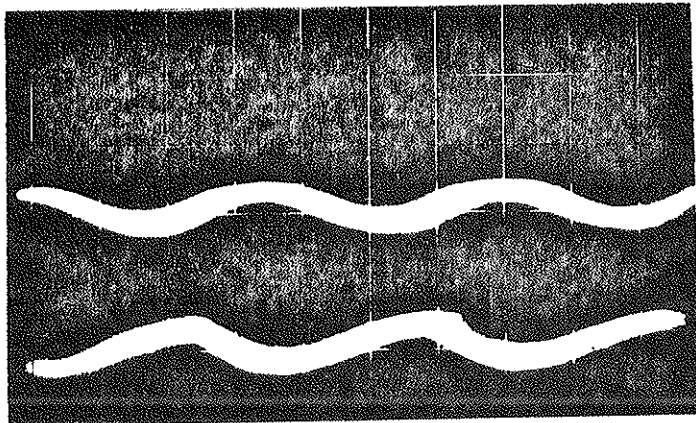
$.1 \text{ V/cm}$

$20 \text{ } \mu\text{s/cm}$

FIG. 6-7 CONT.

 $B = 262 \text{ G}$ 

D.

BROADBAND FREQUENCY
SPECTRUM $.2 \text{ V/cm}$ 5 MS/cm $B = 340 \text{ G}$ 

E.

 $M = 3$ $F = 30.0 \text{ kHz.}$ $.2 \text{ V/cm}$ 10 MS/cm

oscillations being excited. If the two trapped electron modes appeared at nearly the same frequency, the ULF oscillations were highly coherent; if, however, the two trapped electron modes had very different frequencies, the ULF oscillations exhibited a broadband frequency spectrum. This pattern has been observed several times in subsequent experiments.

This point can be amplified by considering Figs. 6-8 and 6-9. In both figures the frequency spectrum of the oscillations of the ion saturation current are shown. In Fig. 6-8 an FLR mode at $f \approx 19$ kHz and a VT_e mode at $f \approx 25$ kHz are shown at $\bar{B} = 282$ G. As the magnetic field strength is increased the frequency spectrum in the vicinity of the trapped electron modes becomes smeared out and the amplitude of the near zero frequency oscillations increases until, at $\bar{B} = 366$ G, it is impossible to resolve the modes at $f \approx 23$ kHz and the plasma exhibits large scale, broadband, ULF oscillations with an approximately $1/f$ spectrum.

In contrast to this, Fig. 6-9 shows the frequency spectrum in a plasma which was exhibiting large scale, coherent ULF oscillations. (The large division mark on the y-axis marks the amplitude of the zero frequency marker generated by the frequency analyzer.) In this case, the frequency spectrum at 18 kHz was highly coherent and the presence of two separate trapped electron modes with different azimuthal mode numbers could not be determined until we spatially Fourier decomposed the instability spectrum.

Figs. 6-8 and 6-9 also reveal another interesting difference

Figure 6-8 a,b Onset of broadband ULF oscillations as the magnetic field strength is increased. (Note the smearing out of the frequency spectrum peaks at approximately 20 kHz.) The lower frequency mode ($f \approx 18\text{kHz}$) is an FLR mode; the higher frequency mode ($f \approx 25\text{ kHz}$) is a $\sqrt{T_e}$ mode.

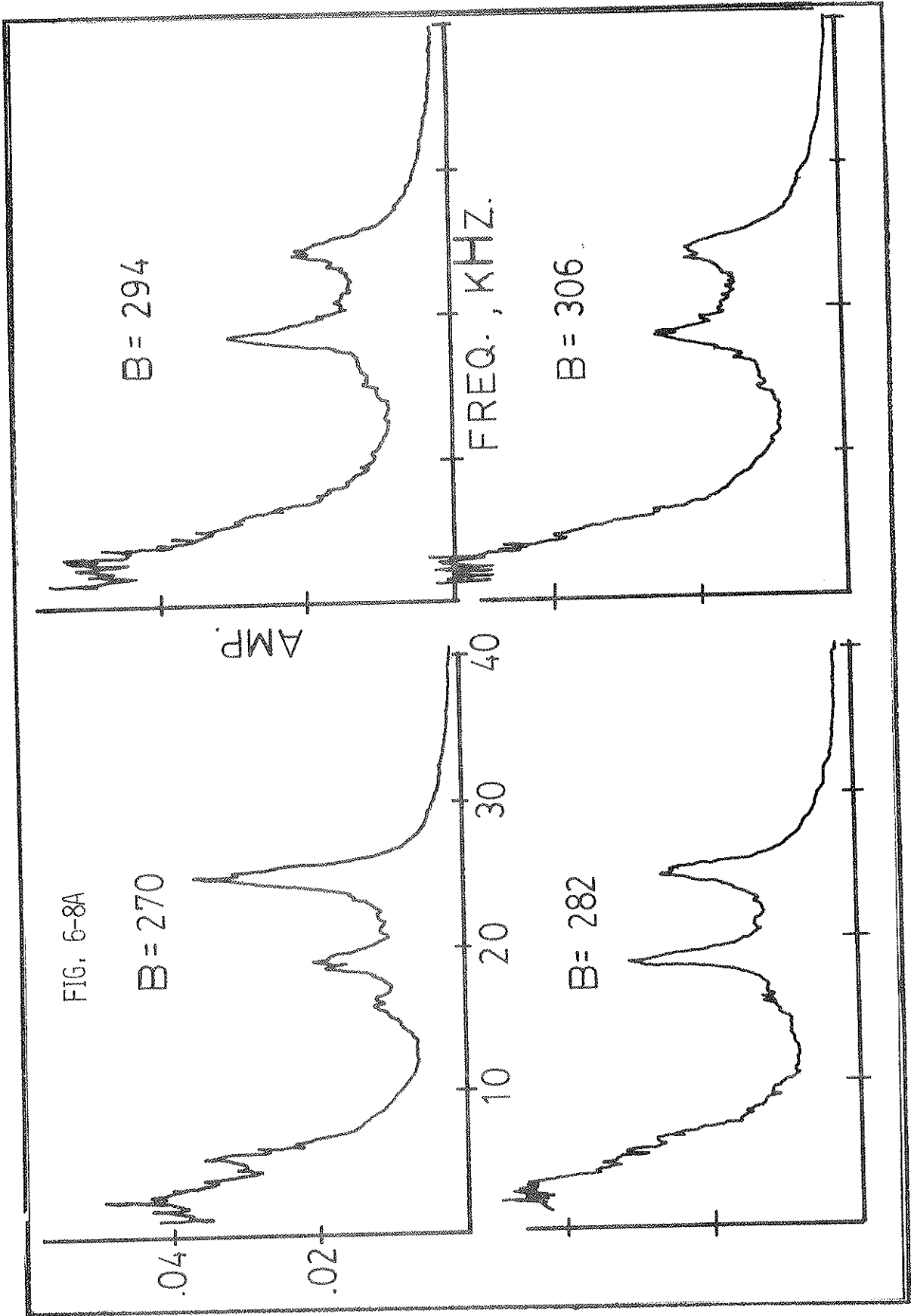


FIG. 6-8A

B = 294

B = 270

B = 306

B = 282

AMP.

FREQ., KHZ.

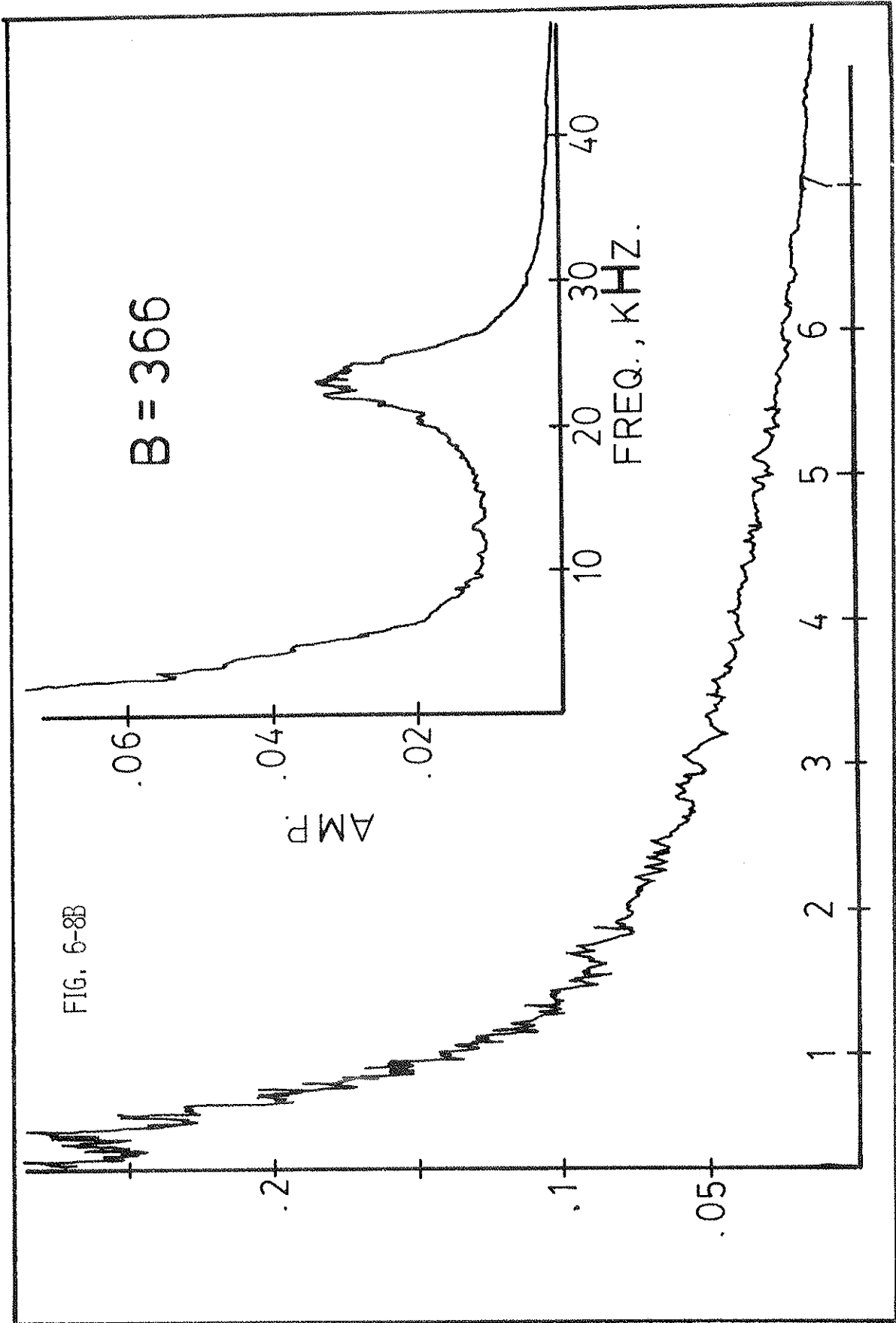
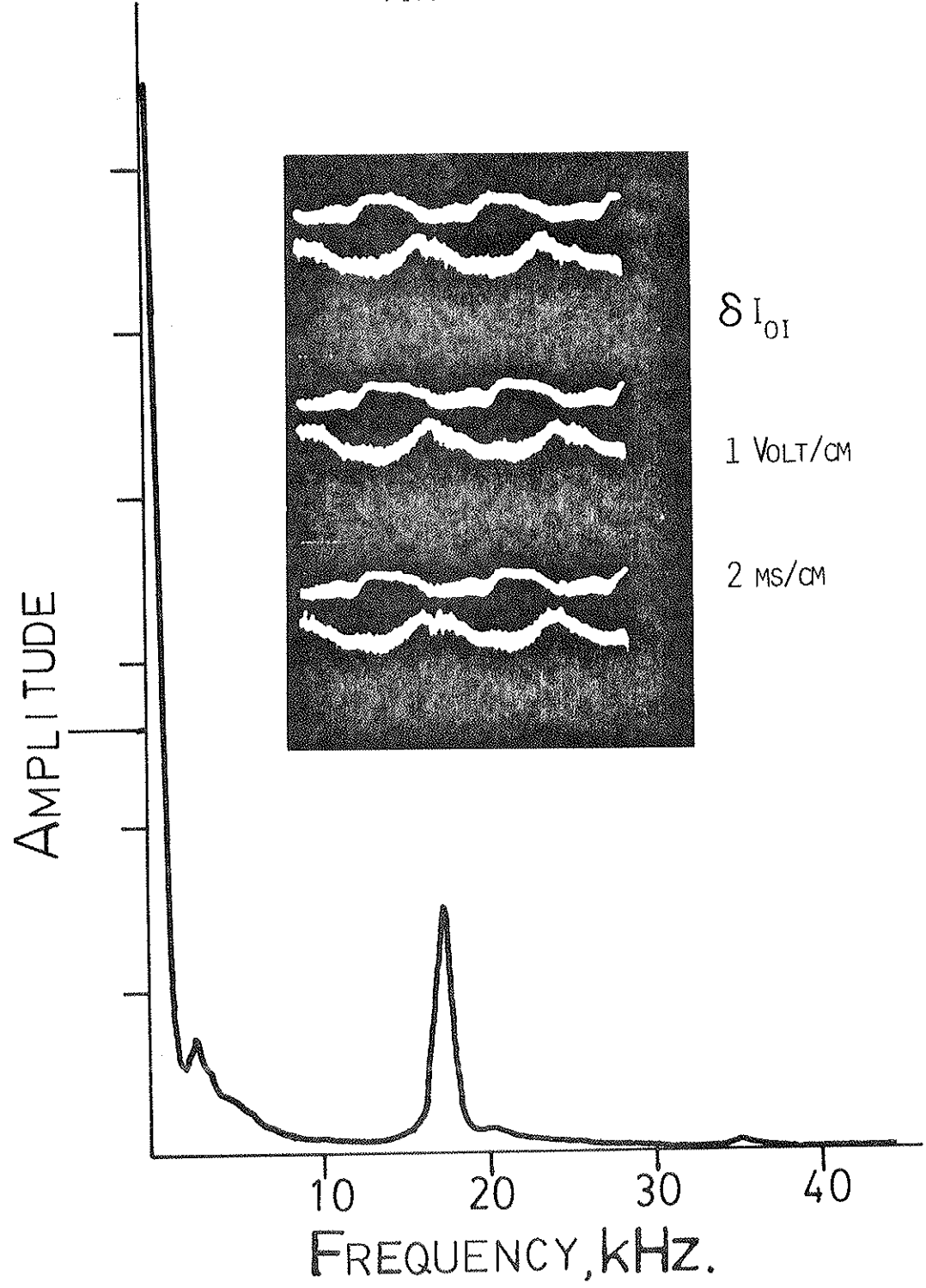


Figure 6-9 Frequency analysis of the fluctuations in the ion saturation current which are shown in the oscillogram in the upper right hand corner of this figure.

FIG. 6-9



between the two types of ULF oscillations. There are a number of frequency spectrums shown in Fig. 6-8. The broadband ULF oscillations appear to be of the soft onset type since a slow increase in the amplitude of these oscillations can be recorded as a critical parameter(s) is changed. However, the coherent ULF oscillations shown in Fig. 6-9 exhibit hard onset, i.e. these oscillations appear quite suddenly as the critical parameter(s) is changed and are excited at nearly maximum amplitude at the time of onset.

At this time we have not determined a theoretical explanation for the excitation of these ULF oscillations. The broadband, near zero frequency oscillations which we observe, however, are quite similar to those observed by Okabayashi¹ in the FM-1 device when it was unstable to more than one drift type of instability. It is not illogical, therefore, to consider the same mechanisms listed in Ref. 1: convective cells²⁻⁴, negative phase velocity ion acoustic instabilities⁵, and ballistic clumps⁶.

The nonlinear excitation of convective cells in the trapped electron regime has been noted by a number of authors^{3,7-9}. The mechanism by which the convective cells are excited is essentially the same for trapped electron instabilities as it is for collisionless drift waves. Okuda and Cheng² have shown that for these modes the nonlinear beating of two drift waves can generate the convective cells due to the differences in the electron and ion responses to the radial E_{θ}/B drift. Convective cells generated in this manner have been observed in computer

simulation of plasmas which are linearly unstable to both collisionless drift waves³ and dissipative trapped electron instabilities.⁷

In the simulation in Ref. 3 they observed that the convective cell saturated at approximately the same amplitude as drift waves, i.e.

$$e\phi/kT_e \lesssim .1 .$$

Our experimental observations of the ULF oscillations can be compared favorably with these theoretical predictions. As shown in Fig. 6-7 a-c we observe the highly coherent ULF oscillations when two trapped electron instabilities with nearly the same real frequency, but different values of k_{\perp} , are present in the plasma at the same time. The resulting ULF oscillations are typical of convective cells in that (1) they are $k_{\parallel} = 0$ modes, (2) they occur at nearly zero frequency, and (3) they saturate with $e\bar{\phi}_f/kT_e \approx 5-10\%$ (recall that we are measuring the oscillations of the floating potential only). At this time there are no published theoretical predictions available with which to compare the level of fluctuations in the ion saturation current which we observed. Work is being done in this area, though.⁴

Numerical solution of the dispersion relation for the trapped electron instability in the LMM (Chapter 5) predicts that modes with different azimuthal mode numbers, m , but the same real frequency, ω , can be unstable in the regime where the temperature gradient driven mode dominates (Figs. 6-10), in the transition regime where both the temperature gradient mode and the finite Larmor radius mode are present (Figs. 6-11 and 6-12), and in the regime where only the finite Larmor

radius mode is present (Fig. 6-13). Since the theory by Cheng and Okuda² predicts that convective cells can be excited whenever there are two drift waves present with the same frequency, but different azimuthal mode numbers, this may explain the fact that ULF oscillations have been observed in all three of the above regimes.

The mechanism by which ballistic clumps or negative phase velocity ion acoustic waves could be excited by trapped electron instabilities has only been intimated¹ without direct theoretical predictions, so no such comparison between these theories and our experiment can be made.

In conclusion, we note that we have experimentally observed ultra low frequency (ULF) oscillations in a linear multimirror device when the plasma was unstable to two dissipative trapped electron instabilities at the same time. When the two trapped electron modes have nearly the same frequency the ULF oscillations are highly coherent. Many of the characteristics of these highly coherent oscillations can be explained in terms of nonlinearly excited convective cells^{2,3}, though other theories may be possible. In addition, we observe large amplitude, broadband ULF oscillations when the plasma is unstable to two trapped electron instabilities at different frequencies. This appears to be a related phenomenon and may be relevant to similar oscillations observed in the FM-1 device¹ and the Culham Levitron¹¹.

Figure 6-10 Instability frequency versus azimuthal mode number for the trapped electron instability. The dispersion relation was evaluated using plasma parameters typical of those for which the ∇T_e mode is the only unstable mode.

FIG. 6-10

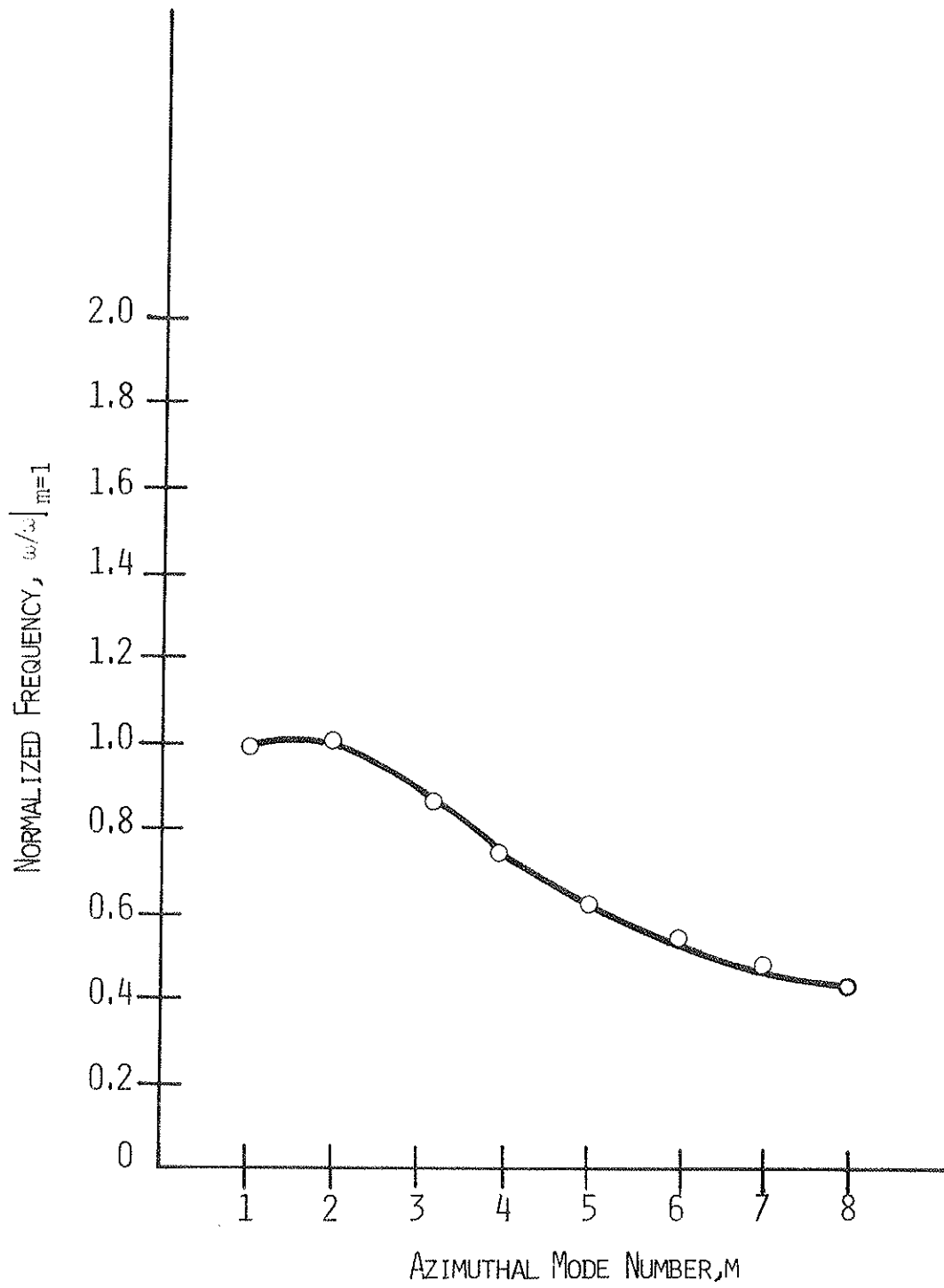


Figure 6-11 Instability frequency versus azimuthal mode number for the trapped electron instability. The dispersion relation was evaluated using plasma parameters which are typical of those at the radial position where the ∇T_e mode has maximum amplitude in the transition field strength regime.

FIG. 6-11

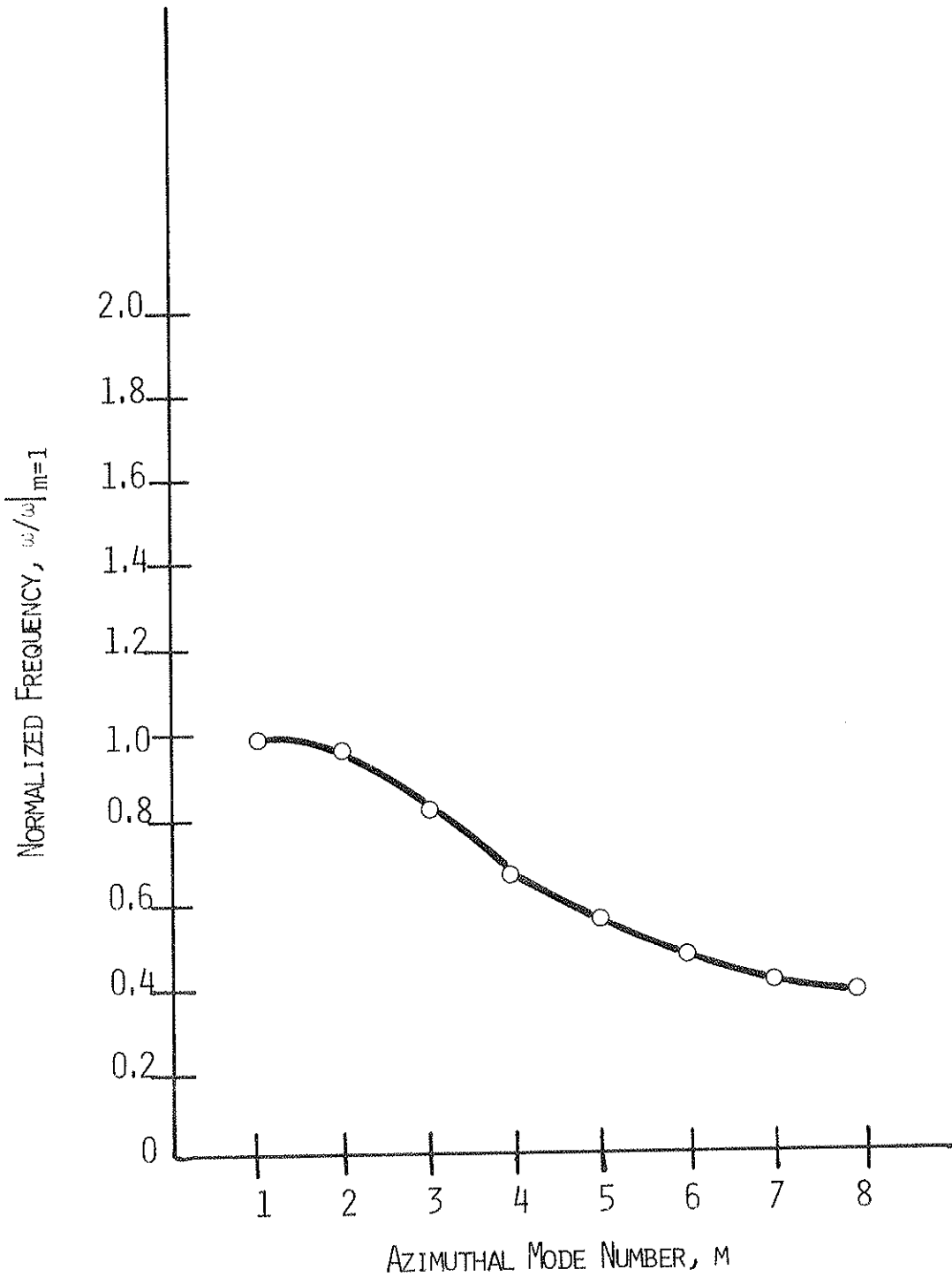


Figure 6-12 Instability frequency versus azimuthal mode number for the trapped electron instability. The dispersion relation was evaluated using plasma parameters which are typical of those at the radial position where the FLR mode has maximum amplitude in the transition field strength regime.

FIG. 6-12

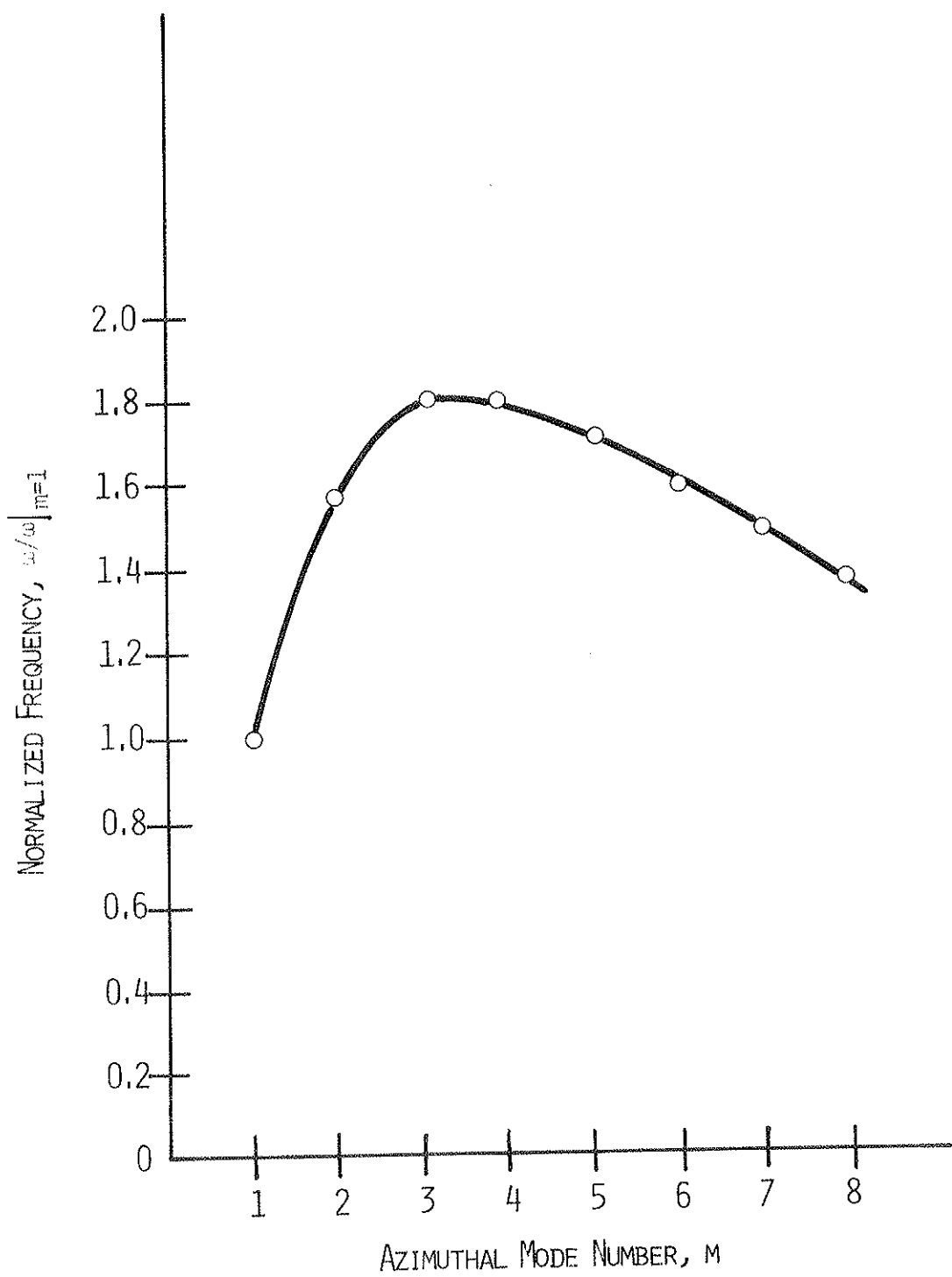
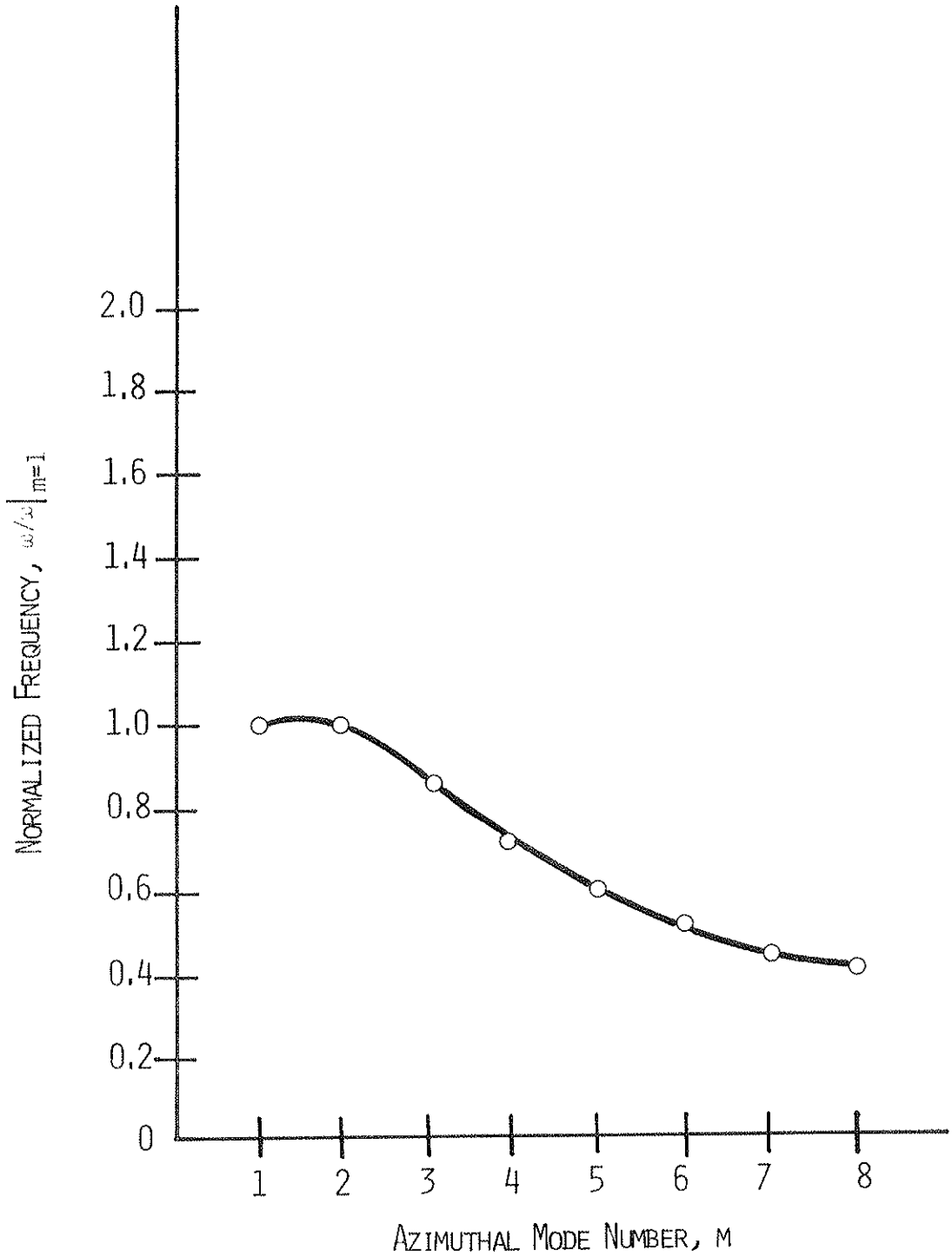


Figure 6-13 Instability frequency versus azimuthal mode number for the trapped electron instability. The dispersion relation was evaluated using plasma parameters which are typical of those for which the FLR mode is the only unstable mode.

FIG. 6-13



References for Chapter 6

1. M. Okabayashi and V. Arunasalam, *Nuclear Fusion*, 17, 497 (1977)
2. H. Okuda and C. Z. Cheng, Princeton Plasma Physics Lab Report PPPL-1204 (1976)
3. C. Z. Cheng and H. Okuda, *Phys. Rev. Lett.*, 38, 708 (1977)
4. P. N. Guzdar, C. Z. Cheng, P. K. Kaw, and H. Okuda, *Bull. Am. Phys. Soc.*, 22, 1127 (1977)
5. B. B. Kadomstev, *Plasma Turbulence*, Academic Press, New York (1965), Chapter 4
6. J. H. Misguich and R. Balescu, EUR-CEA-FC-859, 1976
7. C. Z. Cheng and H. Okuda, *Bull. Am. Phys. Soc.*, 22, 1143 (1977)
8. L. Chen, R. L. Berger, J. G. Lominadze, M. N. Rosenbluth, and P. H. Rutherford, *Phys. Rev. Lett.*, 39, 754 (1977)
9. W. M. Manheimer, E. Ott, K. R. Chu, J. P. Boris, and J. D. Callen, *Nuclear Fusion*, 16, 203 (1976)
10. P. N. Guzdar, C. Z. Cheng, P. K. Kaw, and H. Okuda, *Bull. Am. Phys. Soc.*, 22, 1127 (1977)
11. M. W. Alcock, D. E. T. F. Ashby, J. G. Gordey, T. Edlington, W. H. W. Fletcher, E. M. James, J. Malmberg, A. C. Riviere, D. F. H. Start, and D. R. Sweetman, in *Plasma Physics and Controlled Nuclear Fusion Research 1976*, Proceedings of the Sixth International Conference, Berchtesgaden (IAEA, Vienna, 1977) Vol. II, p. 305

CHAPTER 7

SUMMARY

We have derived a dispersion relation for the dissipative trapped electron mode (DTEM) which includes the plasma phenomena relevant to the Linear Multi-Mirror (LMM). This dispersion relation correctly predicts the behavior of the two instabilities which we observe in the collisionality regime $\nu_e/\varepsilon \approx \omega_{*e}$, where ν_e/ε is the effective electron Coulomb collision frequency for detrapping out of the magnetic mirrors and ω_{*e} is the electron diamagnetic drift frequency.

At high magnetic field strength we observe an instability which exhibits highly coherent oscillations of both the ion saturation current and the floating potential with $\delta I_{oi}/I_{oi} \approx e \tilde{V}_f/T_e$. This mode propagates in the direction of the electron diamagnetic drift at a frequency which is slightly less than the diamagnetic frequency. Radially the mode is localized in a region of coinciding density and electron temperature gradients.

Parallel to the magnetic field the mode is a full wavelength standing wave. In addition, the amplitude of the instability increases with increasing mirror ratio. Based upon the basic drift wave nature of this instability and our ability to predict its parametric dependencies using the dispersion relation for a DTEM, we have identified this instability as a trapped electron mode driven by the electron temperature gradient (∇T_e mode).

At low magnetic field strength we observe a second new instability in the trapped electron regime. This mode also propagates in the direction of the electron diamagnetic drift at a frequency which is, typically, $1/2$ to $1/4$ of the diamagnetic frequency. This mode is also a full wavelength standing wave parallel to the magnetic field and increases in amplitude with increasing mirror ratio. This mode, however, is not well localized radially and has a maximum amplitude in a region of moderately weak electron temperature gradient. Based upon the basic drift wave nature of this instability and the fact that the mode is a strong and predictable function of the magnetic field strength (using the DTEM dispersion relation), we have identified the second instability as a trapped electron instability driven by finite ion Larmor radius effects (FLR mode).

In an intermediate field strength region the plasma can be unstable to both the ∇T_e mode and the FLR mode simultaneously. The ∇T_e mode is localized in the region of strong electron temperature gradient and the FLR mode has maximum amplitude closer to the wall of the vacuum chamber in a region of weak temperature gradient. It was in this regime that we first observed a class of ultra low frequency (ULF) oscillations of the plasma. These ULF oscillations can be very large with $\delta I_{oi}/I_{oi}$ up to 50%. Fluctuations also appear in the floating potential with $e\tilde{V}_f/T_e \approx 5-10\%$. The ULF oscillations propagate in the direction of the electron diamagnetic drift but at a frequency of only a few hundred Hertz (or less), which is much less than either the electron diamagnetic

drift frequency or the ∇B drift frequency. Radially, these oscillations are not well localized, extending from the center of the plasma out to the walls of the device. Parallel to the magnetic field they exhibit a wavelength which is infinite or at least many times the length of the machine.

It appears that these oscillations are nonlinearly excited when the plasma is unstable to two trapped electron modes at the same time. If the two modes have nearly the same frequency the ULF oscillations are coherent. However, if the two trapped electron modes have very different frequencies the resulting ULF oscillations have a broadband frequency spectrum.

The characteristics of the ULF oscillations which we observe compare favorably with those of convective cells which have been predicted to be excited by the nonlinearly coupling of drift waves. Other explanations may be possible, though.